Characterization studies of small-strip Thin Gap Chambers for the ATLAS Upgrade

Benoit Lefebvre
Department of Physics
McGill University

October 2018

A thesis submitted to McGill University in partial fulfilment of the requirements of the degree of Ph.D.

Abstract

The luminosity of the Large Hadron Collider (LHC) at the CERN laboratory will reach up to $\mathcal{L} = 7 \times 10^{34}$ cm^{-2} s^{-1} following a series of upgrades planned over the next decade. The increased luminosity puts a high pressure on the acquisition systems of the LHC particle physics experiments. In order to fully benefit from the increased LHC luminosity, the ATLAS detector, one of the LHC particle physics experiments, will be upgraded during the LHC Long Shutdown 2 beginning in 2019. Part of the ATLAS muon detector system will be replaced to reduce the single muon trigger rate without raising the transverse momentum thresholds. Half of the newly installed detectors are small-strip Thin Gap Chambers (sTGC), a variant of the current ATLAS TGC technology with improved tracking capabilities. A simulation of a set of sTGC detector modules in ATLAS is performed to certify that the manufacturing process and the detector technology are adequate to deliver the performance requirements for the ATLAS upgrade. Measurements of sTGC spatial resolution using cosmic rays and in a test-beam setup are presented. The cosmic-ray measurements are performed in-situ using novel techniques to correct for detector planes misalignments and detector effects. A certification procedure for the quality control of sTGC modules was developed. Results of the procedure with a sTGC prototype are shown as a proof of concept.

Résumé

La luminosité du Grand Collisionneur de Hadrons (LHC) situé au laboratoire CERN atteindra $\mathcal{L} = 7 \times 10^{34}\ \mathrm{cm}^{-2}\ \mathrm{s}^{-1}$ à la suite d'une série de mises à niveau techniques planifiées au cours de la prochaine décennie. Ce haut niveau de luminosité est un défi de taille pour les systèmes d'acquisition de données des expériences associées au LHC. Afin de bénéficier de l'augmentation de la luminosité du LHC, le détecteur ATLAS, l'une des expériences de physique des particles du LHC, sera amélioré pendant le *Long Shutdown 2* du LHC qui débutera en 2019. Une partie du système de détection de muons d'ATLAS sera remplacé dans le but de réduire le taux de déclenchement du système d'acquisition de données pour les événements à un muon sans pour autant augmenter les seuils de quantité de mouvement transverse. La moitié des nouveaux détecteurs seront de type *small-strip Thin Gap Chamber* (sTGC), une variante des détecteurs TGC actuels d'ATLAS, qui se distinguent par une meilleure aptitude pour la localisation de particles. Une simulation d'un ensemble de modules sTGC dans ATLAS a été réalisée afin de confirmer que les méthodes de fabrication des nouveaux modules de détection et que la technologie sTGC permettra d'atteindre les critères de performance demandés pour la mise à niveau d'ATLAS. Des mesures de la résolution spatiale, obtenue en utilisant des rayons cosmiques et un faisceau de pions, sont aussi présentées. La résolution spatiale avec rayons cosmiques est obtenue *in-situ* en utilisant une technique d'analyse innovatrice qui corrige pour les désalignements entre les plans de détection ainsi que pour d'autres effets intrinsèques. Finalement, une procédure de certification a été développée pour le contrôle qualité des nouveaux détecteurs sTGC. Les résultats de la procédure, obtenus avec un petit détecteur prototype, sont présentés à titre de démonstration de faisabilité.

Acknowledgments

This dissertation is the conclusion of a research work that would not have been possible without the continuous support of many people. First, I cannot express my gratitude enough to my supervisor, Brigitte Vachon[1], with whom I have had a fantastic academic experience, long scholarly discussions and a shared passion for physics. She has given me, through this doctoral degree, a unique opportunity to push my limits and challenge myself intellectually.

Thanks to Andrée Robichaud-Veroneau[1] and Camille Bélanger-Champagne[1] for their precious help and fruitful collaboration at the McGill sTGC Testing Facility. Thanks to Vladimir Smakhtin[2], Ilia Ravinovich[2] and Gianluigi de Geronimo[3], all very talented scientists with whom I learned almost everything I know about instrumentation.

Thanks to my fellow graduate students, which include, although the list is far from exhaustive, Alessandro, Anabel, Auriane, Benjamin, Félix, Kuhan, Lévis, Robert, Sébastien, Sheir, Shreya, Waleed and Wei. Thanks for making the McGill workplace so lively and exciting.

Thanks to Stewart Boogert[4] and Véronique Boisvert[4] for giving me the opportunity to reside at Royal Holloway, University of London, for the time of writing my thesis.

On a more personal note, my family deserves a special recognition. I am grateful to my parent Lucie and Claude, my siblings Simon, Cécile and Bruno, and my partner Helena for supporting me. They always believed in me and are making this work much more meaningful.

Finally, my research project would not have been possible without the financial support of the FRQNT[5] which has funded my doctoral studies. Moreover, the Shrum fund, McGill University Graduate and Postdoctoral Studies and the McGill Department of Physics funded many of my field trips to Israel and at the CERN laboratory. This additional mobility has greatly expanded the scope and the quality of my research.

1. McGill University, Canada
2. Weizmann Institute of Science, Israel
3. Stony Brook University, United-States of America
4. Royal Holloway, University of London, United Kingdom
5. Fonds de Recherche du Québec - Nature et Technologies

Statement of originality and contributions of co-authors

The cosmic-ray results that are presented in this dissertation were obtained in collaboration with the members of the McGill University ATLAS group. The facility equipment, gas system and cosmic-ray hodoscope were all commissioned in collaboration with members of the group. The 40×60 cm^2 sTGC prototype was assembled by members of the ATLAS NSW group.

The NSW sector simulation, described in Chapter 4, and the cosmic-ray analysis, described in Chapters 5 and 6, were entirely developed by the author of this dissertation. The author was also in charge of the readout electronics calibration, the trigger processor design and the data taking for the cosmic-ray measurements presented in Chapters 5 and 6. Test-beam measurements and the analysis work that followed were performed in collaboration with members of the ATLAS NSW group. The author's contribution to the test-beam measurements is in the commissioning of the experimental setup and the development of techniques for the baseline measurement of VMM1 ASICs.

Contents

1

Introduction

Particle physics is the study of the nature of the most fundamental constituents of matter and their interactions. Most subatomic phenomena are, to this day, accurately described by the Standard Model (SM) of particle physics [1]. The SM, however, fails to provide answers to several fundamental questions such as “what is the nature of dark matter believed to exist in the Universe?”, “what is the origin of the matter-antimatter asymmetry which has resulted in a matter dominated Universe”, and “can all forces of nature, including gravity, be mathematically described with one grand unified theory?”. In order to address some of these questions, subatomic physics research aims to search for Beyond the Standard Model (BSM) phenomena.

The search for BSM phenomena and precision tests of SM predictions can be performed at particle collider experiments. In a collider experiment, a particle accelerator is used to bring two particle beams travelling in opposite directions into collision. Particles in the beam are accelerated at a sufficiently high energy such that a fraction of the beam particles undergo inelastic collisions resulting in the creation of secondary particles as described by the mass-energy equivalence principle of special relativity [1]. The possible outcomes of a particle collision are determined by the fundamental interactions between the particles involved and, therefore, provide information about different subatomic phenomena occurring in nature. The study of high energy particle collisions in the laboratory is therefore used to test predictions of the SM and search for new physics phenomena.

The electric charge, trajectory and energy of secondary particles created in high energy particle collisions are measured with large detectors that surround the collision

1. The mass-energy equivalence principle states that any particle of mass m at rest is equivalent to a quantity of energy E given by the famous expression $E = mc^2$ where c is the speed of light.

interaction region. Interactions between particles are fundamentally nondeterministic as they are driven by the principles of quantum mechanics. Thus, a large number of collisions is necessary to test SM predictions especially if they involve rare physics processes.

The Large Hadron Collider (LHC) [2], located at the CERN Laboratory in Switzerland, is the most powerful particle accelerator built to this day. It accelerates two beams of protons in a ring 27 km in circumference. The proton beams are made to collide in multiple interaction regions around the ring. The interaction regions host different independent particle physics experiments. Before the end of its operations in 2037, the LHC will be upgraded during two different long shutdown periods, first in 2019-2020, and then in 2025-2026. As part of these planned upgrades, the intensity of the proton beams will be increased in order to achieve a higher rate of proton collisions in the interaction regions. The increased rate of collisions will enhance the discovery potential of the LHC particle physics experiments by providing a steadily increasing dataset allowing more precise SM measurements and the study and search for rare phenomena with increasing sensitivity.

The foreseen increased rate of collisions is a challenge for the detector systems of the LHC experiments because they will have to cope with higher readout rates, detector occupancy and particle fluxes. In order to fully benefit from the physics opportunities offered by the planned increase in LHC beams intensity, LHC experiments are also scheduled to undergo various upgrades of their detector systems. In particular, during the 2019-2020 LHC shutdown period, the ATLAS experiment [3] at the LHC will replace part of its detector systems in order to significantly improve the ability to precisely measure the trajectory of muons [2]. This improved detector capability will result in a background rejection rate sufficient to maintain the detector readout rate at an acceptable level with little or even no loss in sensitivity to rare physics processes. These improvements in the

2. Muons are elementary particles with the same properties as the electrons except for their heavier mass.

ability to measure the trajectory of muons in the ATLAS experiment will be achieved by replacing part of its existing muon detector system by new detector modules called "small-strip Thin Gap Chambers" (sTGC). This dissertation focuses on the performance and construction of sTGC modules as part of this ATLAS upgrade project.

1.1 Particle physics overview

The SM is a theory that describes the properties and interactions of the elementary particles in nature. The SM is expressed using the theoretical framework of Quantum Field Theory under which particles are treated as an excited state of an underlying field that permeates space-time. Quantum field theories are consistent with the fundamental principles of special relativity and quantum mechanics. Some of the properties characterizing particles are their electric charge, spin and mass. The spin is a quantum number [3] associated with the intrinsic angular momentum carried by the particle. Elementary particles are either fermions, of spin ½, gauge bosons, of spin 1, or scalar bosons, of spin 0. In addition, elementary particles can combine to form a wide variety of composite states. A table of the known elementary particles described by the SM is shown in Fig. 1.1.

Particles interact via four fundamental forces which are, in order of increasing relative strength, gravity, the weak force, the electromagnetic force and the strong force. All fundamental forces, with the exception of gravity, are mathematically described as arising from the exchange of gauge bosons. The nature of interactions between particles is determined by a set of parameters which include the coupling constants of the fundamental forces. The Z and W bosons mediate the weak force, the photon (γ) mediates the electromagnetic force and the gluon (g) mediates the strong force. To this day, no force mediator for gravity has been observed and the SM does not include a description of gravity. Gravity is, however, significantly weaker than other fundamental forces at the

3. A quantum number describes the dynamics of a quantum system and is associated to the value of a conserved quantity.

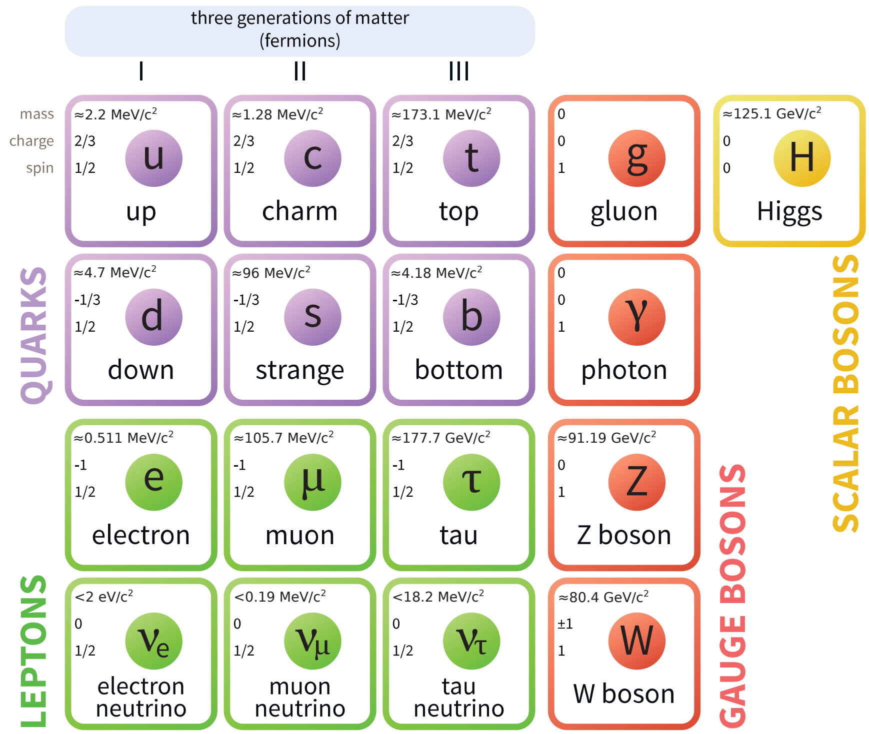

Figure 1.1: Schematic diagram [4] showing the different types of elementary particles observed in nature and described by the Standard Model of particle physics. Particles are arranged in different categories according to their properties. The mass, electric charge and spin of the particles are also indicated using values taken from [5].

microscopic level and its effects are not noticeable in a particle collider experiment.

Elementary fermions can be classified in two categories named quarks (q) and leptons (l), the later being insensitive to the strong force. Quarks exist in six different flavours: up (u), down (d), charm (c), strange (s), top (t) and bottom (b). The lepton flavours are electron (e), muon (μ), and tau (τ). Flavour is a quantum number, intrinsic to the particle, that governs the amplitude and range of possible interactions between SM particles. To each lepton flavour is associated one charged particle and one neutrino (ν). Neutrinos are very light [4] and electrically neutral particles that do not undergo electromagnetic interactions. As shown in Fig. 1.1, fermions are classified in three generations

4. Neutrinos are assumed massless in the SM but a number of experiments performed in the last 20 years suggest it is not the case [6,7].

of increasing mass and varying flavour content. Each generation contains two quarks in addition to one charged lepton and one neutrino of the same flavour.

For each fermion, there exists a corresponding antiparticle of equal mass having opposite intrinsic quantum numbers [5]. For example, the electric charge carried by antiparticles is equal but opposite to that of particles. This dissertation refers to both the particle and the antiparticle when the charge is not specified. For example, the symbol μ refers to both muons (μ^-) and antimuons (μ^+).

The Higgs boson (H) completes the set of particles described by the SM. The Higgs is an electrically neutral boson of spin 0. The Higgs boson is not a force mediator but interacts with all elementary particles, including itself. The strength of this interaction is described by a coupling constant proportional to the mass of the particles interacting with the Higgs boson. The existence of a Higgs field permeating all space can therefore explain the origin of the mass of all elementary particles [10].

Quarks cannot exist in a free state because the strength of the strong force increases as a function of the distance between quarks. Quarks are observed to form bound states of two quarks, named mesons, or three quarks, named baryons [6]. Quark bound states are collectively called hadrons. The mass and properties of hadrons are a function of the quark content, the spin angular momentum and the orbital angular momentum of the system. Mesons are composed of one quark and one antiquark, and have integer spin values. For example, pions are spin-0 mesons composed of a combination of the quarks u and d. Neutral pions (π^0) have a lifetime of 8.5×10^{-17} s [5] and decay preferably to two photons. Charged pions (π^+/π^-) have a longer lifetime of 2.6×10^{-8} s [5] and can travel several meters before they decay. Baryons are composed of either three quarks or three

5. To this day, no experimental observation has settled whether neutrinos are the same particle as antineutrinos. The observation of a neutrinoless double beta decay could indicate that neutrinos and antineutrinos are, in fact, the same particle [8]. The process has not been observed to this day, but a number of experiments are ongoing to search for the existence of this reaction [9].

6. Other exotic structures such as tetraquarks (4 quarks) or pentaquarks (5 quarks) are not excluded and may have been observed [11,12].

antiquarks making a system of half-integer spin values. For example, the proton and the neutron, the components of the atomic nucleus, are baryons having the quark content uud and udd respectively. Both have spin ½. The proton is considered stable because it is the lightest known baryon and thus cannot decay without violating the baryon number conservation law. The neutron has a lifetime of 880.2 s [5] but is stable if bound in the atomic nucleus of a stable isotope.

The SM is used to calculate the outcome of a wide variety of phenomena such as the lifetime of fundamental and composite particles, the cross-section of physics processes and the mass of composite states. The accuracy of SM predictions depends on the precise knowledge of the SM free parameters which include the mass of fundamental particles and the interaction coupling constants. Differences between SM predictions and experimental observations would provide hints of the existence of new physics phenomena beyond the SM. The precise measurement of SM parameters and the rigorous test of SM predictions in a particle collider experiment necessitate a large number of collisions because some of the processes of interest are extremely rare. Thus, the advancement of particle physics depends on the beam intensity delivered by accelerators and the capacity of detectors to provide precise measurements at high readout rate.

The increase in the number of collisions following the planned LHC upgrades will make it possible to carry out an extensive and broad research program that aims at addressing several of the main questions in particle physics. To do so, this research program will focus on searches for new physics phenomena and the exploration of the region of validity of the SM. This will be done, for example, through precision measurements of the Higgs boson properties and, more generally, the study of physics phenomena at the TeV energy scale. The search for new physics phenomena, including hypothetical particles that could make up the dark matter in the universe, will also be enhanced by the significant increase in the amount of collision data to be recorded. This ambitious research program calls for an upgrade of the ATLAS experiment through the replacement of part of the muon detection system by small-strip Thin Gap Chambers.

1.2 Thin Gap Chamber technology overview

Thin Gap Chambers (TGC) are a variant of the Multi-Wire Proportional Counter (MWPC) introduced by Charpak [13] in the 1960's. An MWPC is a planar gaseous ionization detector. The gas volume is contained between two cathode planes with an array of parallel anode wires stretched in between. An MWPC operates by collecting the ionization created in the gas volume by the passage of ionizing radiation. The ionization charge is multiplied by the action of the high electric field in the vicinity of the anode wires through a process called a Townsend avalanche [14–16]. Therefore, a relatively large electric signal is measured on the anode wires despite a modest amount of primary ionization having taken place in the gas volume. A measure of the position of incoming ionizing radiation can be obtained by reading out the signal induced on individual anode wires, pickup electrodes on segmented cathode planes or both.

The first TGC detectors were manufactured in the 1980's [17] as a proof of concept for a compact multi-wire chamber. Then, the technology was successfully used as the sensitive volume of a calorimeter for the OPAL experiment [18–22] at the Large Electron Positron collider [23] which operated between 1989 and 2000. Thin Gap Chambers are currently used in the ATLAS experiment to measure the trajectory of muons as a means to trigger the readout of the entire detector [24]. Small-strip Thin Gap Chambers are an improved version of the technology offering a better spatial resolution and higher particle flux capabilities. This is the new detector technology that will be installed in ATLAS during the 2019-2020 LHC shutdown.

1.3 Dissertation overview

This dissertation presents simulation and detector characterization studies aimed at validating the sTGC technology and design, the manufacturing process, and the quality control procedure within the scope of the ATLAS muon detector system upgrade. These studies have been essential to ensure that the upgraded muon detector system will achieve the physics performance goals of the ATLAS experiment during high luminosity LHC running.

Chapter 2 presents an overview of the physics principles behind radiation detection using gaseous ionization detectors. A description of the LHC accelerator complex, as well as the ATLAS experiment and the muon detector system, is found in Chapter 3. Simulation studies of sTGC modules, aimed at characterizing the impact of construction non-conformities on the muon track reconstruction performance, are presented in Chapter 4. Performances studies of sTGC detector prototypes in a cosmic-ray and test-beam setups are presented in Chapter 5. The quality control procedure and the algorithms developed for qualifying sTGC modules during module manufacturing are described in Chapter 6. This dissertation is concluded in Chapter 7.

2

Principles of sTGC radiation detection

The physics principles behind radiation detection by small-strip Thin Gap Chamber detectors are discussed in this chapter. The chapter begins with a description of the main interactions between ionizing radiation and the detection medium in Section 2.1. The charge production and transport properties particularly relevant in gaseous media are discussed in Sections 2.2 and 2.3. The general principles of radiation detection with gaseous ionization detectors are presented in Section 2.4.

2.1 Interaction of ionizing radiation with matter

Radiation detection is possible if an interaction occurs with the active medium of a detector. The energy deposited in the medium must be converted into an electric signal to be recorded by a data acquisition system.

Muons produced at the LHC will be detected by sTGC detectors, which are described later in Section 3, via ionization and excitation processes. Furthermore, photon production in the sTGC gas volume may impact detector performances. Only these most relevant processes are discussed in this section.

2.1.1 Ionization and excitation

Charged particles traversing matter undergo a large number of elastic Coulomb collisions with the atomic electrons of the medium. Excitation processes occur when an atomic electron is promoted to a higher energy level of the atom or molecule. Ionization processes occur when an electron receives enough energy to free itself from the molecular potential.

The maximum energy transfer to an atomic electron after a single collision can be derived from kinematics

$$W_{\text{max}} = \frac{2m_e c^2 \beta^2 \gamma^2}{1 + 2\gamma m_e/M + (m_e/M)^2} \tag{2.1}$$

where m_e is the electron rest mass, and β, γ and M are, respectively, the velocity relative to the speed of light c, the Lorentz factor [1] and the mass of the incident particle.

Mean energy loss

The energy loss of a particle traversing matter usually scales linearly with the medium density. Thus, it is convenient to define the "area density" x, that is the distance s scaled to the medium mass density ρ_m. For infinitesimal distances, this relation is expressed as

$$dx = \rho_m \, ds. \tag{2.2}$$

The mean differential energy loss, or "stopping power", due to energy transfers to the atomic electrons is given by the Bethe-Bloch formula [25]

$$\left\langle -\frac{dE}{dx} \right\rangle = K z^2 \frac{Z}{A} \frac{1}{\beta^2} \left[\frac{1}{2} \ln \frac{2m_e c^2 \beta^2 \gamma^2 W_{\text{max}}}{I^2} - \beta^2 - \frac{\delta(\beta\gamma)}{2} \right] \tag{2.3}$$

where K is a constant equal to $4\pi N_A r_e m_e c^2$ which has an approximate value of 0.307 MeV·mol^{-1}·cm^2. The symbol N_A represents the Avogadro number and r_e is the classical electron radius. The symbols E and z are, respectively, the energy and the charge in units of elementary charge of the incident particle. The symbols Z, A and I represent, respec-

1. The Lorentz factor is defined as $\gamma \equiv \frac{1}{\sqrt{1-\beta^2}}$.

tively, the atomic number, atomic mass and mean excitation potential of the medium. The symbol $\delta(\beta\gamma)$ represents the "density effect corrections". The density effect corrections account for the relativistic polarization of the medium. The correction is negligible for $\beta\gamma \leq 100$.

The Bethe-Bloch formula assumes small energy losses (i.e. $W_{\text{max}} \ll E$) and an incident particle significantly heavier than an electron. It does not hold for electrons because it does not account for the quantum indistinguishability between the projectile and the target.

The formula is valid for an incident particle of "intermediate" momentum, that is in the approximate domain $0.1 \leq \beta\gamma \leq 1000$. At lower momentum, the electrons atomic binding energy is significant and shell corrections are necessary. At higher momentum, radiative effects dominate the energy loss.

Inside its domain of applicability, the Bethe-Bloch formula is accurate within a few percents. An example of the average energy loss of a muon traversing a sTGC gas volume is shown in Fig. 2.1. The energy loss is computed from the Bethe-Bloch formula and assuming ideal gases. The mean ionization potentials of the gas components are taken from the NIST PSTAR database [26]. The Bethe-Bloch formula is proportional to β^{-2} in the low momentum range and to $\ln(\beta\gamma)$ in the high momentum range. A muon is a minimum ionizing particle (mip) at $p_\mu \sim 0.35$ GeV$/c$.

Variations in energy loss

Variations in the energy loss ϵ by a particle in a medium of thickness δx can be expressed in terms of the Landau probability distribution function [27]

$$f(\epsilon, \delta x) = \frac{1}{\xi}\phi(\lambda) \tag{2.4}$$

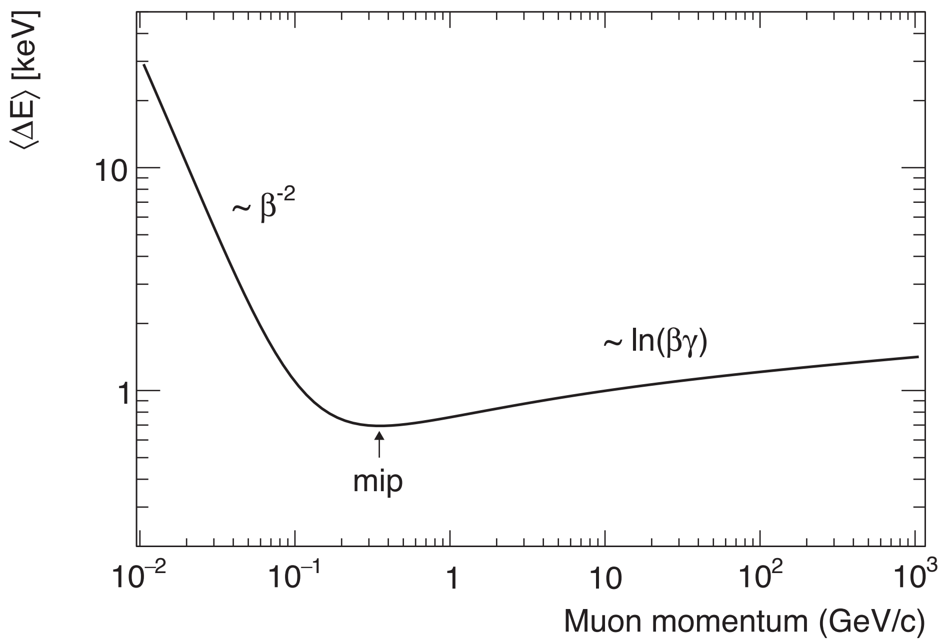

Figure 2.1: Mean energy loss from electronic interactions of a muon traversing the gas volume of a sTGC detector. The energy loss is computed assuming a gas volume with a thickness of 2.8 mm filled with a mixture of n-pentane and CO_2 in the ratio 45:55.

where $\phi(\lambda)$ is the "Universal Landau Function" given by

$$\phi(\lambda) = \frac{1}{2\pi i}\int_{c-i\infty}^{c+i\infty} \exp\left(u \ln u + \lambda u\right)\ du \qquad c > 0 \tag{2.5}$$

and ξ is a scale parameter having units of energy. It is derived from the Rutherford scattering cross-section and is defined as

$$\xi = \frac{z^2 q_e^4 N_A Z}{8\pi\varepsilon_0^2 m_e c^2 A\beta^2}\ \delta x = 153.4\ [\text{keV cm}^2\ \text{mol}^{-1}]\ \frac{z^2}{\beta^2}\frac{Z}{A}\delta x, \tag{2.6}$$

where q_e is the elementary charge and ϵ_0 is the permittivity of vacuum. The parameter λ is unitless and proportional to the energy loss ϵ. The parameter λ is defined as

$$\lambda = \frac{\epsilon - \bar{\epsilon}}{\xi} - \beta^2 - \ln \frac{\xi}{W_{\max}} + \gamma_e - 1. \tag{2.7}$$

where $\bar{\epsilon}$ is the average energy loss obtained from the Bethe-Bloch formula. The symbol γ_e represents the Euler-Mascheroni constant of approximate value 0.577 [28]. Examples of energy loss distributions predicted by the Landau theory in a sTGC gas volume for different incident muon energies are shown in Fig. 2.2.

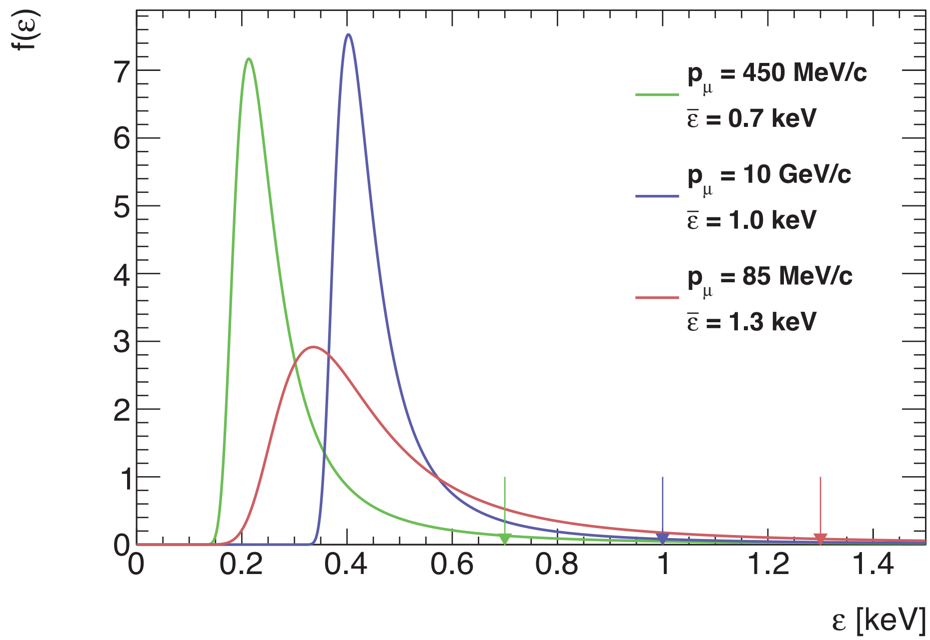

Figure 2.2: Fluctuations of energy loss predicted by Landau's theory for muons traversing a sTGC gas volume. The arrows indicate the mean energy loss $\bar{\epsilon}$ obtained by the Bethe-Bloch formula.

Landau's theory assumes that the incident particle undergoes a large number of collisions in a thin material with no limit on the maximum transferable energy $W_{\max}$. The typical energy transfer is assumed to be large compared to the binding energy of the atomic electrons. Variations of energy loss are actually limited by kinematics. A more accurate energy loss distribution that assumes a finite $W_{\max}$ was derived by Vavilov [29]. For thick materials, the tail is reduced and the energy loss distribution resembles more that of a Gaussian function [30].

The Landau distribution is highly skewed. The theoretical expression has no defined mean or standard deviation. The most probable value (MPV) is a more meaningful figure of merit when characterizing the distribution. An expression for the MPV is derived from taking the maximum of Eq. 2.4 [31]

$$\max(\epsilon) = \xi \left[\ln \frac{2m_e c^2 \beta^2 \gamma^2}{I} + \ln \frac{\xi}{I} + 0.2 - \beta^2 \right] \tag{2.8}$$

Production of δ-rays

The momentum transfer to atomic electrons is sometimes large enough to produce an ionization electron with sufficient momentum as to further interact in the detector medium, called a δ-ray. The approximate energy distribution of the δ-rays produced in a medium of thickness δx is given by [14]

$$P(E_\delta) = K \frac{Z}{A} \frac{1}{\beta^2} \frac{\delta x}{E_\delta^2} \tag{2.9}$$

where K is a constant taken from the Bethe-Bloch formula in Eq. 2.3. In principle, the distribution of Eq. 2.9 should be bounded at W_{max}, the maximum transferable energy. Large energy transfers are, however, rare, especially for heavy particles at high momentum.

The δ-rays have a significance because they smear the primary ionization column along the trajectory of the incident particle. The spread of primary ionization degrades the spatial resolution of tracking devices, including sTGC detectors. The effect is especially important when the δ-ray electron range in the medium is large like for gaseous ionization detectors.

Furthermore, δ-rays can be created in the structural supports and electrodes of the detector. If the separation between the trajectory of the incident muon and that of the δ-ray is sufficient, the ionization produced by the δ-ray can be reconstructed as a separate hit in the detector.

2.1.2 Photon processes

Photons are neutral particles ($z = 0$), and therefore they do not interact with the medium via excitation and ionization processes. Photons are detected from other processes that produce free electrons. Of all possible photon interactions with matter, the following three have a significant importance for detector operation at the energy scale of collider experiments [32]:

- **photoelectric effect** by which an atomic electron is freed after it absorbs the incident photon,
- **Compton scattering** which corresponds to a collision between an atomic electron and the incident photon,
- **pair production** by which the incident photon is converted into an electron-positron pair when it interacts with the Coulomb field of an atomic nucleus or an atomic electron of the medium.

Photons that interact via the aforementioned processes are either completely absorbed (photoelectric effect, Compton absorption and pair production) or scattered at a very large angle. The cross-sections in lead of the major photon processes are shown in Fig. 2.3. The photoelectric effect is dominant at low energies (below 1 MeV). Then, Compton effects and pair production dominate the intermediate (around 1 MeV) and high (above 1 MeV) energy ranges, respectively.

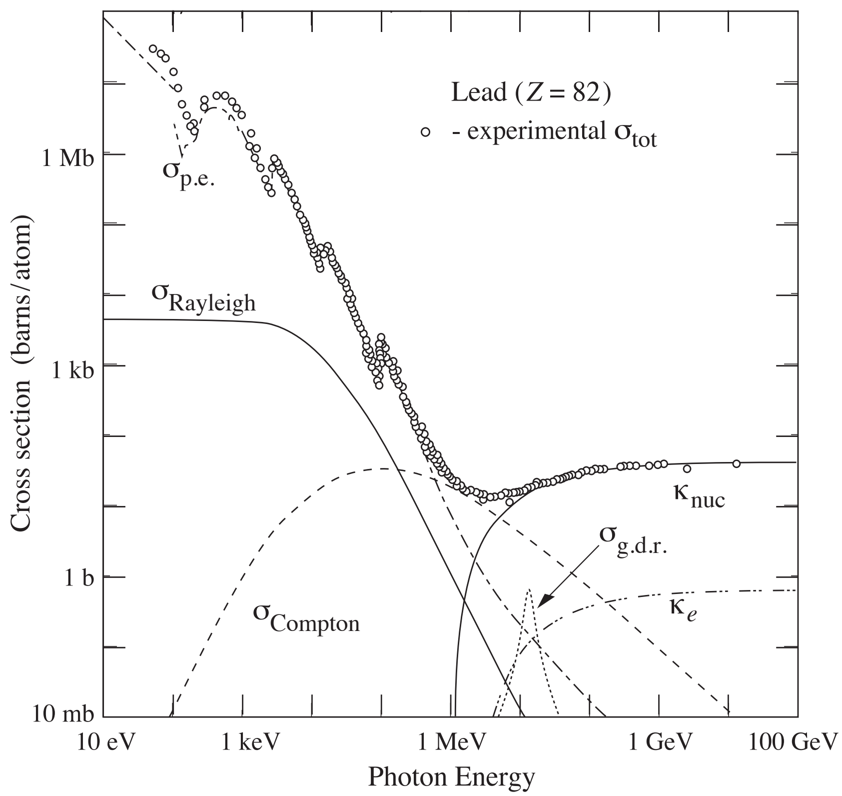

Figure 2.3: Interaction cross-section of photons in lead [5]. The contribution of individual photon processes, including the photoelectric effect ($\sigma_{\text{p.e.}}$), Compton effects (σ_{Compton}) and pair production (in the nuclear field, κ_{nuc}, and in the electron field, κ_e) is shown. The contribution of Rayleigh scattering (σ_{Rayleigh}) and photonuclear interactions ($\sigma_{\text{g.d.r.}}$) to the photon cross-section is also shown. These processes were not mentioned in the text because they are not dominant.

2.2 Yield of ionizing radiation

Assuming that the incident particle interactions with the atomic electrons are independent events, the probability for the number of ionization events created in the medium is given by a Poisson distribution

$$P(k) = \frac{\bar{k}^k}{k!} e^{-\bar{k}} \tag{2.10}$$

where k is the number of ionization events and $\bar{k}$ is the mean number of interactions. The mean number of interactions $\bar{k}$ depends on the cross-section of the incident particle in the medium and the molecular density of the medium. Each ionization event generates an ionization cluster made up of one or more electron-ion pairs depending on the energy loss in the ionization event.

The total ionization n_T is the total number of electron-ion pairs created by the incident particle in the detector medium. The total ionization n_T is proportional to the energy ΔE deposited in the medium [32]

$$n_T = \frac{\Delta E}{W} \tag{2.11}$$

where W is the average energy required for creating an electron-ion pair. The value of W is in general larger than the excitation potential I because excitation processes do not usually result in a free electron. The value of W also accounts for the probability of recombination. For sTGC detectors, the value of W is approximately 32 eV [33], which is a typical figure for gaseous ionization detectors [32].

The value of W is not an intrinsic property of the detector medium. A gas mixture can have a value of W that is lower than that of its individual components by virtue of the “Penning effect” [34,35]. The effect is observed when one of the gas components has a lower ionization potential than the excitation potential of the other gas components. The former can be ionized following a collisional energy transfer with an excited molecule of the other gas components.

For example, the W value of argon can be lowered from 26.2 eV to 20.5 eV with the addition of 0.5% of acetylene while the addition of methane has no impact [36]. Halogen gases are a common choice for creating Penning mixtures because they have a low ionization potential [37].

2.3 Transport properties of drifting charge in a gas

Ions and electrons diffuse in the medium after they are created following a random walk. The spread of a localized distribution of charge can be described by a Gaussian distribution [32]

$$\frac{dN}{N} = \frac{1}{\sqrt{4\pi Dt}} \exp\left[-\frac{r^2}{4Dt}\right] \, d^3\vec{r} \tag{2.12}$$

where $\frac{dN}{N}$ is the fraction of charges located in the space element $d^3\vec{r}$ at time t. The symbol D represents the diffusion coefficient that depends on the mean free path [32] and the velocity of the drifting charge. The mean free path depends on the cross-section of the drifting charge in the medium and the density of molecules in the medium. Assuming no external electric field is applied to the medium, the average molecular kinetic energy is given by $K = \frac{3}{2}k_BT$, following the theorem of equipartition of energy where k_B is the Boltzmann constant and T is the medium temperature [38]. Therefore, electron diffusion is, in general, faster than ions because of their small mass and cross-section.

The spatial standard deviation of the diffusion equation can be expressed either for linear (σ_r) or volume (σ_V) diffusion:

$$\sigma_r = \sqrt{2Dt} \;\; \text{(linear)} \qquad \sigma_V = \sqrt{3}\sigma_r = \sqrt{6Dt} \;\; \text{(volume)}. \tag{2.13}$$

In the absence of an electric field, the ion-electron pairs would quickly recombine after they are created in the detector medium. In a gaseous ionization detector, an electric field is created within the medium in order to allow the positive ions and negatively charged electrons to drift apart. The electric field induces a net motion of the charge carriers in the direction of the field lines. The drift velocity v_d is proportional to the electric field strength E and is defined as

$$v_d = \mu \frac{E}{p} \tag{2.14}$$

where μ, in this context, is the proportionality factor named the "charge-carrier mobility" and p is the pressure of the operating gas. The dependence of the mean free path on the density of molecules explains why the velocity depends on the gas pressure.

The mobility of ions remains fairly constant as a function of the electric field [39]. The value of the ion mobility, denoted μ^+, is typically between 1 and 10 $\text{cm}^2\ \text{atm}\ \text{V}^{-1}\ \text{s}^{-1}$ [14].

The electron mobility, denoted μ^-, is highly dependent on the electric field E because the energy gained by electrons in the field can significantly exceed their thermal energy. Additionally, the electron cross-section varies with energy as predicted by the Ramsauer-Townsend theory [40, 41].

The electron drift velocity in a mixture of n-pentane and CO_2, as used in sTGC detectors, is shown in Fig. 2.4 for various concentrations of n-pentane. The electron drift velocity is of the order of 10 cm/μs which is about one thousand times faster than ions [14].

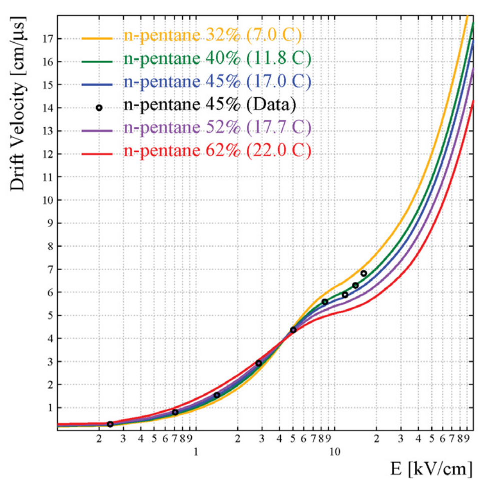

Figure 2.4: Drift velocity of electrons as a function of the electric field for various concentrations of n-pentane in CO_2 [33]. The x-axis covers the possible E field values within the gas volume of a sTGC operating at 2.9 kV.

2.4 Gaseous ionization detectors

Gaseous ionization detectors are sensitive to the movement of charges created by ionizing radiation in their gaseous active medium. The ionization charge drifts towards an anode and cathode electrodes by the action of an electric field that permeates the medium. The operation principles of ionization detectors can be used in a wide range of detector devices and applications including sTGC detectors.

2.4.1 Gas amplification

The total ionization in the gaseous medium of an ionization detector is of the order of 10^2 electrons ($\sim$0.01 fC) for a minimum ionizing particle and assuming a path length of the order of one centimetre at atmospheric pressure [32]. This amount of charge is too small to be detected by most modern readout electronics.

The action of the electric field in the gaseous medium can, however, increase the total charge yield. For electric fields higher than a few kV/cm, drifting electrons acquire enough kinetic energy between collisions to ionize gas molecules. For example, the cross-section for ionization dominates the elastic collision cross-section for electrons of kinetic energy higher than 15 eV in the gas volume of a sTGC detector. The cross-section of the main electron processes in an n-pentane and CO_2 mixture is shown in Fig. 2.5.

Following each ionization process, electrons are accelerated until they gain a sufficient energy to further ionize the gaseous medium. The total ionization charge increases as a function of distance from the detector anode in a process called the "Townsend avalanche" [42]. A simple schematic diagram depicting the phenomenon of a Townsend avalanche is shown Fig. 2.6.

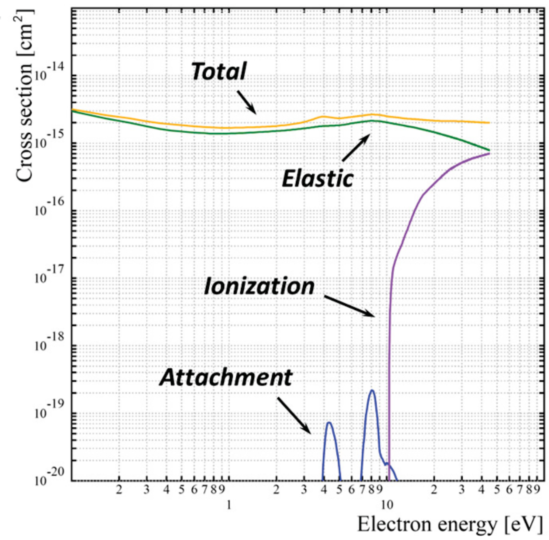

Figure 2.5: Cross-section of the main electron processes as a function of the electron kinetic energy in the operating gas of a sTGC detector, a mixture of n-pentane and CO_2 in the ratio 45:55. The total cross-section (yellow) is the sum of elastic collision, ionization and attachment processes. The cross-section for ionization is comparable to the cross-section for elastic scattering for electrons with a kinetic energy higher than 50 eV. The cross-sections are obtained from simulation [33].

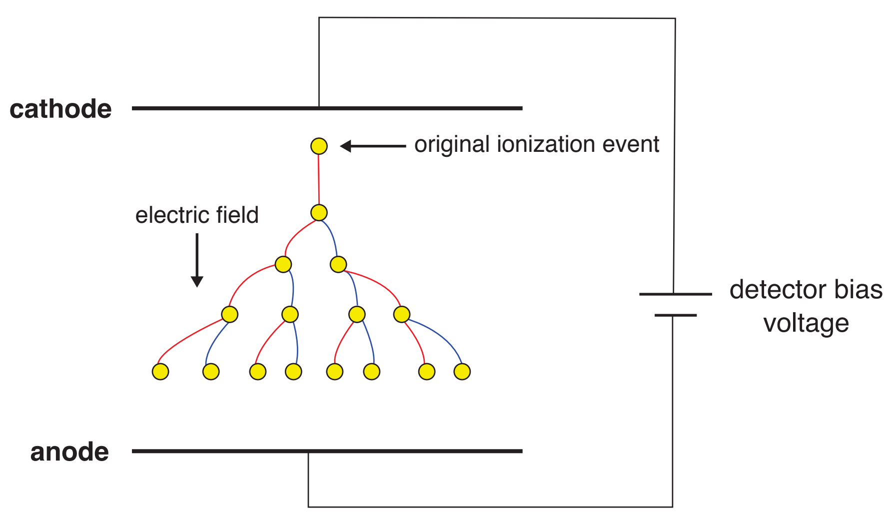

Figure 2.6: Schematic diagram of a Townsend avalanche. A strong electric field permeates the gaseous medium between the anode and the cathode. The yellow disks represent ionization events caused by an incident electron (red lines). Freed electrons (blue lines) produce more ionization events as they drift in the electric field. The total ionization approximately doubles at each step of the avalanche.

Avalanche yield

Variations in the number electrons making up a Townsend avalanche dN_e are proportional to the total number of electrons N_e in the avalanche

$$dN_e = \alpha N_e ds \tag{2.15}$$

where α is defined as the "first Townsend coefficient" and s is the length of the avalanche. The value of α depends on the electron mean free path and cross-section for ionization. The electron mean free path and cross-section both depend on the electric field intensity. Thus, the Townsend coefficient is commonly expressed as a function of s to account for electric field variations. The total number of electrons as a function of the avalanche size follows an exponential law

$$N_e(s) = N_0 e^{\alpha s} \tag{2.16}$$

where N_0 is the number of electrons before avalanche multiplication. The charge multiplication M, where $M = N_e/N_0$, is defined as the yield of a single primary electron in the avalanche. The value of M can be expressed in an integral form

$$M = \exp\left[\int_{s_1}^{s_2} \alpha(s)\ ds\right] \tag{2.17}$$

where $s_1 \leqslant s \leqslant s_2$ are the boundaries of the detector "critical region" in which the electric field is high enough for multiplication.

Excitation processes and photon production

Avalanche electrons give rise to gas excitation along with ionization. The excited medium can increase the electron yield if the operating gas is a Penning mixture [43]. Additionally, the excited gas molecules can emit an ultraviolet (UV) photon when they return to their lowest energy state. The UV photons then interact with other gas molecules and create photoelectrons that increase the avalanche multiplication. The gas multiplication including the contribution of photons is [32]

$$M_\gamma = \frac{M}{1 - P_\gamma M} \tag{2.18}$$

where P_γ is the probability of an avalanche electron to be associated with the production of one photon. Equation. 2.18 implies that gas breakdown occurs when $P_\gamma M \to 1$, called the Raether limit [44]. The Raether limit typically occurs at $\alpha s \sim 20$ or gains of the order of $M \sim 10^8$.

Photons propagating far from the original electron avalanche can degrade the spatial resolution of a gaseous ionization detector by spatially spreading the charge ionization and avalanche formation. If photon production is sufficient, the detector enters into the so-called Geiger mode of operation [32]. The Geiger mode is characterized by the formation of avalanches at multiple locations along the anode which severely limits the rate capabilities of the detector. Photons can also be produced when ions recombine on the detector cathode resulting in an afterpulse that can occur up to several microseconds after the original avalanche [45].

Photon production must therefore be moderated when operating at a gain $M > 10^2$ [46]. Photon moderation is achieved by the addition of a “quenching” gas. Quenching gases are made of molecules that convert the absorbed photon energy into vibrational levels of energy. Thus, they do not de-excite by photon emission. Typical gas quenchers are long molecules such as hydrocarbons, halides or alcohols [46].

Space charge

A Townsend avalanche heavily polarizes the gaseous medium because most electrons are located in the last mean free path while ions, that are much slower, stay behind. The polarization creates local "space charge effects" that reduce the local electric field thereby reducing the avalanche multiplication. Space charge can degrade the linearity of an ionization detector.

The phenomenological limit for gas amplification, at which space charge effects completely mitigate avalanche multiplication is given by the Raether limit [44].

For high rate operation of gaseous ionization detectors, the slow ions drifting to the cathode may generate global space charge effects that reduce the effective electric field of the gas volume resulting in particle detection inefficiencies.

2.4.2 Modes of operation

Gaseous ionization detectors have different modes of operation characterized by the total ionization yield in the gas volume. Different modes of operation can be achieved by varying the operating voltage V_0 as shown in Fig. 2.7.

At very low voltage (region I), the ionization pairs are likely to recombine before they drift in the gas volume. This mode of operation has no practical use for radiation detection.

If the voltage is set high enough to prevent recombination (region II), charge carriers drift towards the electrodes and contribute to the detector signal. The total charge collected is equal to the primary ionization N_0.

Above the threshold voltage V_T, gas amplification begins (region III). The gas multiplication grows exponentially with the voltage and the detector response is proportional to the primary ionization.

At even higher voltage (region IV), saturation of proportionality is observed because of space charge effects. This is the region of operation of sTGC detectors.

When the Raether limit is met (at $M > 10^8$), the dependence of the ionization yield on the primary ionization is lost (region V). Photon emission is significant and the detector operates in "streamer" mode. If the operating gas is not heavily quenched, photons propagate everywhere along the anode wire and the "Geiger-Müller" mode of operation is observed [47].

If space charge effects are not sufficient to reduce the effective electric field and stop the avalanche, a continuous avalanche, or glow discharge, is observed (region VI). This is the mode of operation of gas-discharge lamps, which is not useful for radiation detection.

2.4.3 Cylindrical ionization chambers

Cylindrical ionization chambers have a cylindrical cathode fitted with a thin coaxial anode wire and filled with the operating gas. The simple cylindrical geometry makes it possible to analytically derive expressions for the gain and the time development of a signal that are applicable to sTGC detectors.

A positive voltage is applied to the wire which generates a radial electric field pointing towards the cathode. A schematic of a typical cylindrical ionization detector is shown in Fig. 2.8. The electric field and potentials inside the cylindrical cathode are derived from the law of electrostatics

$$V(r) = \frac{V_0 \ln(r/r_a)}{\ln(r_i/r_a)} \qquad \vec{E}(r) = \frac{V_0}{r \ln(r_a/r_i)}\hat{r} \tag{2.19}$$

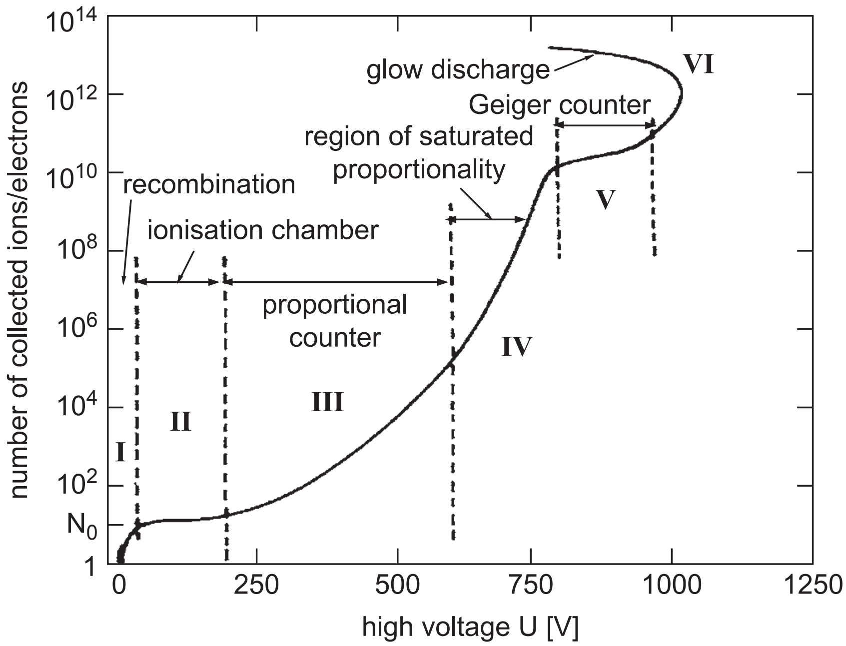

Figure 2.7: Ionization yield as a function of voltage for a typical ionization detector following the passage of a mip with a primary ionization $N_0 \sim 10$ [32].

where V_0 is the voltage applied to the anode wire, r is the radial distance from the center of the cylindrical cathode and $\hat{r}$ is the radial unit vector.

Following the passage of an ionizing particle, the ionization electrons drift toward the anode wire. Avalanche amplification occurs when ionization electrons reach the high electric field region in the vicinity of the wire. The avalanche is terminated when all electrons reach the anode.

The small amplification region of a cylindrical ionization chamber has many advantages. The gas amplification is independent of the initial position of the ionization electrons. This allows for a response proportional to the primary ionization. Furthermore, since the electric field increases as $1/r$ in the tube, a strong electric field is obtained close to the wire even when operating with a modest voltage.

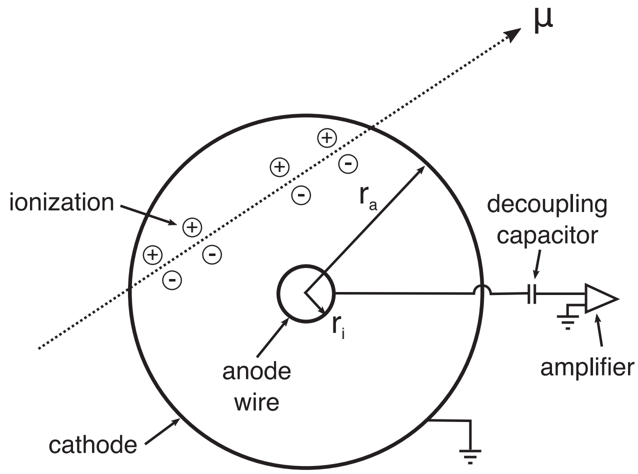

Figure 2.8: Cross-section schematic of a cylindrical ionization detector.

Avalanche multiplication

The total electron yield depends on the value of the first Townsend coefficient α in the amplification region. The value of α varies significantly as a function of the electric field and the gas mixture and pressure. The Korff's parameterization [48] suggests that α is proportional to the gas molecular density ρ_M and the mean electron energy ϵ_e

$$\alpha = k\rho_M\epsilon_e \tag{2.20}$$

where k is a constant specific to the operating gas mixture. Values of k are of the order of 10^6 cm$^2 \cdot$ mol$^{-1} \cdot$ cm^{-1} [14]. An expression for the gas multiplication of the cylindrical ionization detector shown in Fig. 2.8 is obtained using this approximation and following Rose and Korff [48, 49]. The integral of Eq. 2.17 is used with $s_1 = r_i$, the wire radius, and $s_2 = r_C$, the critical radius inside which the electric field is strong enough to initiate an avalanche. Following these assumptions, the gas multiplication is [14]

$$M = \exp\left[\sqrt{\frac{r_i k N C_l V_T}{\pi\varepsilon_0}}\sqrt{\frac{V_0}{V_T}}\left(\sqrt{\frac{V_0}{V_T}} - 1\right)\right], \tag{2.21}$$

where C_l is the linear capacitance of the cylindrical ionization detector and V_T is the "voltage threshold". The value of V_T relates to the critical radius according to the rule of three [14]

$$\frac{r_C}{r_i} = \frac{V_0}{V_T}. \tag{2.22}$$

Equation 2.21 suggests that no gas amplification occurs if $V_0 < V_T$. On the other hand, the gas amplification factor follows an exponential law for $V_0 \gg V_T$

$$M(V_0) \propto e^{C_l V_0}. \tag{2.23}$$

Another consequence of Eq. 2.21 is the exponential dependence of the gas multiplication factor on the inverse square root of the anode wire radius. This effect is demonstrated in Fig. 2.9 for a TGC detector irradiated with a ^{55}Fe radioactive source. For a fixed value of operating voltage, the gas multiplication factor is shown to increase with decreasing anode wire radius.

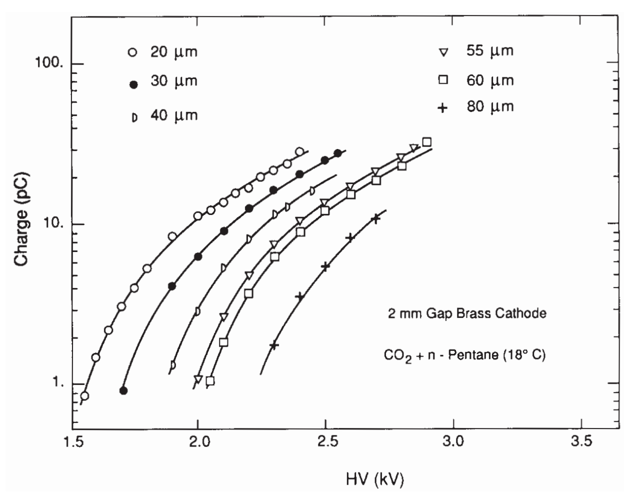

Figure 2.9: Impact of the wire diameter on the signal response of a TGC [50]. The charge saturation as a function of the operational high voltage (HV) is explained by space charge effects [51].

The approximation of Eq. 2.20 does not hold for an electric field of the order of 50 kV/cm. Furthermore, space charge effects become significant at gas gains higher than 10^5 [51]. The geometry of space charge effects can be complicated in general. Therefore, a simulation is required for an accurate description of a detector response at high gain or electric field [14].

Cylindrical ionization detector signal

The movement of ionization charges due to the electric field within the ionization detector induces a drop in voltage on the anode wire. Both ions and electrons produced during the avalanche contribute to the drop in voltage on the anode wire. The contribution of ions and electrons to the observed voltage drop is of the same sign, despite having opposite electric charge, because they drift in opposite directions. From the laws of electrostatics, the infinitesimal drop in voltage on the anode wire induced by a charge Q moving in the cylindrical detector is [14]

$$dv = \frac{Q}{CV_0}\frac{dV}{dr}dr \tag{2.24}$$

where C is the cylindrical ionization detector capacitance. Approximately half of the electron multiplication occurs in the final step of the avalanche [14]. Therefore, a good approximation is to assume that all charge is initially located at a radius $r_i + r_k$ where r_k is approximately the electron mean free path. Integrating Eq. 2.24 for both positive and negative charge carriers, the ratio of positive to negative signal contributions can be shown to be

$$\frac{v^-}{v^+} = \frac{\ln(r_i + r_k) - \ln r_i}{\ln r_a - \ln(r_i + r_k)}. \tag{2.25}$$

When applying Eq. 2.25 to the design values of an ATLAS monitored drift tube (described in Section 3.2.1) having $r_i = 25$ µm and $r_a = 15$ mm, and assuming $r_k = 1$ µm, the ratio is 0.6% which implies that the main contribution to the signal amplitude is from the movement of ions, and not electrons. When integrating Eq. 2.24 over an arbitrary time t and neglecting the electron contribution, the time evolution of the signal is obtained

$$v(t) = -\frac{Q}{4\pi\varepsilon_0 l} \ln\left(1 + \frac{\mu^+ C V_0}{\pi\varepsilon_0 p r_a^2} t\right) = -\frac{Q}{4\pi\varepsilon_0 l} \ln\left(1 + \frac{t}{t_0}\right) \tag{2.26}$$

where l is the axial length of the ionization detector and t_0 is the characteristic time of signal formation, defined by the last equality. Equation 2.26 does not apply beyond the time T required for ions to reach the cathode. The condition

$$v(t) \mid_{t \geq T} = -\frac{Q}{C} \tag{2.27}$$

must be met and provides a limit to the signal amplitude. The value of T is very large compared to the time development of the signal. Typically, half of the signal is generated in one-thousandth of T. Therefore, the readout electronics processing the raw detector signal typically collect the charge over a small duration sometimes referred to as the readout "integration time".

The term "integration time" can sometimes be found to refer to multiple related concepts. For example, in some contexts, it can be used to refer to the gate width, or time window, of a Charge to Digital Converter (QDC) during which charge is collected. It may also refer to the "characteristic time" of a bandwidth filter, also known as "shaper" [52]. In such a filter, the integration time is finely tuned to minimize the duration of the pulse thereby reducing dead time. A short integration time may, however, come at the price of a higher sensitivity of the detector response to noise, and a potential loss of electronic amplification called "ballistic deficit" [53]. Therefore, the integration time of a bandwidth filter must be optimized for the particular signal time dependence of the detector.

The simulated signal contribution of ions and electrons as a function of the integrated time for a sTGC detector is shown in Fig. 2.10. The ion signal clearly follows the logarithmic dependence predicted by Eq. 2.26. The electron signal is already saturated after a few nanoseconds. The electron signal contribution dominates only in the first few nanoseconds of the signal development, after which, the dominant contribution to the change in voltage measured on the anode wire is due to the movement of positive ions.

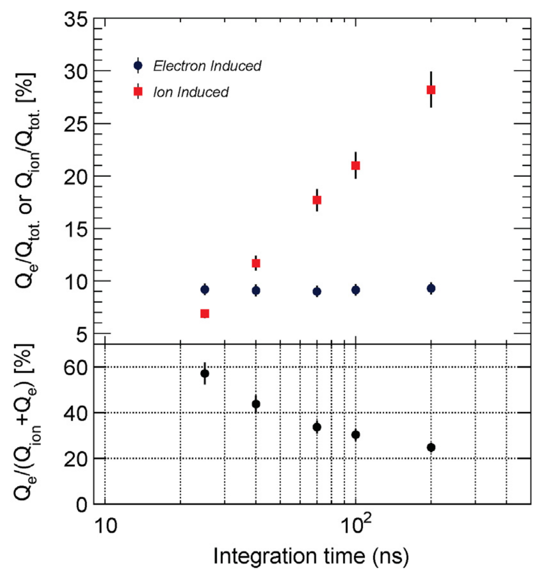

Figure 2.10: Signal contribution of ions and electrons for a sTGC detector as a function of the integration time [33]. The bottom plot highlights that the electron contribution is dominant only for very short integration times. The resulting voltage signal is $v = (Q_e + Q_{ion})/C$ where C is the detector capacitance.

2.4.4 Multiwire chambers

Multiwire chambers are gaseous ionization detectors made of many equidistant anode wires sharing the same gas volume [13]. Small-strip Thin Gap Chambers are an example of multiwire chambers. The gas volume is located between parallel cathode planes. A multiwire chamber can measure the position of ionizing particles over a large area and has the benefit of having all its anode wires inside the same gas volume. The position of an incident particle can be deduced from the signal induced on anode wires closest to the primary ionization.

The geometry of multiwire chambers varies greatly. The electric field close the anode wires is, however, similar to that of a cylindrical ionization counter. The electric field lines and equipotentials of a typical multiwire chamber are shown in Fig. 2.11. As a result, the detector signal development is also expected to be similar to that of a cylindrical ionization chamber since most of the signal is generated when the charge carriers are in the vicinity of one of the anode wires [14].

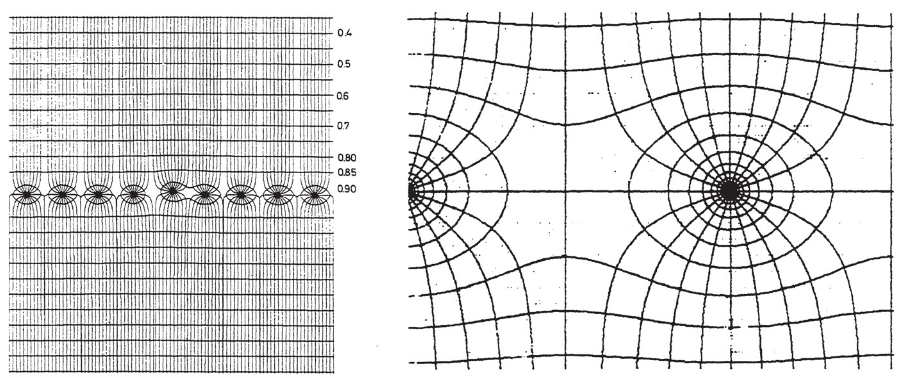

(a) (b)

Figure 2.11: (a) Electric field lines and equipotentials in the gas volume of a multiwire chamber. The electric potential relative to the anode wire potential, or value of V_0, is indicated. The effects of a minor displacement of one anode wire are shown. (b) Enlarged view of the same figure in the vicinity of a wire [14].

2.4.5 Cathode readout

For tracks perpendicular to the multiwire chamber plane, the avalanche signal is typically observed on a single anode wire. Therefore, the detector spatial resolution is directly proportional to the wire pitch s and given by $\sigma = s/\sqrt{12}$ [14]. Stable detector operations are more difficult to achieve with $s < 2$ mm [14] limiting the resolution of a multiwire chamber with wires readout to approximately 600 µm.

In a planar multiwire chamber, the change in voltage produced by the movement of charge carriers is induced on both anode wires and the cathode planes. The signal induced on each cathode plane is inverted and is half the amplitude of the voltage drop observed on the anode wires. If the cathode plane is segmented into strips coupled to ground, the signal induction is shared between the strips. The schematic of a multiwire chamber with a segmented cathode is shown in Fig. 2.12, along with a sketch of the signal induced on each strip. A centroid finding technique is used to deduce the spatial location where a charged particle has traversed the detector volume from the induced charge profile. Readout from a segmented cathode provides better tracking performances than wire readout [54] because the spatial resolution is not limited by the readout pitch.

The spatial coordinate parallel to the wires can be measured if the strips are made to be perpendicular to the wires. For a readout strip segmentation parallel to the wire, the spatial resolution is typically still limited to the wire pitch because the avalanche induction is centred on the wire and spatial information is related to the charge induction by the avalanche. At low gain, the asymmetry of the avalanche around the wire can be exploited for more precision; however, effects of the avalanche asymmetry are lost at high gain [55, 56].

Charge induction profile

The cathode current element over an infinitesimal distance λ along y scaled to the anode-cathode spacing and using the coordinates system of Fig. 2.12 is [57]

$$dI_C(t, \lambda) = I_a(t)\Gamma(\lambda)\, d\lambda \qquad \text{where } \lambda = \frac{y}{h} \tag{2.28}$$

where $I_a(t)$ is the time evolution of the signal, which does not depends on the avalanche

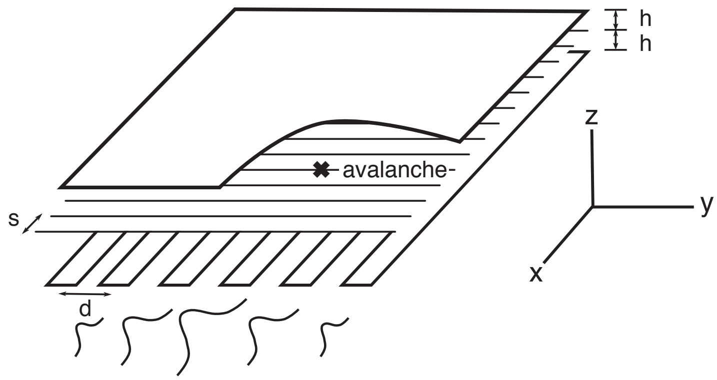

Figure 2.12: Schematic of a multiwire chamber with a segmented cathode. The cross highlights the avalanche position on one of the anode wires. The signal induction on each cathode strip is sketched [57].

position, and h is the anode-to-cathode spacing. The signal time evolution corresponds to the expression of Eq. 2.26. The unitless function $\Gamma(\lambda)$ is the signal induction distribution. Its normalization is given by [57]

$$\int_{-\infty}^{\infty} \Gamma(\lambda)\, d\lambda = \frac{1}{2} \tag{2.29}$$

which assumes that the charge induction on a single cathode is half that on the anode wires. An approximate expression for $\Gamma(\lambda)$ assuming a single avalanche was derived by Gatti [57]

$$\Gamma(\lambda) = K_1 \frac{1 - \tanh^2 K_2\lambda}{1 + K_3 \tanh^2 K_2\lambda} \tag{2.30}$$

where K_1 and K_2 are constant related to K_3 by

$$K_1 = \frac{K_2\sqrt{K_3}}{4\,\mathrm{atan}(\sqrt{K_3})} \qquad K_2 = \frac{\pi}{2}\left(1 - \frac{\sqrt{K_3}}{2}\right) \tag{2.31}$$

The parameter K_3 is a constant that depends on the anode wires radius, the anode-cathode spacing and the wires pitch. Gatti's approximation assumes the azimuthal symmetry of the avalanche and small anode wires compared to the overall dimensions of the detector

Numerical calculations of K_3 were performed by Mathieson and Gordon [58]. For the geometry of a sTGC detector they obtained $K_3 \sim 0.7$. As shown in Fig. 2.13(a), a Gaussian function constitutes a good approximation of the Gatti function. The actual $\Gamma(\lambda)$ distribution combines the effects of all avalanches created by the primary ionization but it should still resemble a Gaussian function.

Effect of a resistive cathode

Readout strips that also act as a segmented cathode are undesirable as they create limitations in the detector design [59]. In order to decouple the detector cathode surface from the readout elements, a capacitive layer with a resistive coating can be inserted in front of the readout strips. The resistive coating surface is grounded and constitutes the actual detector cathode surface. In such a design, the readout electrodes are insulated from the cathode surface. The readout electrodes are directly connected to the readout electronics and are, therefore, virtually grounded.

A resistive coating can be modelled as an array of multiple RC [2] filters which effectively spreads the signal further beyond the natural charge spread originating from the avalanche formation in the detector. The cathode "transparency" is the property that allows the resistive cathode to spread charge [60]. The transparency is a function of the graphite square sheet resistance [3] and the surface capacitance of the capacitive film (mea-

2. Resistor–capacitor circuit.

3. The cathode sheet resistance is obtained by measuring the resistance between two probes touching the cathode. The numerical value of the measured resistance is equal to the sheet resistance. The sheet resistance is invariable when changing the positioning of the probes. The sheet resistance has units of "ohms per square" ($\Omega/\square$) which is dimensionally equal to an ohm.

sured in F/m^2). The transparency can be tuned to match the optimal signal spread for the detector without changing its geometry. For example, the graphite coating sheet resistance of the current ATLAS TGC, described in Section 3.2.1, was tuned to limit the charge spread over more than one strip [61].

The profile of the charge spread of a point charge on a resistive cathode can be described by the one-dimensional solution to the diffusion equation [33]

$$\rho_Q(y,t) = \sqrt{\frac{\tau}{4\pi t}} \exp\left(-\frac{\tau y^2}{4t}\right), \tag{2.32}$$

where $\rho_Q(y,t)$ is the linear charge density, τ is the characteristic time and t is the time after the charge creation. The value of τ is a function of the detector transparency. The charge collected by the electrodes as a function of time can be expressed as the convolution of Eq. 2.30 and Eq. 2.32. An example of the charge induction profile at different times t is shown in Fig. 2.13(b).

Simulation studies show that Eq. 2.30 and the charge diffusion model of Eq. 2.32 accurately describes the signal formation in a TGC detector [33].

The ionization current creates a potential drop in the resistive coating by virtue of Ohm's law. This effect causes a drop in the detector effective operating voltage. The effect can momentarily lower the hit efficiency of the detector during high rate operations [62].

Differential non-linearity

A systematic effect, called the "differential non-linearity", can bias the reconstructed position of a charged particle traversing the gas volume. The existence of this bias is due to sampling effects of the charge profile and the capacitive coupling between strips. The differential non-linearity bias is a function of the avalanche position with respect to the inter-strip spacing [63]. An example of the effect of differential non-linearity on the re-

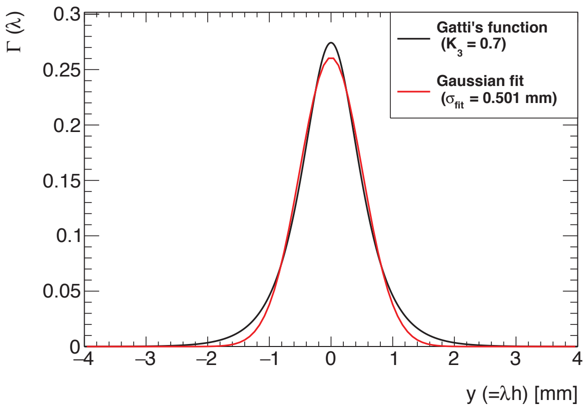

(a)

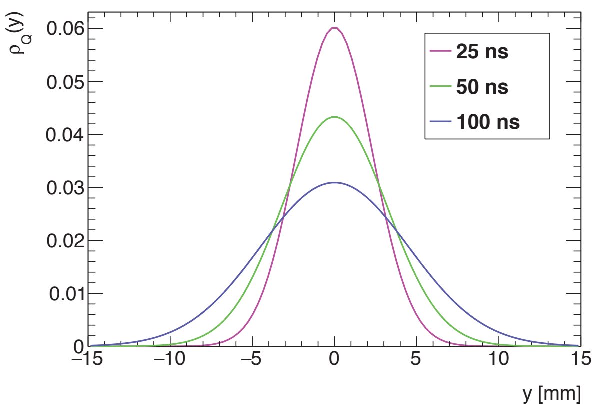

(b)

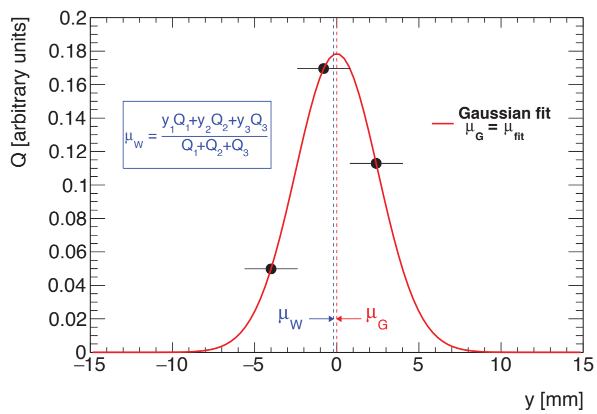

(c)

Figure 2.13: (a) Charge induction on the cathode of a sTGC detector predicted by Gatti's formula. (b) The effect of the resistive coating on the charge distribution as a function of time for a graphite time constant of 10 ns. (c) Example of the charge induced on three consecutive readout strips in a sTGC detector as a function of the strip position. The centroid positions obtained using the Gaussian fit (μ_G) and weighted average (μ_W) algorithms, described in Chapter 5, are shown. The charge cluster nominal position is at $y = 0$ and the strip pattern is shifted by 1.6 mm. The difference between the nominal cluster position and the reconstructed positions is due to the differential non-linearity.

constructed position of a charge cluster is shown in Fig. 2.13(c).

A number of techniques were developed to reduce to the magnitude of the differential non-linearity bias at the hardware level [64, 65]. The differential non-linearity bias can also be reduced by the appropriate choice of centroid finding algorithm [63, 66].

Differential non-linearity effects are observed with sTGC detectors because the readout strips are large with respect to the width of the charge induction. Measurements of the differential non-linearity bias with sTGC detectors were performed in a test-beam setup [67, 68] and with cosmic rays (Chapter 5 of this dissertation). The analysis of Chapter 5 presents a technique to correct the differential non-linearity bias and improve track reconstruction performance.

3

The ATLAS experiment at CERN

This chapter motivates the characterization studies of sTGC detectors for the ATLAS upgrade taking place during the 2019-2020 LHC shutdown. The chapter starts with an overview of the Large Hadron Collider in Section 3.1. It follows with a description of the ATLAS detector in Section 3.2 with an emphasis on the muon detector system, the so-called muon spectrometer. A description of the ATLAS upgrade, whose purpose is the improvement of the forward muon identification capability of the muon detector system in anticipation for the LHC high luminosity operations, is given in Section 3.3.

3.1 The Large Hadron Collider

The Large Hadron Collider (LHC) [2] is a particle accelerator located at the CERN laboratory, straddling the border between France and Switzerland. The accelerator operates inside an underground tunnel of 27 km circumference at a depth of 100 m. The LHC tunnel was dug initially for the purpose of the Large Electron-Positron collider (LEP) [23]. The LEP collider operated from 1989 until 2000. The LHC construction started in 1998 and finished in 2008. The LHC still operates to this day. A continuous operation of the accelerator, with only periodic shutdowns for maintenance or upgrades, is planned until the year 2037.

The LHC is designed to accelerate protons in counter-rotating beams. Proton-lead, lead-lead and xenon-xenon collisions were also performed since the start of LHC operations in 2010. The accelerated particles are stored in up to 2808 bunches [1] distributed

1. Accelerated particles at the LHC are not uniformly distributed along the circumference of the LHC ring. Instead, the particles are grouped into so-called bunches due to the effect of the longitudinal oscillating voltage responsible for increasing the kinetic energy of the particles. The number of bunches around the LHC ring is constant and depends on the frequency of the oscillating voltage.

over the LHC circumference. Particle bunches cross at 25 ns intervals at the LHC interaction points. This time interval is defined as the "bunch crossing time". The LHC design collision center-of-mass energy and instantaneous luminosity [2] are $\sqrt{s} = 14$ TeV and $\mathcal{L} = 10^{34}$ cm^{-2} s^{-1} respectively.

The LHC has a total of four interaction points occupied by the four main LHC detectors: ALICE [69], ATLAS [3], CMS [70] and LHCb [71]. The approximate location of the main LHC experiments with respect to the LHC ring and the accelerator complex is shown in Fig. 3.1.

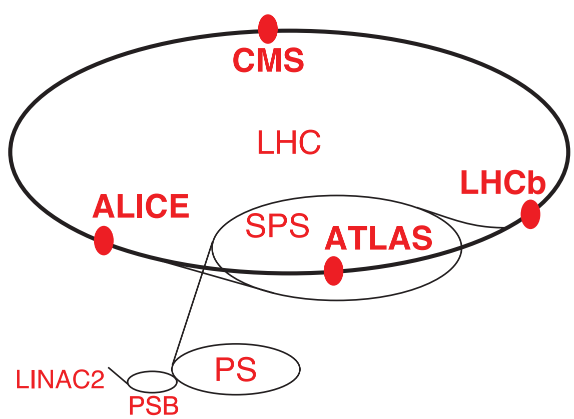

Figure 3.1: Schematic diagram of the LHC and its injectors [72]. The approximate location of the main CERN experiments that are using the LHC beams is also shown. The accelerator complex includes the Linear Accelerator 2 (LINAC2), the Proton Synchrotron Booster (PSB), the Proton Synchrotron (PS), the Super Proton Synchrotron (SPS) and the Large Hadron Collider (LHC).

2. The instantaneous luminosity [5] for two particle bunches crossing head-on with frequency f_{coll} and containing n_1 and n_2 particles is obtained from the expression

$$\mathcal{L} = f_{\mathrm{coll}} \frac{n_1 n_2}{4\pi\sigma_x\sigma_y} \tag{3.1}$$

where σ_x and σ_y characterize the root mean square (RMS) transverse beam sizes in the coordinates perpendicular to the beams assuming the beams are traveling along the z-axis.

3.1.1 The accelerator complex

Protons are accelerated by a sequence of injectors before they reach the main LHC ring. Injectors are particle accelerators that boost the protons to a sufficient momentum in order to be accepted by the next injector in the sequence. A schematic diagram of the injection sequence in shown in Fig. 3.1.

The LHC source of protons is molecular hydrogen converted into H^+ ions by ionizing and splitting H_2 molecules. Protons are initially accelerated by the Linear Accelerator 2 (LINAC2) up to an energy of 50 MeV and are arranged into bunches before being transferred to the Proton Synchrotron Booster (PSB). The PSB increases the protons energy up to 1.4 GeV prior to their injection into the Proton Synchrotron (PS). There, the protons are accelerated up to 26 GeV and injected into the Super Proton Synchrotron (SPS). Finally, the protons are accelerated up to 450 GeV in the SPS and are injected into the LHC. The LHC increases the energy of the protons up to the final value before they are made to collide at the interaction points.

3.1.2 LHC operation and upgrade

Multiple upgrades of the LHC and the accelerator complex are planned until the decommissioning of the accelerator currently scheduled for approximately 2037. An overview of the LHC schedule is shown in Fig. 3.2 which highlights three major upgrade periods, the Long Shutdowns (LS) and the End of Year Technical Stop (EYETS). The schedule is briefly summarized below.

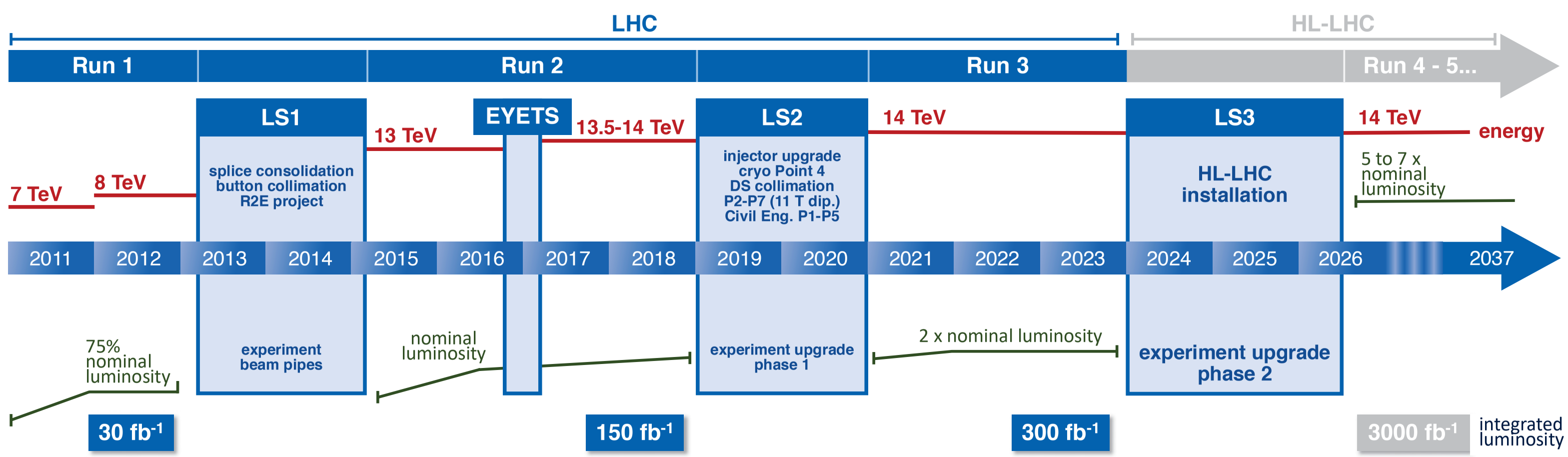

Figure 3.2: LHC operation schedule [73]. Each block indicates the LHC consolidation works scheduled during each individual upgrade period: Long Shutdown 1 (LS1), End of Year Technical Stop (EYETS), Long Shutdown 2 (LS2) and Long Shutdown 3 (LS3).

The LHC delivered a total integrated luminosity [3] of $\mathcal{L}_{\text{int}} = 30$ fb^{-1} to the ATLAS experiment during its first years of physics operation from 2010 to 2013. During this running period, the center-of-mass energy was kept at $\sqrt{s} = 8$ TeV or below with a luminosity achieved using a bunch crossing time of 50 ns, larger than the nominal value of 25 ns.

The Long Shutdown 1 (LS1) followed for a period of two years to prepare the accelerator for a gradual increase in luminosity and energy up to their nominal values. More than three years of almost continuous operation, only briefly interrupted by the EYETS, have been taking place since LS1. Approximately 150 fb^{-1} of collision data will have been collected by the end of 2018. The LHC achieved its design luminosity in 2016 and has since surpassed it [4].

The Long Shutdown 2 (LS2) is scheduled to start at the end of 2018 and to last for two years. During this period, the performance of the LHC injectors will be improved resulting in the ability to operate the LHC with a bunch crossing time of 25 ns. These modifications will increase the LHC luminosity up to at least twice its nominal value.

The Long Shutdown 3 (LS3) is scheduled to begin three years after the end of LS2. During this shutdown period, the machine will be upgraded to its High-Luminosity configuration (HL-LHC). After this upgrade, the luminosity is expected to reach up to seven times the nominal value. If all beam parameter targets are successfully achieved, the LHC will collect over 3000 fb^{-1} of data by 2037.

The anticipated rate of collisions in the coming years will result in an increased

3. The integrated luminosity $\mathcal{L}_{\text{int}}$ is the integral of the instantaneous luminosity with respect to time

$$\mathcal{L}_{\text{int}} = \int \mathcal{L}\, dt. \tag{3.2}$$

The number of detected events N is related to the cross-section of the physics process of interest σ and the integrated luminosity with the expression $N = \sigma\mathcal{L}_{\text{int}}$. Thus, the integrated luminosity typically relates to the statistical error on a physics measurement.

4. The maximum instantaneous luminosity delivered by the LHC was $\mathcal{L} = 2.14 \times 10^{34}$ cm^{-2} s^{-1} at the time of writing of this dissertation [74].

particle flux and detector occupancy for the LHC experiments. Thus, major hardware upgrades of the LHC experiments are planned in order to be able to benefit from the improved LHC performance. One of these upgrades consists in the replacement of parts of the muon detector system of the ATLAS experiment. A description of this upgrade is found in Section 3.3.

3.2 The ATLAS experiment

The ATLAS experiment [3] is a detector located at one of the LHC interaction points. The detector is cylindrical with a 4π coverage of the interaction region. The detector was initially optimized to operate during proton-proton collisions up to a peak instantaneous luminosity of 10^{34} cm^{-2} s^{-1}. The overall dimensions of ATLAS are 25 m in height and 44 m in length for a total weight of roughly 7000 tons. A cut-away view of the ATLAS detector is shown in Fig. 3.3. ATLAS can be divided into five major subsystems: the magnet systems, the inner detector, the calorimeters, the muon spectrometer and, the trigger and data acquisition system. The detector subsystems are essentially composed of multiple concentric cylindrical layers centred around the interaction point. They are immersed in the strong magnetic field generated by the magnet systems. All subsystems are briefly described below. The muon spectrometer, which is directly relevant for the research work performed in this dissertation, is separately discussed in Section 3.2.1.

The ATLAS coordinate system is defined as follows. The origin is located at the nominal interaction point. The z-axis is defined to be in the direction of the beam line, the y-axis points upwards and the x-axis points towards the center of the LHC ring. If cylindrical coordinates are used, ϕ is the azimuthal angle around the beam line and r is the shortest distance from the beam line. Observables labelled "transverse", such as the transverse momentum p_T, correspond to their value projected onto the x-y plane. The

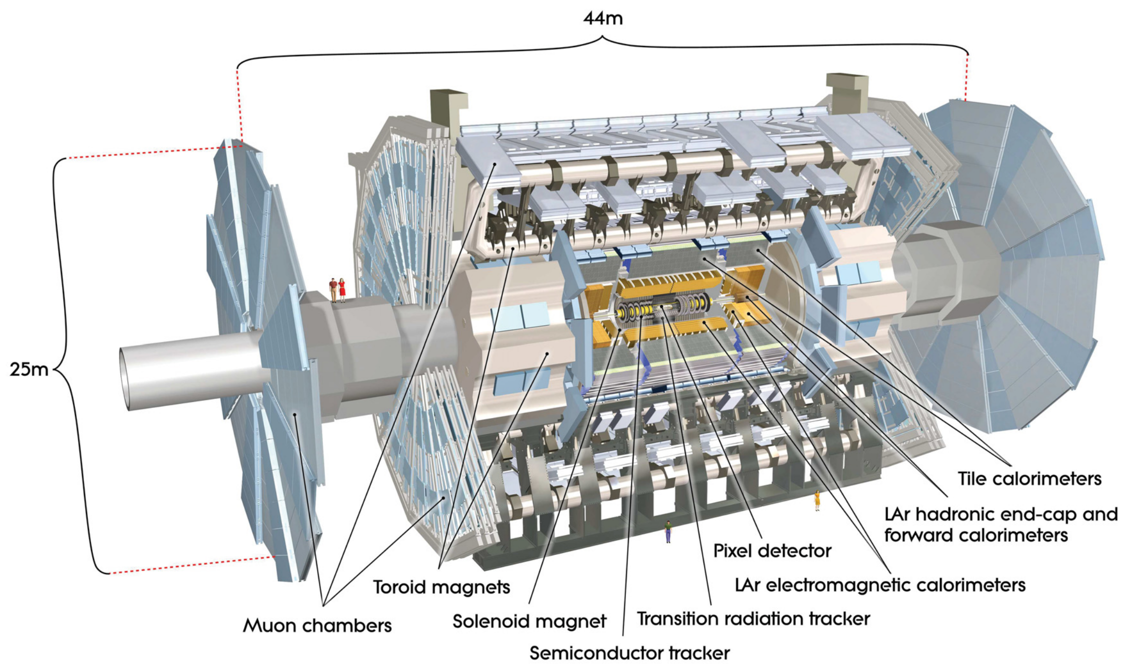

Figure 3.3: Cut-away view of the ATLAS detector. The major detector subsystems are identified.

pseudorapidity [5] is a function of the polar angle θ (defined by $\tan\theta \equiv r/z$) and is defined as $\eta = -\ln(\tan(\theta/2))$.

The ATLAS magnet systems [75–78] generate a strong magnetic field that bends the trajectory of charged particles by the action of the Lorentz force. The trajectories of charged particles are precisely measured by the inner detector and the muon spectrometer. The particle momentum and charge are deduced from the curvature of the reconstructed particle trajectory. One solenoid magnet, positioned around the beam pipe, generates a 2 T axial magnetic field that permeates the inner detector. Toroid magnets are placed just outside the calorimeters and generate a 4 T azimuthal magnetic field. The toroid magnets are arranged in an 8-fold symmetry around the beam pipe. The geometry of the ATLAS detector subsystems is driven by this magnet configuration.

5. The pseudorapidity is often used rather than the polar angle θ because differences in pseudorapidity are Lorentz invariant under boosts along the longitudinal axis.

The inner detector [79–81] is used for precisely reconstructing the trajectory of charged particles in the vicinity of the beam pipe. The inner detector also assists in electron/pion identification and hadron flavour classification. It is made of a collection of silicon-based detectors and gas ionization straw tubes. The detector modules are arranged in a cylindrical geometry axially centred on the beam pipe. The overall dimensions of the inner detector are approximately 5.3 m in length and 2.5 m in diameter.

The calorimeters [82, 83] are used to measure the energy and trajectory of photons, electrons and hadrons. These particles interact with the calorimeters by initiating a shower; that is a cascade of secondary particles. The incoming and secondary particles both interact with the material of the calorimeter to create new secondary particles of lesser energy. The cascade stops when the particles making the shower do not have a sufficient energy to create more secondary particles. The calorimeters are optimized to completely absorb the showers. The incoming particle energy is related to the total ionization left by the shower in the calorimeter. Electrons and photons initiate cascades called electromagnetic showers. Cascades initiated by hadrons combine a hadronic component, that consists of secondary hadrons, and an electromagnetic component, that consists of secondary electrons and photons. ATLAS calorimeters are specialized in the detection of either type of showers. Electromagnetic calorimeters are located closer to the interaction point than hadronic calorimeters. The calorimeters completely cover the inner detector and are located between the solenoid magnet and the toroid magnets. The calorimeters collectively make a cylinder of 14 m in length and 8 m in diameter.

The trigger and data acquisition system [84, 85] controls the data flow between the detector subsystems and permanent data storage. Proton bunch crossing occurs at a maximum rate of 40 MHz at the ATLAS interaction point. The trigger system identifies what bunch crossings resulted in physics processes of interest. Only detector data from the bunch crossings selected by the trigger system are saved to permanent storage. The trigger system architecture is divided in two levels: the Level-1 (L1) trigger and the High-Level Trigger (HLT). The L1 trigger is hardware based, meaning it uses custom electronics and FPGAs [6] to quickly process detector hits. The L1 trigger decision is based on hits from the calorimeters and muon detector systems only. The maximum L1 trigger rate is 100 kHz, limited by the on-detector electronics readout rate capabilities. Upon an L1 trigger accept signal, on-detector data tagged with the selected bunch crossing are transferred to a computing farm. The HLT is implemented on a computing farm with commercial off-the-shelf computer processors. Data from all detector subsystems are available for HLT processing. Detector data are transferred from the computing farm to permanent storage upon an HLT accept. The maximum HLT rate is of the order of 1 kHz, limited by the offline data storage capabilities.

3.2.1 The ATLAS Muon Spectrometer

The main purpose of the muon spectrometer is the momentum measurement of muons, originating from the interaction point, based on their Lorentz deflection as they traverse the magnetic field generated by the toroid magnets. The muon spectrometer constitutes the outermost detector layer of ATLAS. The muon spectrometer is divided in height octants both in the barrel region and the end-caps to match the toroid magnets geometry. Some of the detector modules of the muon spectrometer are located over and in between the toroid magnets coils with some overlaps to minimize gaps in detector coverage.

A schematic of the arrangement of muon detector modules in the x-y and y-z planes of ATLAS is shown in Fig. 3.4. The barrel modules are arranged in three concentric cylindrical stations located at approximately $r = 5$ m, 7.5 m, and 10 m. The stations are named barrel inner (BI), barrel middle (BM) and barrel outer (BO) respectively. The end-cap modules are arranged in four disk-shaped stations located at $z = 7.4$ m, 10.8 m, 14 m,

6. Field-Programmable Gate Array.

and 21.5 m. The stations are named end-cap inner (EI), transition end-cap (EE), end-cap middle (EM) and end-cap outer (EO) respectively. The octants making a muon station typically contain small (denoted S) and large (denoted L) detector modules that overlap to minimize gaps in detector coverage at the transition between octants. As explained later in Section 3.3, some parts of the end-cap inner muon station will be replaced during the LHC Long Shutdown 2.

Each muon station combines multiple detector technologies specialized in either triggering or precision muon trajectory measurement. Monitored Drift Tubes (MDT) [86, 87] and Cathode Strip Chambers (CSC) [88] are used as precision detectors. The MDT detector modules are used in both the barrel and end-cap regions while CSC modules are used in the end-caps only. Resistive Plate Chambers (RPC) [89, 90] and Thin Gap Chambers (TGC) [24] are used for triggering. The RPC and TGC detector modules are respectively located in the barrel and the end-cap regions. An overview of the different muon detector technologies is given later in this section.

The role of precision modules is to provide an excellent measurement of the muon trajectory in the bending plane. Measurements from precision modules are used to deduce the muon momentum with a resolution of approximately 10% for $p_T = 1$ TeV/c muons [61]. The trigger modules, on the other hand, serve the following purposes:

- Online muon momentum measurement for the trigger system.
- Measurement of the muon track coordinate in the direction orthogonal to the bending plane used for offline muon reconstruction.
- Identification of the bunch crossing number to which hits in the precision modules are associated.

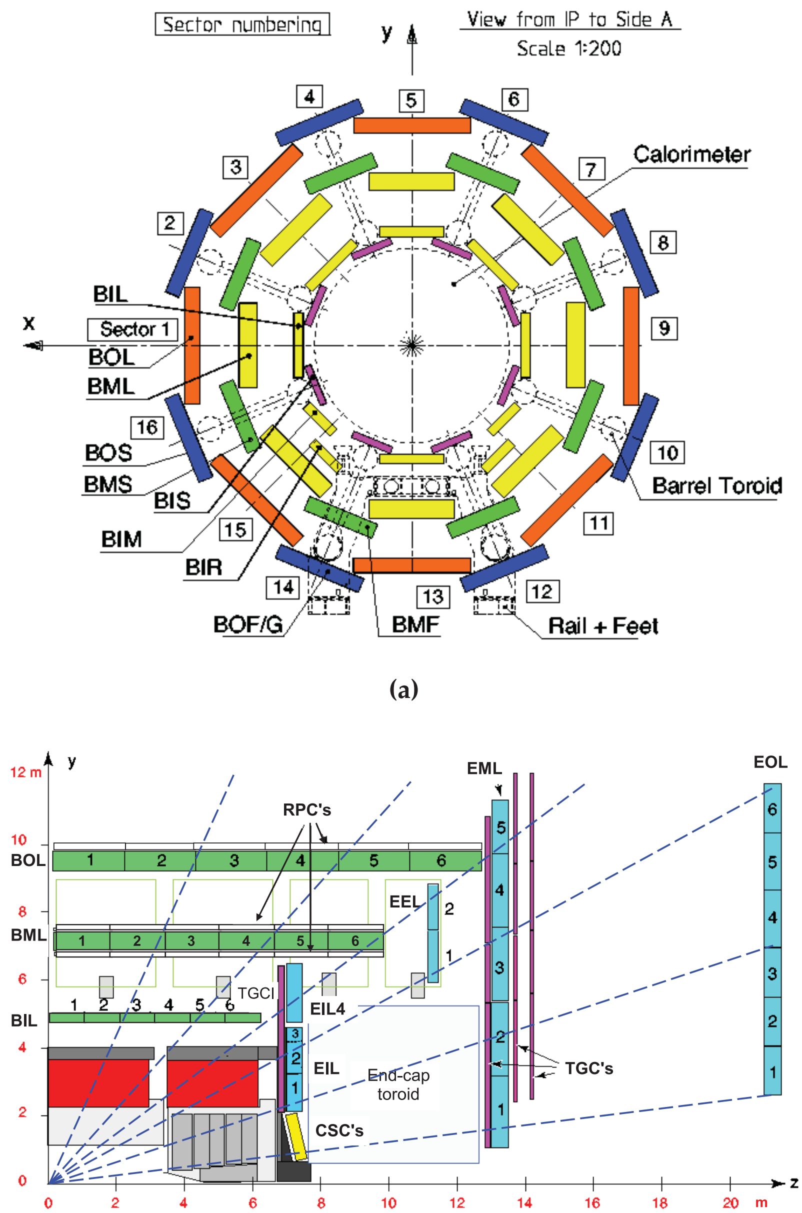

(a)

(b)

Figure 3.4: Projection of the current ATLAS muon detector system [3] (a) on the x-y plane and (b) on the y-z plane. The muon stations and module size are denoted using 3-letter acronyms. The first letter indicates a Barrel (B) or End-cap (E) station. The second letter indicates the position of the station relative to the interaction point. Four layers of stations are defined: Inner (I), Middle (M), Outer (O) and transition end-cap (E). Finally, the third letter indicates the module size typically named Small (S) or Large (L). End-cap small modules are not seen in the y-z projection because they are located at a different ϕ position. Special modules are positioned around the support structures, or "feet", of the muon spectrometer to minimize the loss of coverage in these regions. The special modules are denoted with the letters M, R, F or G depending on their exact dimensions and location.

Monitored Drift Tubes

Monitored Drift Tubes (MDT) [86,87] are cylindrical ionization detectors that measure the muon track position based on the time of arrival of the earliest ionization electron on the anode wire. A single MDT tube cannot unambiguously determine the angle of a track. Therefore, MDT modules consist of six layers of tubes allowing for the reconstruction of a muon trajectory. The multi-layer configuration also provides an improved redundancy and spatial resolution. Monitored Drift Tubes are made of aluminum cylinders 30 mm in diameter fitted with a coaxial tungsten-rhenium wire of 50 μm diameter. The filling gas is a mixture of argon and CO_2 in the ratio 93:7 at a pressure of 3 bars. The filling gas contains a small admixture of water vapour (<1000 ppm) which improves the spatial resolution and reduces variations of electron drift properties as a function of the magnetic field [91]. The operating voltage is 3080 V for an operation in the proportional mode.

The MDT technology has many advantages explaining why it was chosen as the main precision chamber in ATLAS. Monitored drift tubes are simple to fabricate and feature a rigid construction with predictable mechanical deformations. Monitored drift tube modules have a high redundancy, a single tube failure having small consequences on the module overall performance. The dependence of the MDT modules spatial resolution on the muon track angle is very small because of the azimuthal symmetry of each individual tube. The spatial resolution of a single MDT is 80 μm and 35 μm for a 6-layer module.

Cathode Strip Chambers

Cathode Strip Chambers (CSC) [88] are multiwire proportional chambers with segmented cathodes readout. The ATLAS CSCs operate with a mixture of argon and CO_2 in the ratio 80:20. Anode wires are made of gold-plated tungsten with 3% rhenium and have a diameter of 30 μm. The wire pitch is 2.54 mm and is equal to the cathode-anode spacing. The operating voltage is 1900 V which corresponds to a gas gain of 4×10^4 for an operation in the proportional mode.

The CSC cathodes are segmented into strips on both sides of the gas volume. The strip patterns are perpendicular to each other to provide two coordinates of the muon track. A CSC can resolve two muon tracks by matching the total charge read-out by the opposite cathodes. The strip pattern alternates between one readout and two larger intermediate strips. The readout strips are connected to the readout electronics while intermediate strips are capacitively coupled to the readout strips. This particular strip pattern reduces differential non-linearity effects without increasing the number of readout channels. The spatial resolution of a single CSC chamber is 60 μm in the bending plane. In the non-bending plane, the spatial resolution is limited by the wire pitch to approximately 2.5 mm.

Cathode strip chambers can operate at a higher particle flux than MDTs without suffering from significant efficiency and spatial resolution degradations [61,92]. The high operating pressure and large drift volume of MDTs slows the evacuation of avalanche ions and makes MDTs particularly sensitive to space charge effects that vary the effective electric field in a tube. The MDT spatial resolution depends on the stability of the electron drift time and the gas amplification that are both a function of the electric field. In ATLAS, CSCs are therefore used rather than MDTs in areas where the particle flux is above 200 Hz/cm^2 (at the nominal ATLAS luminosity) which corresponds to the forward regions of the end-cap inner muon stations. There, muons typically cross 4 CSC layers.

Resistive Plate Chambers

A Resistive Plate Chamber (RPC) [89,90] is a gaseous parallel electrode-plate detector. The gas volume is bounded by graphite coated electrodes that generate a uniform electric field. Thus, gas multiplication occurs simultaneously for all ionization clusters left by a muon in the gas volume. The RPC signal is, therefore, a short and unique pulse. The RPC gas gain is not well defined because it varies as a function of the distance of the primary ionization from the anode plane. RPCs operate at a voltage of 9.8 kV with a gas mixture of $C_2H_2F_4$/iso-C_4H_{10}/SF_6 in the ratio 83:7:10. The gas gap thickness is 2 mm.

Readout strips are located on either side of a gas volume and are isolated from the graphite electrodes with a PET[7] foil. The strips on either side of a gas volume are orthogonal providing a two-coordinate measurement of a charged particle traversing an RPC. Each RPC module has two gas volumes, and there are three layers of RPC modules surrounding ATLAS. Therefore, high-p_T muons typically traverse six RPCs. Unlike other ATLAS muon chambers, RPCs do not have wires which has the advantage of a simpler construction. They have a time jitter better than 1.5 ns. The spatial resolution achieved is approximately 1 cm, adequate for a trigger chamber.

Thin Gap Chambers

Thin Gap Chambers (TGC) [24] are multiwire chambers operating in the quasi-saturated mode and featuring cathode readout. The operating principles of TGCs are very similar to those of small-strip Thin Gap Chambers (sTGC), described in detail in Section 3.3.3. Specificities of the current ATLAS TGCs are discussed here.

Muon trajectory measurements in the bending plane are performed by the anode wires. Anode wires are read out in groups of 6 to 31 which corresponds to a readout pitch varying between 10.8 mm and 55.8 mm. Anode wire grouping is optimized to limit the number of readout channels while keeping the spatial resolution sufficient for the purposes of muon trigger. In the end-cap regions, the muon momentum p is up to six times higher than p_T, the observable of interest for the trigger system. Thus, a smaller granularity is required at high $|\eta|$ to improve the p_T resolution. The capability of TGCs

7. Polyethylene terephthalate.

to conveniently vary their readout pitch without drastically changing the detector design partly explains why TGCs, rather than RPCs, are used in the end-caps.

One cathode per gas volume is segmented into strips that measure the azimuthal coordinate of the muon track. The strip width varies so as to obtain an azimuthal granularity of 2-3 mrad. The other cathode is not segmented. The cathode graphite sheet resistance is 1 MΩ/□ for the end-cap middle station and 0.5 $M\Omega/\Box$ for the end-cap inner station. The graphite sheet resistance is tuned to limit charge spread on multiple strips while keeping good rate capabilities.

Thin Gap Chamber modules are assembled into doublets or triplets, made of 2 or 3 chambers, respectively. A multiplet configuration allows for redundancy, readout electrode staggering between chambers for an improved spatial resolution and fewer false coincidences due to hits from background radiation. The end-cap middle station has one triplet in front of the MDTs (TGC1) and two doublets behind (TGC2 and TGC3). The end-cap inner station (TGCI) has one doublet layer. The positioning of the TGC modules in the muon spectrometer is shown in Fig. 3.5.

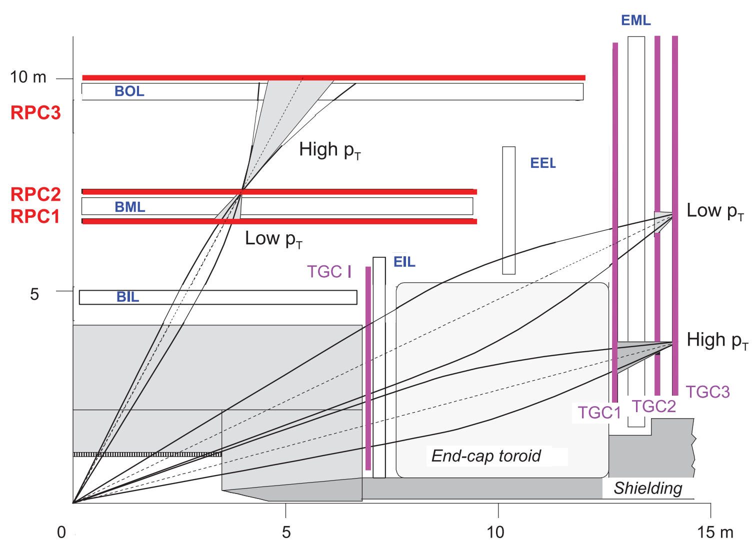

Figure 3.5: Schematic diagram of the TGC and RPC modules shown on a quadrant cross-section of the ATLAS muon spectrometer in the z-r plane.

3.3 The ATLAS muon detector upgrade

The increased luminosity of the LHC following the planned upgrade periods is a challenge for the LHC experiments such as ATLAS due to the increased particle flux experienced by the detector subsystems. To prepare ATLAS for these new running conditions with a minimum impact on the physics performance, parts of the muon end-cap inner stations will be replaced by an assembly of new detector modules called the New Small Wheels. The installation of the New Small Wheels is planned during the LHC Long Shutdown 2 period. The motivation for this muon upgrade and a description of the New Small Wheels are given below.

3.3.1 Motivation for the upgrade

A significant fraction of the muon Level-1 trigger rate originates from reconstructed track segments that are not associated with muons coming from the interaction point. Those "fake" muons are caused by background radiation incident on the muon end-cap middle station. The end-cap middle station background radiation consists mainly of neutrons and photons originating from the material located between the muon inner and middle stations. Offline analyses show that 98% of muon track candidates having $p_T > 20$ GeV/c reconstructed in the end-caps (in the region $|\eta| > 1.3$) that lead to a Level-1 trigger accept are fakes [93].

The Level-1 trigger rate for single muon event candidates is expected to increase linearly as a function of the LHC luminosity [94]. At an instantaneous luminosity of 3×10^{34} cm^{-2} s^{-1}, the Level-1 trigger rate for single muons with $p_T > 20$ GeV, the current minimum p_T threshold for single muons, is expected to reach approximately 60 kHz [93]. More than 80% of the total trigger bandwidth would be from end-cap muon candidates, most of which are fakes as mentioned earlier. This rate is excessive considering that the total Level-1 readout bandwidth is 100 kHz.

Possible workarounds to the Level-1 trigger rate problem include raising the trigger p_T threshold to 40 GeV or applying trigger prescaling[8]. These possible scenarios would successfully reduce the single muon trigger rate to an acceptable level, but with the consequence of reducing the sensitivity to many important physics processes that produce muons. For instance, the yield of Higgs boson decays via the $H \to WW^{(*)} \to l\nu l\nu$ channel would be reduced by about 70% [93]. The distributions of the leading and subleading lepton p_T in this Higgs decay channel are shown in Fig. 3.6 to demonstrate the impact of changing the trigger muon p_T threshold.

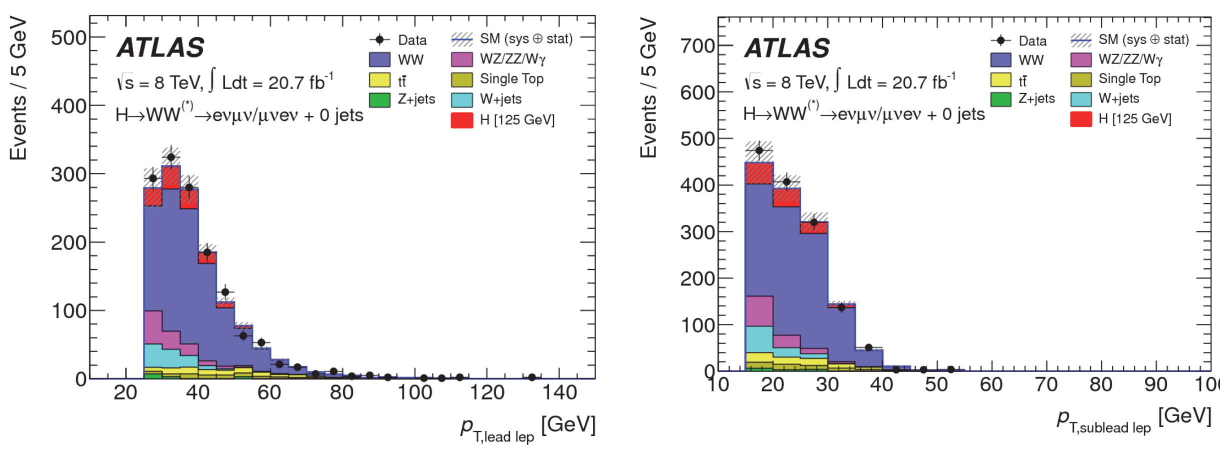

(a) **(b)**

Figure 3.6: Distribution of the (a) leading and (b) subleading lepton p_T for candidate events of the $H \to WW^{(*)} \to l\nu l\nu$ decay channel [93]. The red region highlights the simulated yield originating from Higgs boson decays. The efficiency for identifying this particular type of process is very sensitive to an increase in the p_T threshold.

Apart from issues with the muon trigger rate, the overall performance of muon detectors located in the inner end-cap stations will be compromised by an increase in particle flux. Based on simulation studies, the particle flux in that region is estimated to reach up to 20 kHz/cm^2 at an instantaneous luminosity of 7×10^{34} cm^{-2} s^{-1} [95]. Test-beam

8. Trigger prescaling consists in recording the information from only a preset fraction of events that satisfy a particular set of trigger conditions.

measurements showed that CSCs currently used in ATLAS would suffer from unacceptable inefficiencies at that level of particle flux [96]. The situation is similar for the MDTs installed in the forward region where, in addition to a loss in reconstruction efficiency, they will also suffer from a degradation of their intrinsic spatial resolution [61]. A large number of missed hits from the precision chambers would results in a degradation of the offline muon identification efficiency and muon p_T resolution.

3.3.2 New Small Wheel

To address the aforementioned issues, some parts of the current muon inner stations in the forward regions will be replaced by new detector structures called the New Small Wheels (NSW). The current muon Level-1 trigger algorithm in the end-cap regions only uses hits from the middle stations. The trigger algorithm will be enhanced by using NSW track segments to efficiently discriminate between fake and true muons. The reduction in the fraction of fake muons reconstructed by the enhanced trigger algorithm is expected to lower the Level-1 trigger rate to an acceptable level. A schematic diagram visually showing how the track segment measurements from the NSW will be used in the identification of muons by the Level-1 trigger system is shown in Fig. 3.7.

The NSW trigger algorithm requires detector modules that perform an online muon track segment reconstruction with an angular resolution better than 1 mrad to match the middle station pointing resolution. This requirement translates to a spatial resolution better than 100 μm per individual detector plane. Additionally, the muon track segment finding efficiency must be better than 97% to keep a good overall Level-1 trigger reconstruction efficiency. The offline spatial resolution must be similar to the one delivered by the current end-cap inner station precision modules. The NSW, like any other trigger detector system, is also required to perform bunch crossing identification which implies the use of detectors with a time jitter lower than 25 ns. Finally, detector modules making

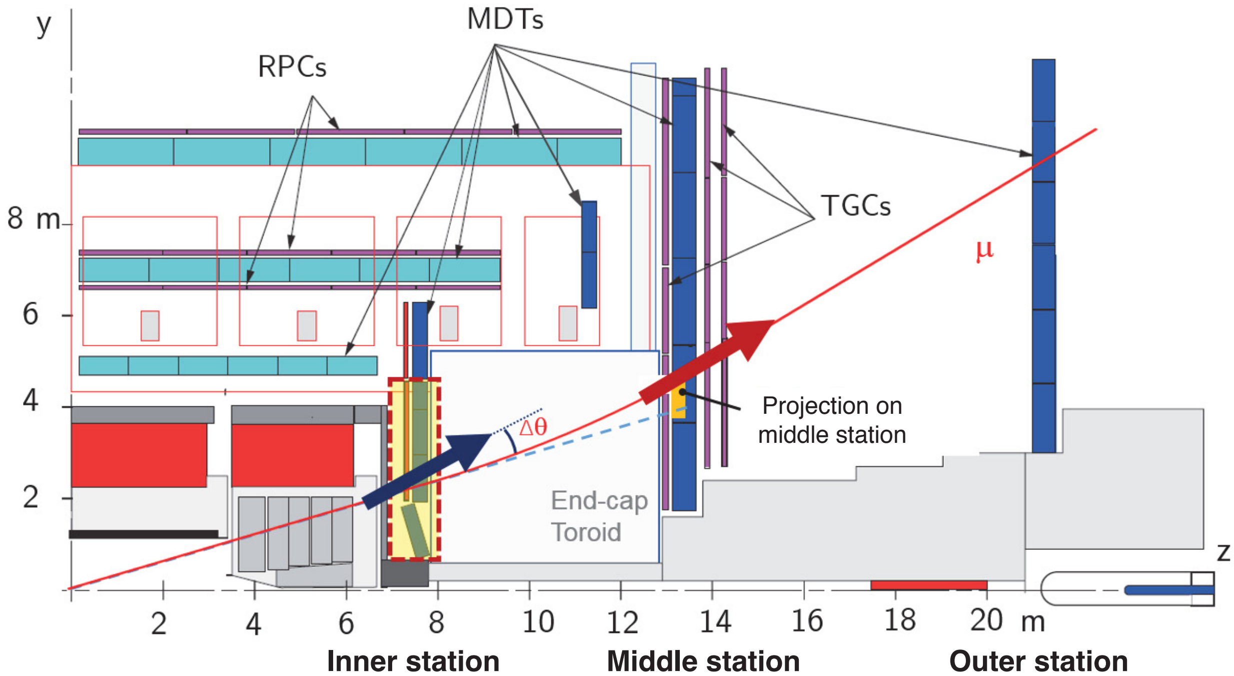

Figure 3.7: Projection of the current ATLAS muon spectrometer on the y-z plane [97]. The yellow shaded rectangle highlights the inner station modules that will be replaced by the NSW as part of the muon spectrometer upgrade. A visual representation of the Level-1 muon trigger algorithm, based on information from the NSW, is shown. A muon originating from the interaction point (red line) traverses the NSW resulting in the reconstruction of a track segment. The NSW measurement is used to confirm whether the reconstructed track segment comes from a particle originating from the interaction point by measuring the angle difference $\Delta\theta$ between the reconstructed track segment and a track segment that would be expected from a muon originating from the interaction point. Then, the NSW track segment is required to be consistent with a second track segment reconstructed by the middle station. Finally, if the NSW trigger conditions are met, the central trigger processor determines if a Level-1 trigger accept shall be issued based on the track segments. The muon transverse momentum p_T is estimated from the muon deviation in the magnetic field of the end-cap toroid which corresponds to angle difference of the track segments of the inner and middle stations.

up the NSW should deliver a stable overall performance up to the levels of particle fluxes expected until the LHC decommissioning.

The detector technologies that satisfy all aforementioned requirements and that were chosen for the NSW are small-strip Thin Gap Chambers (sTGC) [17, 21, 24] and Micromegas [98]. As shown in Fig. 3.8, the NSW combines eight layers of Micromegas mounted between four layers of sTGC on each side. The detectors are assembled into trapezoid-shaped modules of four layers called quadruplets. Quadruplets are then mounted into pie-slice "wedges" consisting of 3 quadruplets for sTGC or 2 for Micromegas. Two types of wedges with different dimensions make up the NSW: the large and the small. The sTGC quadruplets making up the wedges are named QS1, QS2 and QS3 for the small sector and QL1, QL2 and QL3 for the large sector in order of increasing distance r from the beam pipe. Small and large wedges have a similar r dimension but the large wedge covers a larger area in ϕ. Two sTGCs and two Micromegas wedges of the same type make a "sector" of the corresponding type. The wedges making a sector have the same dimensions but have different readout electrode granularity or cathode board segmentation. The naming "confirm" and "pivot" is used to label the wedges based on their z position relative to the ATLAS interaction point. A schematic of the large sector showing the individual quadruplets is shown in Fig. 3.8(a). The NSW comprises a total of 16 sectors arranged in a wheel and alternating between the small and large types. This configuration is used to match the middle station layout. All detector layers, structural supports and services must fit in the 1110 mm thick envelope left by the current inner station detectors. A schematic of the NSW is shown in Fig. 3.8(b).

Small-strip Thin Gap Chambers use the same operating principles as the current ATLAS TGCs but feature an improved spatial resolution and can be operated to even higher particle fluxes because they have a lower graphite coating sheet resistance. A thorough discussion of the sTGC technology is given in Section 3.3.3.

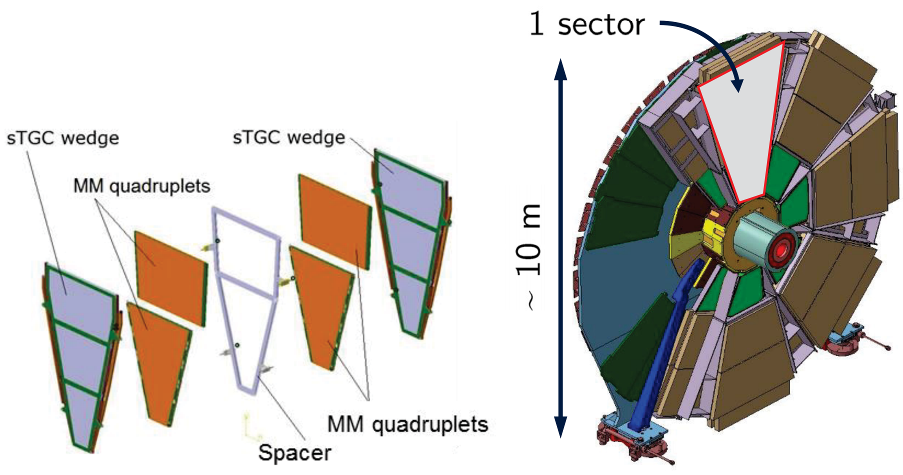

(a) (b)

Figure 3.8: (a) Schematic of a disassembled large sector combining sTGC and Micromegas wedges and (b) cutaway drawing of the finished NSW as seen looking towards the interaction point. The sTGC wedges combine 3 modules while Micromegas wedges have 2 modules. The detector modules are made of 4 detector layers. Wedges can be of "large" or "small" type making large and small sectors respectively. The NSW is made of 8 large and 8 small sectors.

Micromegas are micro-pattern gaseous detectors. The strip patterns of different Micromegas layers of a module are rotated by a small angle making a stereo-strip arrangement. Micromegas strips provide a precise measurement of the candidate muon track in the bending plane and a coarse measurement in the non-bending plane delivered by the stereo-strips.

Measurements from both sTGC and Micromegas are used for Level-1 trigger and for offline reconstruction. Both detectors technologies complement the weaknesses of the other. Micromegas do not suffer from a spatial resolution degradation with increasing angle of incidence, characteristic of multiwire ionization detectors such as sTGCs. On the other hand, the electron drift velocity in a sTGC is faster than for Micromegas due to the high electric field in the sTGC gas volume offering a faster signal formation. Therefore, in analogy with other detector systems of the ATLAS muon spectrometer, sTGC modules are called "trigger chambers" and Micromegas modules "precision chambers" despite having comparable tracking and trigger performances.

3.3.3 Small-strip Thin Gap Chambers

Small-strip Thin Gap Chambers are multiwire chambers operating in the quasi-saturated mode [17, 21, 24] with a gas amplification of approximately 10^5 [33], one order of magnitude larger than the ATLAS CSCs. The sTGC gas volume is relatively thin with an anode-cathode spacing of 1.4 mm. The spacing between the anode wires is 1.8 mm.

A schematic of a sTGC gas volume showing the different electrode types is shown in Fig. 3.9. Small-strip Thin Gap Chambers installed in the NSW have two segmented cathodes on each side of their gas volume. The first is segmented in fine strips 3.2 mm in width and the other into large pads. Anode wires are ganged in groups of 20 corresponding to a granularity of 3.6 cm. Confirm and pivot sTGC modules have the same strip pattern but different pad patterns. Strip electrodes are used for precision muon track reconstruction in the bending plane. Pad and wire electrodes provide a coarse measurement of the muon trajectory in the non-bending plane. Pad electrodes are also used to identify a band of strips to be read out after the passage of a candidate muon. The NSW trigger algorithm requires a 3-out-of-4 coincidence of the pad hits from different layers of a wedge to initiate strip readout [97]. The geometrical pattern of sTGC readout pads is staggered between the layers of a quadruplet. Logical pads are defined as regions of the η-ϕ space corresponding to overlapping areas of the sTGC physical readout pads in all four layers of a module. One logical pad covers approximately the width of 13 strips, or $\sim$40 mm, when projected on the surface of a detector plane. Physical readout pads have a trapezoidal shape in the Cartesian coordinate system. The physical pads size in the r-coordinate is approximately 80 mm. The readout pads size in the ϕ-coordinate is constant for a given module and is smaller for modules closer to the beam pipe to account for the increased particle flux [9]. Logical pads have the same shape as the physical pads but with approximately one-quarter of the area when projected onto the NSW detector planes. The drawing of the physical pad pattern on one of the sTGC cathode board and a schematic of the pad staggering are shown in Fig. 3.10.

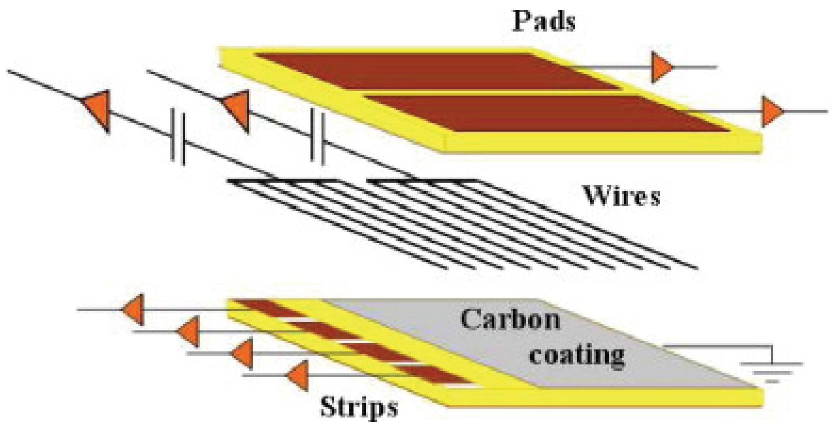

Figure 3.9: Schematic of the pad, strip and wire electrodes of a sTGC gas volume used in the NSW. The wires are ganged in groups of 20 and capacitively coupled to the readout electronics. The strip and pad electrodes are capacitively coupled to the graphite coating.

The thin gas volume geometry and high gain of sTGC detectors result in a very good performance for muon detection in a high particle flux environment. In this context, the advantages of a thin gas volume are:

- Quick evacuation of positive ions which reduces space charge effects that reduce the hit detection efficiency at high particle flux.
- Fast arrival of primary ionization electrons in the critical region resulting in a lower readout signal time jitter.
- Lower sensitivity to electronegative impurities capturing primary ionization electrons [100].
- Lower probability of δ-ray production that distort the charge induction on the

9. The size of readout pads is tuned to maintain approximately a uniform readout rate per channel over the surface area of the NSW.

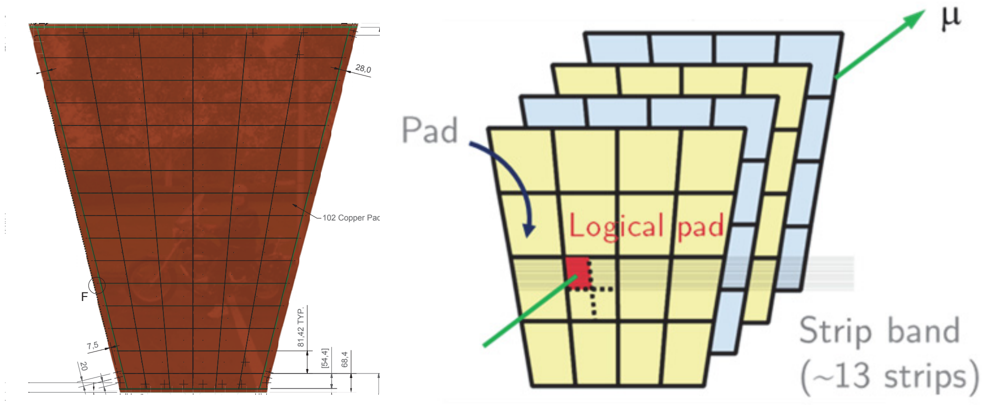

(a) **(b)**

Figure 3.10: (a) Physical readout pads geometry of layer 1 of the QL1 pivot quadruplet [99] and (b) schematic of the readout pads staggering between different sTGC layers of a quadruplet [97]. The area corresponding to a logical pad on a detector plane is approximately four times smaller than the area of a physical pad.

cathode.

- Lower sensitivity to gamma-rays [101] and neutron [102].
- Smaller dependence of the spatial resolution on the angle of incidence of the incoming particle due to a smaller charge spread along the plane perpendicular to the readout strips.
- More detector layers and redundancy in a given space allowance.

Additionally, the advantages of a multiwire chamber that operates at a high gain are numerous:

- Variations of the gas volume thickness have a smaller effect on the gas amplification and detector response [103].
- Small time jitter as ionization electrons close to the critical region suffice to generate a signal above threshold without waiting for ionization electrons generated far from the anode wire that have a long drift time [104].
- Smaller fluctuations in the gas amplification resulting in a smaller Landau tail [32].

In particular, it makes the detector response from neutrons similar to that of a minimum ionizing particle. Smaller fluctuations in charge production make it possible to use readout electronics that have a smaller dynamic range.

These characteristics come with the trade-off of a reduced accuracy of dE/dX measurements compared to other multiwire chambers operating in the true proportional mode. Furthermore, small variations of the gas volume thickness have a large impact on the detector response when using a thin gas volume despite the high gain operation that mitigates the effect. Therefore, the manufacturing process must meet very high-quality standards in order to keep the detector response variations over the area of a detector plane small.

The good spatial resolution, good timing properties, low sensitivity to background radiation (neutrons and photons) and good irradiation rate tolerance make sTGC detectors an excellent choice for a muon trigger chamber. The design characteristics of sTGC detectors are summarized below.

Wire pitch and anode-to-cathode spacing

The sTGC anode wire pitch (1.8 mm) and anode-to-cathode spacing (1.4 mm) are optimized to balance small time jitter and stable operations [14, 61]. A small distance between anode wires implies a shorter drift time for the ionization created in the space between two anode wires. A reduction of the wire pitch implies, however, a gain reduction because it increases the detector capacitance. A reduction of the anode-cathode spacing or an increase of the operating voltage can counterbalance the gain reduction. However, increasing the electric field in the drift region makes it more probable for an electron avalanche to reach the Raether limit and generate a spark.

Operating gas

The operating gas of sTGC detectors is a mixture of n-pentane and CO_2 in the ratio 45:55. Both gases have excellent quenching properties needed for operations at high gain and for a long efficiency plateau [105].

Carbon dioxide is a safe, stable and cheap gas. It exhibits a primary ionization yield similar to argon [10] while having a smaller probability of photon emission after photon absorption.

N-pentane is a hydrocarbon with excellent quenching properties. Compared to other hydrocarbons, n-pentane has a high molecular weight and a low ionization potential providing a large primary ionization yield and a high first Townsend coefficient. Furthermore, despite being liquid when pure at room temperature, n-pentane has a high vapour pressure and can be mixed in high concentrations with other gases.

N-pentane has a lower ionization potential than CO_2 [11] which implies that the ionization yield is enhanced by the Penning effect. The other consequence is that CO_2 ions transfer their positive charge to n-pentane molecules before they reach the cathode thereby reducing the probability of afterpulses after ions recombine at the cathode. The gas mixture also exhibits good ageing properties [62].

Wire radius

The anode wires of sTGC detectors have a diameter of 50 µm and are made of gold-plated tungsten. The choice of wire diameter is a balance between a good mechanical strength and a high gas amplification. Thin anode wires also provide a high gain response independent of the integration time as shown in Eq. 2.26. Tungsten has good ductility and shows an excellent resistance to mechanical stress. Gold has a good electrical conductivity

10. $n_T^{\mathrm{CO_2}} = 91\ \mathrm{cm}^{-1}$ and $n_T^{\mathrm{Ar}} = 94\ \mathrm{cm}^{-1}$ [32].
11. $U_{i,\text{n-pentane}} = 10.34$ eV and $U_{i,\mathrm{CO_2}} = 13.78$ eV [106].

in addition to a high chemical stability which slows detector ageing.

Segmented resistive cathode

Cathode boards are made of 1.3 mm thick FR-4, a glass-reinforced epoxy laminate. Each board is covered on both sides by a 15 µm copper layer. The copper layer outside of the gas volume is used for grounding. The copper layer facing the gas volume forms the readout electrodes that are engraved to the desired shape.

The cathode resistive coating is made of graphite and the capacitive layer is a mylar sheet. The cathode transparency and sheet resistance can be tuned depending on the required granularity and particle flux performances. The sTGC detectors for the NSW have a graphite coating sheet resistance varying between 150 and 200 k$\Omega/\Box$, lower than for a TGC. The thickness of the mylar sheet varies between 150 and 200 µm.

For precision track reconstruction, the strip readout electrodes are used. The optimum strip width for moderately angled tracks was found to be 3.2 mm [107]. The charge induction spreads over typically three to five strips forming a "charge cluster". The track position is deduced from the centroid position of the strip-cluster. The sTGC detectors can achieve a spatial resolution better than 50 µm for perpendicular tracks [67]. The sTGC detectors have no built-in mechanism to correct for differential non-linearity effects. The differential non-linearity bias must be corrected at the level of signal processing by the readout electronics or during offline analysis.

4

Study of the impact of construction non-conformities

The detector modules making the New Small Wheel (NSW) must perform an online reconstruction of candidate muon track segments with an angular resolution better than 1 mrad. Both small-strip Thin Gap Chambers (sTGC) and Micromegas modules should independently satisfy this requirement for an increased redundancy of the trigger system. The angular resolution depends on intrinsic detector effects and the mechanical precision of sTGC modules construction. The impact of the latter is potentially reduced with a tighter quality control of the manufacturing process; for instance, achievable with more stringent construction tolerances.

The impact of detector non-conformities on the track reconstruction performance must be quantified to confirm that the detector manufacturing and quality control procedures are adequate in order to deliver detector modules that satisfy the NSW specifications. This chapter presents a Monte Carlo simulation of a set of sTGC detector planes arranged following the NSW layout. The simulation aims at characterizing the track reconstruction performance of the detector planes as a function of different types and sizes of construction non-conformities.

Section 4.1 of this chapter presents a definition of the different mechanical non-conformities considered in this study. Section 4.2 contains a description of the layout of sTGC modules used in the simulation for one sector of the NSW. Section 4.3 describes the simulated track generation and simulation of the detector and construction effects. Sections 4.4 and 4.5 respectively describe the binning and sampling procedures of the simulation. Finally, results from the simulation are presented in Section 4.7 with a study of the results sensitivity to the simulation parameters presented in Section 4.8.

4.1 Definition of construction non-conformities

As described in Section 3.3, sTGC modules are quadruplets made up of four detector layers. Each layer has two cathode boards, one strip-board and one pad-board, that have different readout electrode patterns. The engraving of the electrode pattern on the boards is performed using a Computer Numerical Control (CNC) machine. The cathode boards quality control procedure [108] define four non-conformities of the strip pattern that have a direct impact on the final track reconstruction performance of the NSW. The non-conformities are defined using the brass inserts, two metal pieces fitted on the angled side of the cathode boards, as a position reference. Drawings of brass inserts are shown in Fig. 4.4. A sketch demonstrating the impact of each strip-board non-conformity on the shape of the strip pattern is shown in Fig. 4.1. The strip-board non-conformities are:

- **constant offset** by which the strip pattern is moved along the precision coordinate perpendicular to the strips,
- **pitch scale** by which the strip width changes gradually along the precision coordinate,
- **non-parallelism** by which the strip width changes gradually along the strip length and
- **rotation** by which the strip pattern is rotated.

A strip-board qualifies for module manufacturing only if the value of all non-conformities fall within plus or minus the corresponding construction tolerance. The value of construction tolerances applied to each individual strip-board is given in Table 4.1. The present study is not concerned with non-conformities of the pad-boards because pads are not used for the reconstruction of the muon trajectory.

Additional non-conformities arise from undesired shifts introduced during quadru-

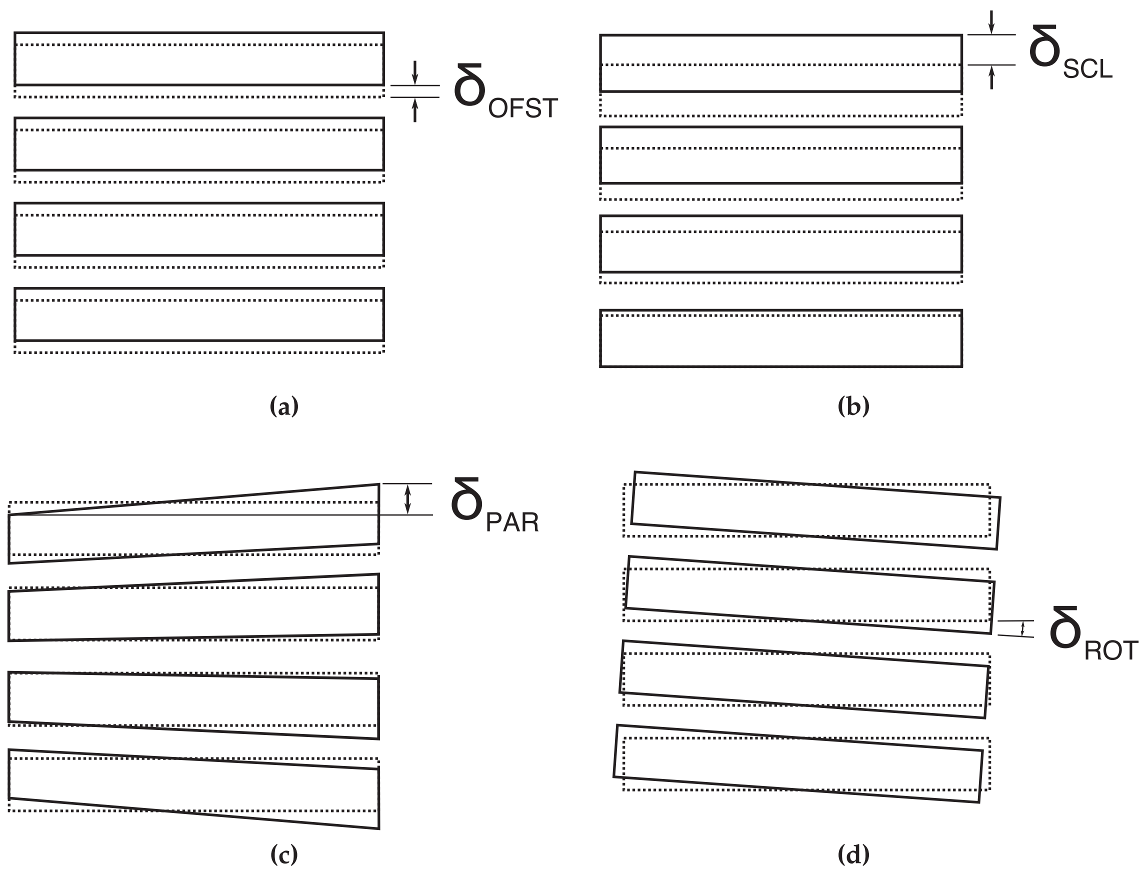

Figure 4.1: Sketch of the strip-board non-conformities considered compared to the nominal strip pattern (dotted lines): (a) constant offset, (b) pitch scale, (c) non-parallelism and (d) rotation. The measurement performed during strip-board dimensional control is shown on each diagram. The values of δ_{OFST}, δ_{SCL} and δ_{PAR} are in units of length while the value of δ_{ROT} is an angle. The strip dimensions are not to scale.

plet assembly and variations in the thickness of detector components. The assembly-level non-conformities considered here are:

- relative strip-boards alignment during **multiplet gluing** where one sTGC detector is moved with respect to the other during the gluing procedure and,
- **shift in z** where the anode wire plane is shifted with respect to its nominal value.

The position of the wire plane is relevant because it corresponds to the z-coordinate of a muon space point measured by a sTGC. Contrary to strip-board non-conformities, effects of multiplet gluing and z shifts cannot be directly measured during construction. However, the range of these non-conformities can be translated to an equivalent construction tolerance estimated from the construction tolerances of detector components and from the specifications of the alignment tools used for manufacturing. Approximate values for the equivalent construction tolerances at the assembly level are given in Table 4.1.

The sTGC quadruplets are ultimately assembled in a wedge of three quadruplets. Then, wedges are assembled into detector wheels. The simulation study presented in this chapter is not concerned with the potential misalignment that results from the manufacturing or alignment steps in the wedge and wheel assembly. The study assumes that the position of sTGC quadruplets with respect to each other will be precisely known based on the optical alignment systems to be installed.

Non-conformity	Tolerance
Constant offset	± 75 µm
Pitch scale	± 75 µm
Non-parallelism	± 75 µm
Rotation	$\pm 0.004°$
Multiplet gluing	± 50 µm
Shift in z	± 50 µm

Table 4.1: Construction tolerances on non-conformities for each individual strip-board and subsequent quadruplet assembly steps.

4.2 Simulated detector geometry

Due to azimuthal symmetry, the simulation is limited to the track reconstruction performance of a single sTGC sector, an assembly of 6 sTGC modules positioned at constant angle ϕ. A sector can be considered as the most basic detector unit of the NSW because no straight muon track originating from the ATLAS interaction point can possibly traverse more than one sector if neglecting overlapping areas. A detailed description of the NSW layout was given in Section 3.3.2. The track reconstruction performance of both “small” and “large” sectors is simulated independently.

A schematic diagram of the detectors layout geometry used in the simulation is shown in Fig. 4.2. The schematic defines the Cartesian coordinate system used in the simulation. The origin of the coordinate system coincides with the ATLAS interaction point. The sTGC gas volumes are modelled as trapezoidal-like polygonal surfaces having no thickness. A simulated sector is made of two identical sTGC wedges located at different z positions, each made of three sTGC quadruplets of different areas and arranged along the y-coordinate. The schematics of the small and large sTGC wedges displaying the dimensions of the sTGC quadruplets and their y position with respect to the beam pipe are shown in Fig. 4.3. The gas volumes of a quadruplet are named L1 to L4, in order of increasing distance from the ATLAS interaction point.

In the simulation, the detector planes have the dimensions of the strip-boards of the gas volume they model. The dimensions are the same for all layers of a given quadruplet. The z position of the detector planes corresponds to the z position of the gas volumes anode wire planes, which defines the z position of a muon “hit” in a sTGC gas volume. The values of z used in the simulation are shown in Table 4.2. The dimensions and positioning of the detector planes are taken from the sTGC modules technical drawings [99].

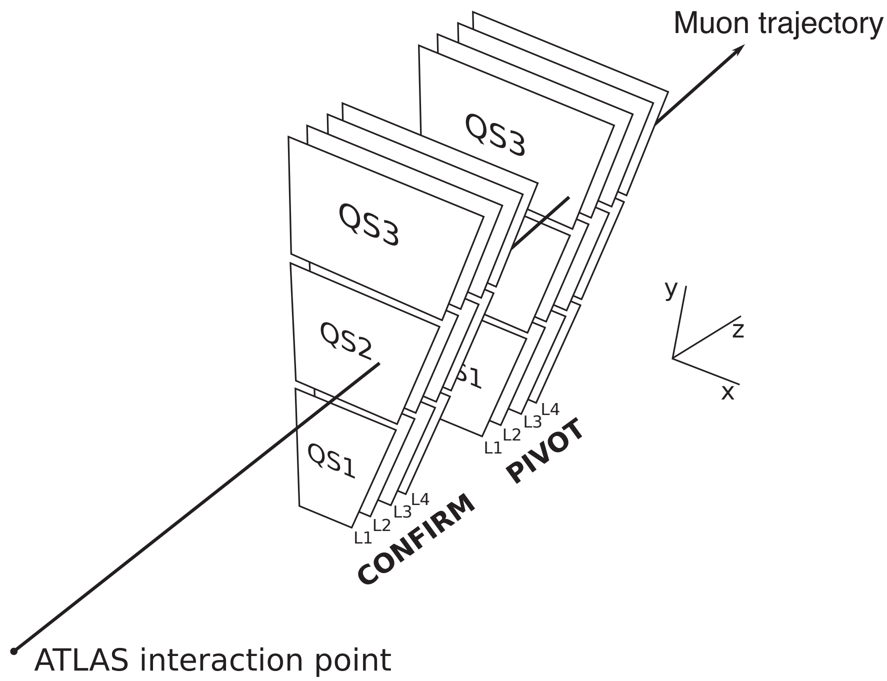

Figure 4.2: Schematic diagram of the simulated detector layout for the small sector. The confirm wedge of the small sector is positioned closer to the ATLAS interaction point than the pivot wedge while the inverse is true for large sectors. A simulated muon trajectory is shown. This schematic is not to scale.

Layer	Large	Small
L1 pivot	7457.55	7327.55
L2 pivot	7468.52	7338.52
L3 pivot	7479.49	7349.49
L4 pivot	7490.46	7360.46
L1 confirm	7791.55	6993.55
L2 confirm	7802.52	7338.52
L3 confirm	7813.49	7349.49
L4 confirm	7824.46	7360.46

Table 4.2: The z position of the simulated detector planes. Units are millimetres.

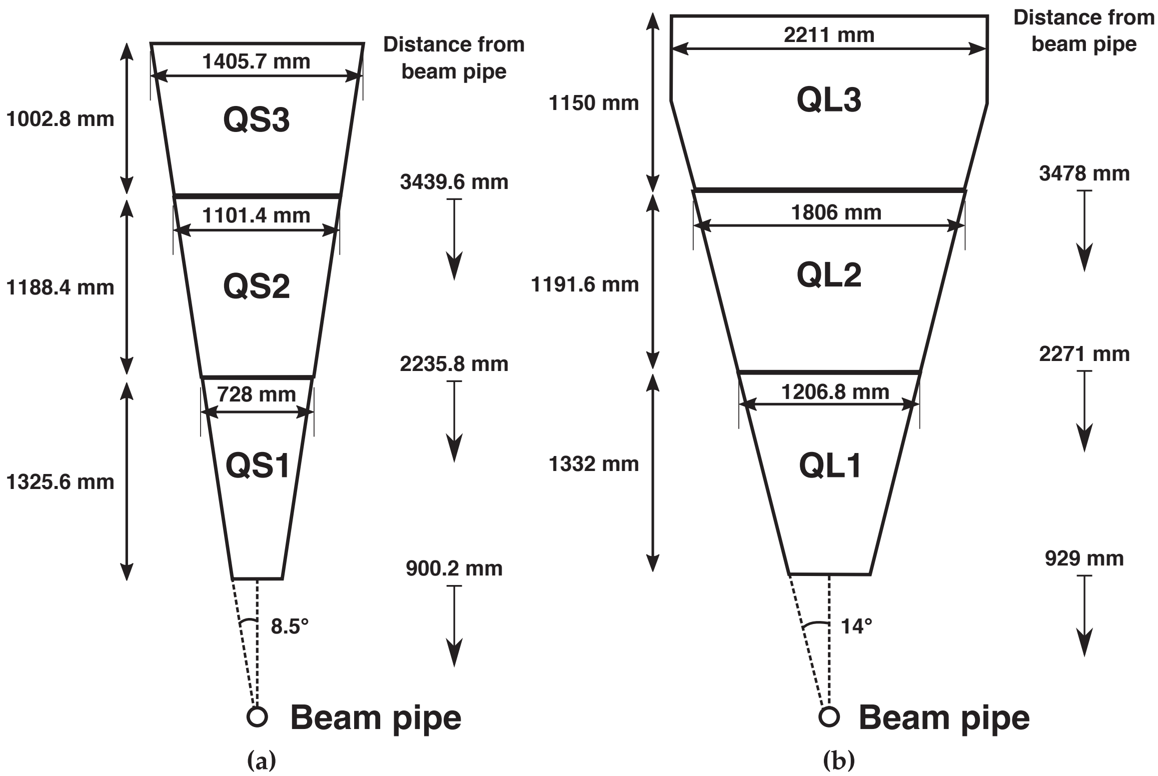

Figure 4.3: Dimensions of the (a) small and (b) large sTGC wedges projected in the x-y plane. The schematics are to scale. The height, width and distance from the beam pipe of each sTGC quadruplet are displayed. The wedges angular coverage in ϕ is also shown. There are small gaps between the quadruplets of the order of 1 cm that cannot be resolved on the figure.

4.3 Simulation of mechanical non-conformities and track reconstruction

Simulated muons originate from the interaction point and are generated at a random angle in the ATLAS $\phi - \eta$ space. Although in ATLAS the trajectory of charged particles originating from the interaction point is bent in the inner detector region because of the magnetic field produced by the solenoid magnet, the muon trajectory in the region between the solenoid and toroid magnets in the end-cap is relatively straight. Therefore, the simulated muon trajectory through the NSW is assumed to be straight.

Simulated muons are selected for analysis if they cross at least three out of four sTGC detector planes of each wedge in accordance to the trigger algorithm [97]. Hit points indexed i are defined for each detector plane crossed by the selected muon. The "true" position of the muon space points, $\vec{r}_{\text{true},i}$, is at the intersection of the muon trajectory and the detector planes. The space points are processed, as described in section 4.3.1 and 4.3.2, to obtain the space points $\vec{r}_{\text{reco},i}$ of the reconstructed track. The difference between the true and reconstructed space points is defined as

$$\delta\vec{r}_i \equiv \vec{r}_{\text{reco},i} - \vec{r}_{\text{true},i} = \delta x_i \hat{\mathbf{x}} + \delta y_i \hat{\mathbf{y}} + \delta z_i \hat{\mathbf{z}} \tag{4.1}$$

where δx_i, δy_i and δz_i are the projections of the vector $\delta\vec{r}_i$ on the unit vectors of the simulation coordinate system and depend on the combined effects of construction non-conformities and sTGC detector intrinsic effects such as the single hit spatial resolution and efficiency.

The track x-coordinate is not used by the NSW muon trigger algorithm. Therefore, both the true and reconstructed tracks are projected onto the $x = 0$ plane. A linear fit is performed on both the true and reconstructed hit points in order to obtain the true and the reconstructed muon track, respectively. The angle between the beam pipe and the projected tracks is θ_{true} (θ_{reco}) for the true (reconstructed) track. The angle difference between the two projected tracks is defined as

$$\Delta\theta \equiv \theta_{\text{reco}} - \theta_{\text{true}} \tag{4.2}$$

4.3.1 Detector construction effects

The effects of construction non-conformities, defined in Section 4.1, on the true track hits, are applied following the sequence:

$$\text{rotation} \rightarrow \text{offset} \rightarrow \text{scale} \rightarrow \text{parallelism} \rightarrow \text{z position} \rightarrow \text{gluing}$$

The order of the sequence for strip-board non-conformities has a negligible impact on the resulting value of $\Delta\theta$. For example, the relative variation of δy_i due to the swap of the order of any of the two construction non-conformities of the sequence is of the order of the ratio between the values of the non-conformities involved and the strip-board dimensions. The order of the z position non-conformity is also arbitrary because all other space point transformations do not depend on the z value. Space point displacements due to non-conformity in the gluing of multiplet modules are applied last to follow the sTGC manufacturing steps.

The construction non-conformities of individual detector planes are parameterized by the values δ_{ROT} (rotation), δ_{OFST} (offset), δ_{SCL} (scale), δ_{PAR} (non-parallelism) and δ_{Z} (z position) whose range of values are limited by a predefined set of construction tolerances. The 24 detector planes of a simulated sector have independent randomly generated values for each parameter. Construction non-conformities due to the gluing of two gas volumes into doublets and of two doublets into a quadruplet are parameterized by the parameter δ_{GLU}. The 12 doublets and 6 quadruplets of a simulated sector have independent randomly generated values of δ_{GLU}. All values of non-conformity parameters are randomly generated from a uniform probability density function (p.d.f.) that is bounded with plus or minus the corresponding tolerance value for the non-conformity. A uniform p.d.f. accounts for all possible biases in detector manufacturing while being agnostic on the true distribution of construction non-conformities which is not well known at this stage of the project. A bounded p.d.f. is consistent with the sTGC quality control procedure which rejects sTGC parts having dimensional control measurements outside of the tolerances.

Strip-boards electrode pattern

Table 4.3 shows the updated values of x and y, corresponding to $x + \delta x$ and $y + \delta y$ respectively, after each strip-board non-conformity is applied. The strip-board geometric parameters are the small trapezoid width W_s and height H. The geometric center of the strip-board is at coordinates $(\bar{x}, \bar{y})$. The axis of rotation of the strip pattern is chosen to be at coordinates (ω_x, ω_y). In the simulation, the axis of rotation coincides with the geometric center of the detector planes implying that $\omega_x = \bar{x}$ and $\omega_y = \bar{y}$. This choice is consistent with the quality control procedure of strip-boards which measures the strip pattern rotation assuming that the axis of rotation is at the geometric center. The values of δx and δy both vary as a function of the space point coordinates (x, y) of the previous step in the sequence of non-conformities simulation.

Anode wire planes z position

The z displacement of the anode wire planes is assumed constant over the area of the gas volumes. The difference between the nominal and displaced position of the wire planes is δ_{Z}, equal to the shift δz applied to the space points which implies that

Non-conformity	$x + \delta x$	$y + \delta y$
Rotation	$(x - \omega_x)\cos(\pi\delta_{\text{ROT}}/180)$ $+(y - \omega_y)\sin(\pi\delta_{\text{ROT}}/180) + \omega_x$	$-(x - \omega_x)\sin(\pi\delta_{\text{ROT}}/180)$ $+(y - \omega_y)\cos(\pi\delta_{\text{ROT}}/180) + \omega_y$
Offset	0	$y + \delta_{\text{OFST}}$
Scale	0	$\frac{\delta_{\text{SCL}}+H}{H}(y - \bar{y}) + \bar{y}$
Parallelism	0	$\frac{\delta_{\text{PAR}}}{4}\frac{(x-\bar{x})}{W_s/2}\frac{(y-\bar{y})}{H/2} + y$

Table 4.3: Value of the x and y coordinates of space points following a simulated strip-board non-conformity. The displacements are applied sequentially meaning the values of x and y are those of the space points coordinates after the previous transformation. The deviation δz is always 0 for strip-board non-conformities.

$$\delta z = \delta_{\text{Z}} \tag{4.3}$$

Doublets and quadruplets gluing

The sTGC gas volumes are glued in two steps before they make a quadruplet. First, pairs of gas volumes are glued together to form “doublets”. Then, two doublets are glued to form a “quadruplet”. The gluing procedure involves placing the detectors on a granite table with a 5 mm paper honeycomb in between for spacing. The alignment of the strip-boards is done using two alignment pins emerging from the granite table. Each strip-board has two brass inserts on one of the angled edge of the trapezoid. During gluing, the brass inserts of the strip-boards are pushed against the alignment pins. A drawing of the two types of brass inserts is shown in Fig. 4.4.

As shown in Fig. 4.5, the alignment pins may be angled compared to the nominal vertical position during gluing. The maximum displacement of the tip of the alignment pins is approximately $\delta_{\text{pin}} = 50$ µm either towards or away from the strip-board. The effect gives rise to a rotation of the top element with respect to the bottom one with an angle of rotation that is a function of the pins tilting.

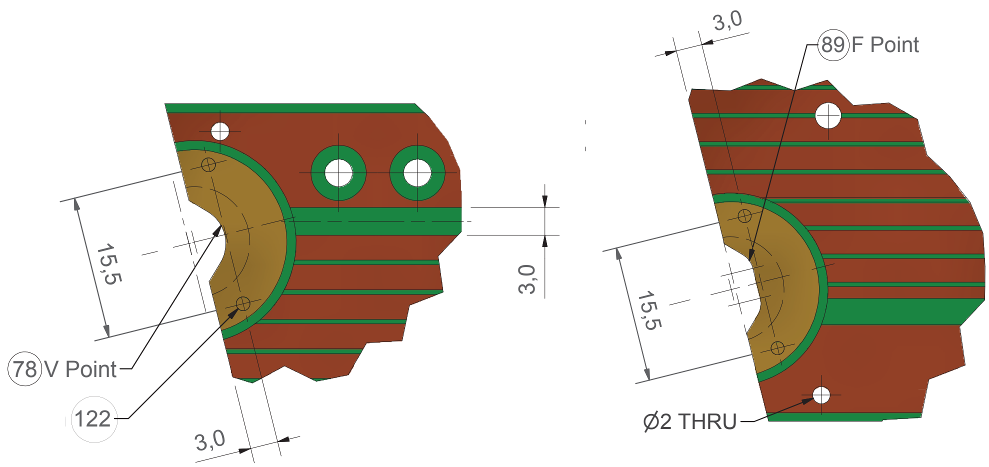

(a) (b)

Figure 4.4: Drawing of the strip-board brass inserts as seen in the QL1 quadruplet technical drawings [99]. Units are millimetres. The brass inserts can be either of (a) triangular or (b) trapezoidal type. One brass insert of each type is crimped on one of the angled sides of the strip-boards. The triangular brass insert is located on the long-base side and the trapezoid brass insert on the short-base side.

To account for gluing effects in the simulation, each doublet and quadruplet of a simulated sector is given two random independent values, $\delta^{\mathrm{A}}_{\mathrm{GLU}}$ and $\delta^{\mathrm{B}}_{\mathrm{GLU}}$, corresponding to the displacements of the tips of both alignment pins. The horizontal displacement of the brass inserts, Δs_{A} and Δs_{B}, is

$$\Delta s_{\mathrm{A}} = \delta^{\mathrm{A}}_{\mathrm{GLU}} \frac{d}{h_{\mathrm{pin}}} \qquad \Delta s_{\mathrm{B}} = \delta^{\mathrm{B}}_{\mathrm{GLU}} \frac{d}{h_{\mathrm{pin}}}. \tag{4.4}$$

For doublets gluing, d is the vertical distance between the strip-boards of the two gas volumes. For quadruplets gluing, d is the vertical distance between the L2 and L3 strip-boards. The length of the alignment pin outside the granite table is denoted by h_{pin}. In the simulation, $d = 6.3$ mm is used for doublet gluing and $d = 14.7$ mm for quadruplet gluing. The value $h_{\mathrm{pin}} = 50$ mm is used in all cases.

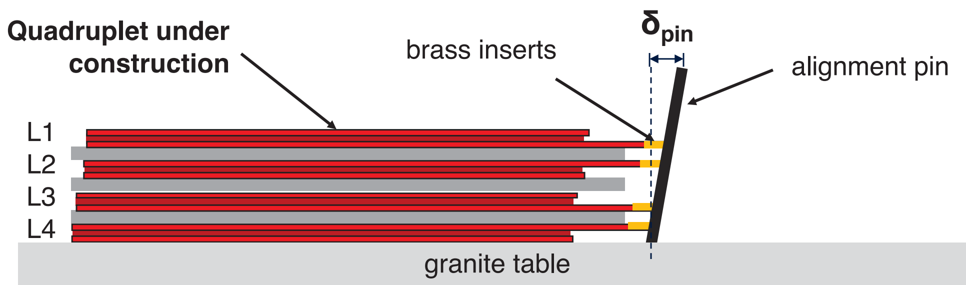

Figure 4.5: Gluing of doublets into a quadruplet on a granite table. The brass inserts are moved away from their nominal positions because of tilted alignment pins.

The displacement of the brass inserts results in a rotation in the x-y plane of the top element with respect to the bottom element. The angle of rotation θ_{GLU} and the position of the axis of rotation $\vec{\omega}_{\mathrm{GLU}}$ are

$$\theta_{\mathrm{GLU}} = \operatorname{atan}\left[\frac{\Delta s_{\mathrm{A}} + \Delta s_{\mathrm{B}}}{\left|\vec{r}^{\,\mathrm{A}}_{\mathrm{b.i.}} - \vec{r}^{\,\mathrm{B}}_{\mathrm{b.i.}}\right|}\right] \qquad \vec{\omega}_{\mathrm{GLU}} = \left(\vec{r}^{\,\mathrm{A}}_{\mathrm{b.i.}} - \vec{r}^{\,\mathrm{B}}_{\mathrm{b.i.}}\right)\frac{\Delta s_{\mathrm{B}}}{\Delta s_{\mathrm{A}} + \Delta s_{\mathrm{B}}} + \vec{r}^{\,\mathrm{B}}_{\mathrm{b.i.}} \tag{4.5}$$

where $\vec{r}^{\,\mathrm{A}}_{\mathrm{b.i.}}$ and $\vec{r}^{\,\mathrm{B}}_{\mathrm{b.i.}}$ are vectors pointing to the A and B brass inserts respectively. All vectors are projected in the x-y plane.

The contribution of the gluing procedure to the values of δx and δy is obtained using the formula for rotation of Table 4.3 using as inputs the angle of rotation θ_{GLU} and the position of the axis of rotation $\vec{\omega}_{\mathrm{GLU}}$. For doublet gluing, the bottom detector plane (L2 or L4) is assumed unchanged while the top detector plane (L1 or L3) is rotated. For quadruplets gluing, the bottom doublet (L3 and L4) is assumed unchanged while the top doublet (L1 and L2) is rotated. The gluing procedure is assumed to have no impact on the z coordinate of the space points. The gluing transformations are applied to the space points in the sequence

$$\text{doublet gluing} \rightarrow \text{quadruplet gluing}$$

which is consistent with the manufacturing procedure.

4.3.2 Detector intrinsic effects

By definition, detector intrinsic effects impact the position of the reconstructed track space points independently of mechanical non-conformities. The intrinsic effects considered here are the sTGC intrinsic spatial resolution and hit efficiency. It is possible to obtain an analytic expression for the angular resolution $\sigma_{\Delta\theta}$ as a function of these two effects assuming a perfect detector construction as shown in Appendix A.

Intrinsic spatial resolution

The sTGC intrinsic spatial resolution smears the precision coordinate y of the space points. The simulated displacement δy, due to the sTGC intrinsic spatial resolution, is taken from the Gaussian p.d.f.

$$G(\delta y) = \frac{1}{\sigma_{\text{sTGC}}\sqrt{2\pi}} \exp\left[-\frac{\delta y^2}{2\sigma_{\text{sTGC}}^2}\right] \tag{4.6}$$

where σ_{sTGC} is the intrinsic spatial resolution which is a direct consequence of the chosen sTGC detector geometry and mode of operation. It is assumed to be constant for all detector planes and track angles. One independent value of δy is randomly generated for each space point of a simulated track.

The detector intrinsic spatial resolution combines the contributions of the primary ionization from the incident charged particle, the gas amplification, strips charge sampling and the readout electronics response. The simulation uses $\sigma_{\text{sTGC}} = 250$ µm, an estimate based on the expected sTGC spatial resolution during the online operation of ATLAS [1].

Hit efficiency

The minimum hit efficiency required by the quality control procedure of sTGC quadruplet construction is $\varepsilon > 98\%$ over the sensitive areas of the detector planes [2]. Inefficiencies increase the probability of selecting a track with six or seven space point measurements rather than eight in the ideal case (six being the minimum required by the trigger algorithm). Tracks with missing space points have a worse angular resolution than ideal tracks reconstructed based on the information from eight space points.

Hit efficiency effects are accounted for in the simulation by discarding individual space points of a track with a probability $1 - \varepsilon$. Muon tracks reconstructed based on less than three space point measurements per wedge are discarded and not processed further. The simulation neglects the presence of non-sensitive regions of the gas volumes due to internal support structures which amount to less than 5% of the total surface area of a strip-board.

1. Test-beam measurements with tracks perpendicular to the sTGC gas volume reported a spatial resolution better than 50 µm [67]. However, the ATLAS sTGC trigger processor computes the charge cluster centroid position using a weighted average algorithm without correcting for differential non-linearity effects. Differential non-linearity effects with an amplitude of approximately 400 µm, larger than for test-beam measurements, are expected. Moreover, the spatial resolution worsens with the track angle as shown in Chapter 5. Muon incident at an angle varying between 7° and 32° are expected on the sTGC detector planes. An average spatial resolution of 250 µm is a reasonable estimate when combining all these effects.

2. Excludes inefficient regions due to support structures in the gas volume.

4.4 Logical pads

The angular coverage of the simulated sectors is divided in regions corresponding roughly to the angular coverage of the sTGC logical pads described in Section 3.3. The simulated logical pads pattern is simpler than the pattern that will be constructed in the NSW. In the simulation, the η-ϕ space is divided in areas of equal size in ϕ but having dimensions in η consistent with half the r dimension of a physical readout pad.

In the simulation, a distribution of the angular deviation $\Delta\theta$ is obtained for each logical pad. A simulated muon is assigned to the $\Delta\theta$ distribution that corresponds to the logical pad traversed by the muon's true trajectory.

4.5 Random generation of sectors

For a given set of construction tolerances, the simulation generates a large number of sectors with random and independent construction non-conformities [3]. For each simulated sector, an average of 400 true muons are incident on each logical pad. The logical pads that do not receive a number of tracks above a predefined threshold are discarded. The mean $\mu_{\Delta\theta}$ and standard deviation $\sigma_{\Delta\theta}$ of the $\Delta\theta$ distributions are obtained for each logical pad.

4.6 Track reconstruction performance metric

The angular resolution of the sTGC sector is defined as the root mean square (RMS) of the angle difference between the true and the reconstructed muon tracks. Using this definition, the angular resolution is the square root of the 2$^{\text{nd}}$ order non-central moment

3. A few thousand sectors were simulated for both the small and large sector simulations. At this level of statistics, small variations (within 10%) of the simulation parameters have a larger effect on the final result than statistical variations.

of the $\Delta\theta$ distribution denoted $R_{\Delta\theta}$. Assuming that the $\Delta\theta$ distribution is similar to a Gaussian function, the value of $R^2_{\Delta\theta}$ is

$$R^2_{\Delta\theta} \equiv \sigma^2_{\Delta\theta} + \mu^2_{\Delta\theta} \tag{4.7}$$

The distribution of $R_{\Delta\theta}$ values for a logical pad is obtained after simulating multiple sectors. In principle, the $R_{\Delta\theta}$ distribution is bounded by the construction tolerances. However, the distribution has a very long tail with a small fraction of the simulated sectors falling far from the distribution core. A sensible metric to evaluate the worse possible sector performance without accounting for the unlikely sectors falling in the tail is the value $R^f_{\Delta\theta}$ defined by

$$f = \int_0^{R^f_{\Delta\theta}} g\left(R_{\Delta\theta}\right) dR_{\Delta\theta} \tag{4.8}$$

where g is the simulated distribution of $R_{\Delta\theta}$ normalized to unit area. The symbol f can be interpreted as representing the probability of manufacturing sectors having an angular resolution smaller than $R^f_{\Delta\theta}$. Provided that the value of f is sufficiently high, the value of $R^f_{\Delta\theta}$ provides a realistic estimate of the worse possible track reconstruction performance given a set of construction tolerances. The values of $\mu^f_{\Delta\theta}$ and $\sigma^f_{\Delta\theta}$ are also obtained from the integrals of the $\mu_{\Delta\theta}$ and $\sigma_{\Delta\theta}$ distributions for each logical pad. The value $f = 99\%$ is used for this simulation as it was observed that the values of $R^{0.99}_{\Delta\theta}$ are always close to the core of the simulated $R_{\Delta\theta}$ distributions. An example of the $R_{\Delta\theta}$ distribution for one logical pad and a plot of the integral of the distribution, which is used to extract the value $R^f_{\Delta\theta}$, are shown in Fig. 4.6.

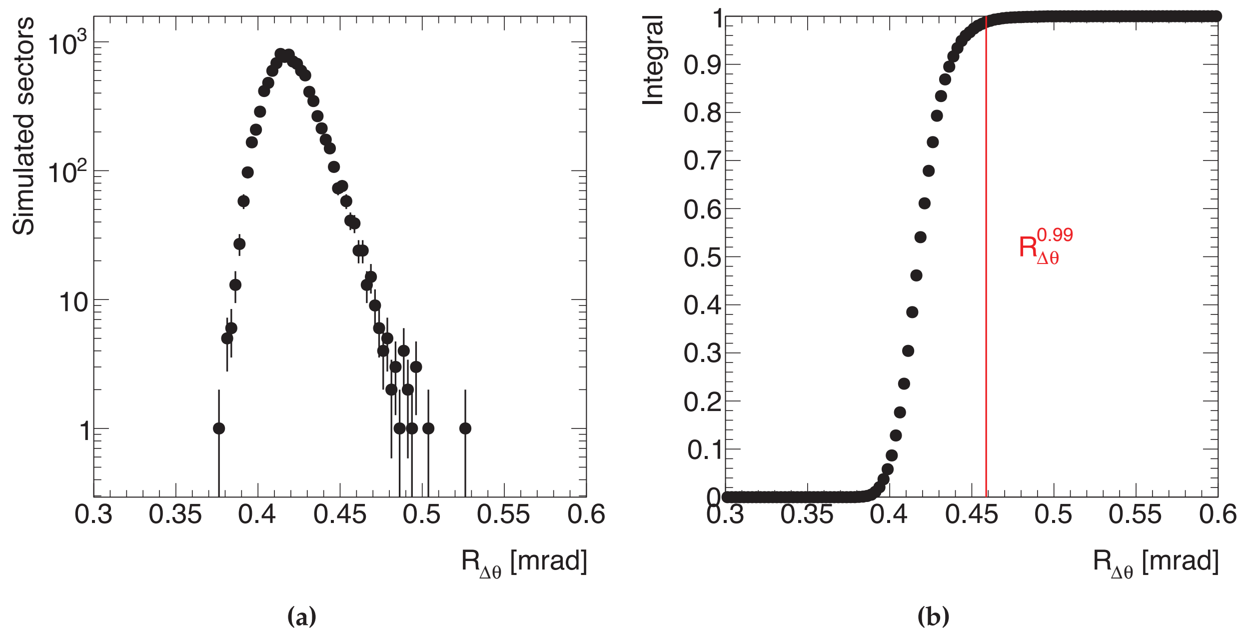

Figure 4.6: (a) Distribution of $R_{\Delta\theta}$ values for one logical pad after simulating 10^4 small sectors and (b) the same distribution, but integrated and normalized with the value at which the integral is above 99%, $R^{0.99}_{\Delta\theta}$, highlighted.

4.7 Results

Construction tolerances shown in Table 4.1 are used to simulate a very large number of possible sectors. The values of $\mu^{0.99}_{\Delta\theta}$, $\sigma^{0.99}_{\Delta\theta}$ and $R^{0.99}_{\Delta\theta}$ as a function of the logical pad for the small and large sectors are shown in Fig. 4.7. The angular resolution degrades with η because of the non linear transformation of the track slope into an angle θ.

The values of $\sigma^{0.99}_{\Delta\theta}$ are larger than $\mu^{0.99}_{\Delta\theta}$ and, therefore, define the shape of the $R^{0.99}_{\Delta\theta}$ distribution. The distribution of $\mu^{0.99}_{\Delta\theta}$ value is not symmetric with respect to $\phi = 0$ due to the gluing procedure, which rotates the detector planes with an axis of rotation that is systematically on the brass inserts side. Thus, space points that are far from the brass inserts are shifted more than those that are closer.

No significant asymmetry is observed for the $\sigma^{0.99}_{\Delta\theta}$ distribution. The values of $\sigma^{0.99}_{\Delta\theta}$

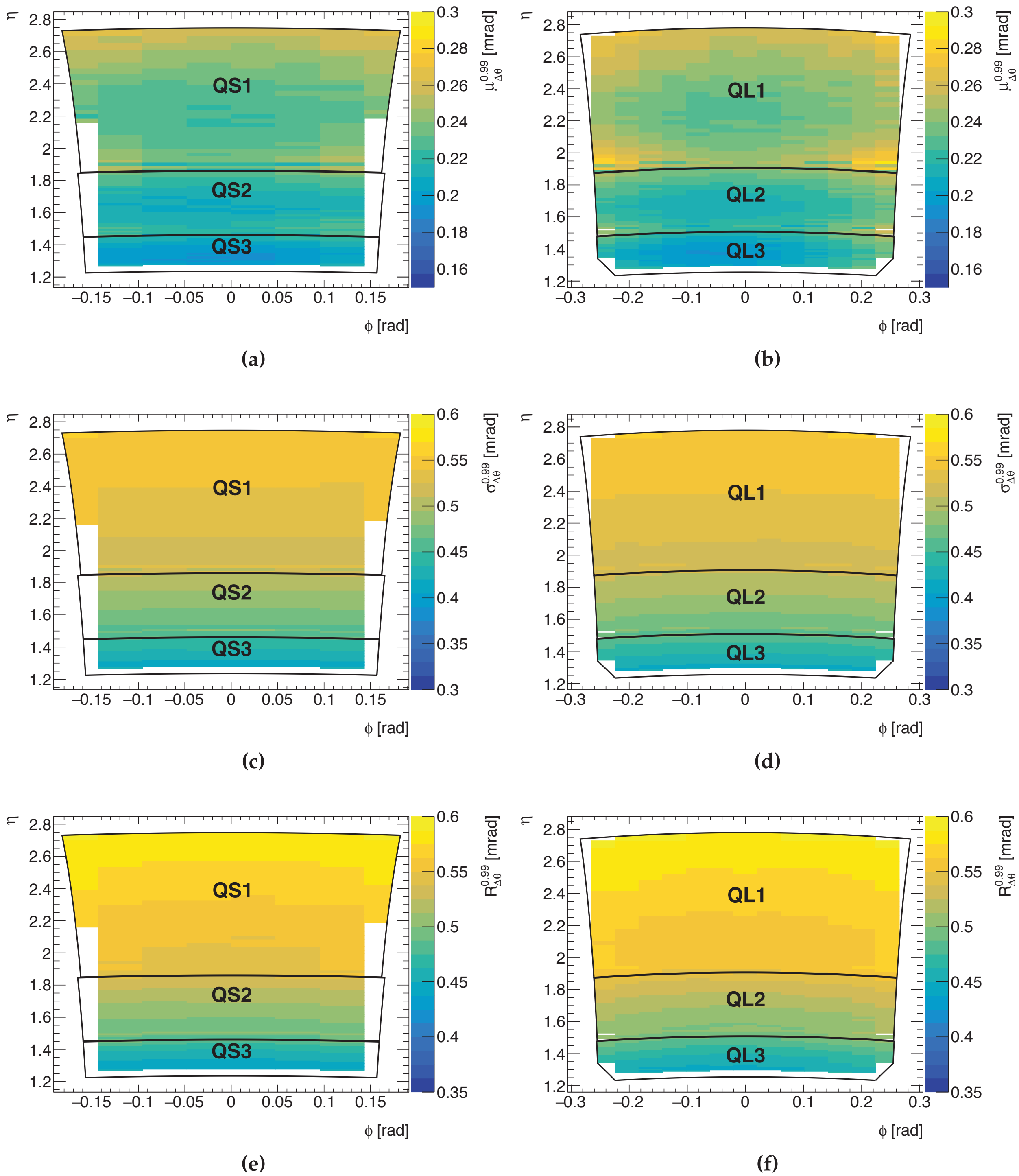

Figure 4.7: Values of (a)-(b) $\mu_{\Delta\theta}^{0.99}$, (c)-(d) $\sigma_{\Delta\theta}^{0.99}$ and (e)-(f) $R_{\Delta\theta}^{0.99}$ as a function of the logical pad. Values for the small sector are shown in (a)-(c)-(e) and for the large sector in (b)-(d)-(f). The black overline highlights the limits of the sector first layer when projected in the η-ϕ space. The orientation of the quadruplets in the η-ϕ space is inverted with respect to the orientation in the x-y space shown in Fig. 4.2.

are very close to the value predicted by the analytic formula of Eq. A.6 of Appendix A which assumes a perfect detector of finite intrinsic spatial resolution. This indicates that construction non-conformities tend to bias rather than smear the $\Delta\theta$ distribution over the area of a logical pad.

The value of $R^{0.99}_{\Delta\theta}$ is well below 1 mrad everywhere for both the small and large sectors. It implies that the current construction tolerances should succeed in delivering detectors satisfying the required online track reconstruction performances for the upgrade of the ATLAS muon detector system.

4.8 Sensitivity to simulation parameters

The values of $R^{0.99}_{\Delta\theta}$ obtained from the simulation depend on the construction tolerances used to randomly generate the non-conformities. For practical considerations, construction tolerances are subject to modifications before or even during sTGC module production. Construction tolerances could potentially be raised because of production costs as they are directly related to the fraction of sTGC components that are rejected because they are out-of-specification. Furthermore, the intrinsic spatial resolution and hit efficiency delivered by the sTGC modules during ATLAS operation could be different from the simulated one and change the conclusions drawn from the simulation studies. Thus, for all these reasons, the dependence of the results presented in Section 4.7 as a function of the simulation parameters must be understood.

The maximum value of $R^{0.99}_{\Delta\theta}$ over all logical pads is used as the metric to compare the effects of the different simulation parameters. Results from Section 4.7 show that the values of $R^{0.99}_{\Delta\theta}$ are very similar for the small and large sector simulations. Thus, for simplicity, the study of the sensitivity of the results on different simulation parameters is done only with the small sector.

Table 4.4 shows the simulated values of $R^{0.99}_{\Delta\theta}$ when varying one of the construction non-conformity tolerances. The offset and scale non-conformities have the largest impact on the angular resolution when they are increased. The value of $R^{0.99}_{\Delta\theta}$ stays below 1 mrad even when doubling all construction tolerances.

Factor	Mechanical construction non-conformity						
	Rotation	Offset	Scale	Parallelism	z-position	Gluing	All
0.5	0.59	0.57	0.59	0.59	0.59	0.59	0.57
1 (nominal)	**0.59**						
2	0.60	0.70	0.62	0.60	0.59	0.59	0.74
5	0.62	1.24	0.78	0.65	0.60	0.60	1.41
10	0.76	2.30	1.23	0.89	0.83	0.73	2.67

Table 4.4: The value of $R^{0.99}_{\Delta\theta}$ in milliradians obtained when varying the construction tolerances of Table 4.1 individually by a factor. The nominal value of $R^{0.99}_{\Delta\theta}$ is shown for reference. The last column indicates the combined effects of raising all constructions tolerances by the same factor.

Table 4.5 shows the values of $R^{0.99}_{\Delta\theta}$ when varying the sTGC intrinsic spatial resolution. The value of $R^{0.99}_{\Delta\theta}$ increases by approximately 0.200 mrad when the spatial resolution is increased by 100 µm. This result is consistent with the analytic expression of Eq. A.6 presented in Appendix A.

σ_{sTGC} [µm]	$R^{0.99}_{\Delta\theta}$ [mrad]
50	0.28
150	0.41
250	**0.59**
350	0.80

Table 4.5: The value of $R^{0.99}_{\Delta\theta}$ in milliradians as a function of the sTGC intrinsic spatial resolution. The nominal value used in the simulation is in bold font.

The simulation is not sensitive to changes in the hit efficiency. The values of $R^{0.99}_{\Delta\theta}$ for simulations performed between a hit efficiency of 80% and 100% do not significantly differ. Analytical expressions in Appendix A show that the value of $\sigma_{\Delta\theta}$ varies by approximately 5% when changing the hit efficiency from 100% to 80%. The increase in $\sigma_{\Delta\theta}$ due to hit efficiency effects does not cause a noticeable difference to the value of $R^{0.99}_{\Delta\theta}$.

Simulation studies presented in this chapter confirmed that the manufactured sTGC modules will meet the NSW specifications given the current values of construction tolerances used during quality control. The simulation, however, assumed specific values for the sTGC intrinsic spatial resolution and hit efficiency. In order to validate those simulation parameters, a measurement of the intrinsic spatial resolution is presented in Chapter 5. Furthermore, the sTGC spatial resolution and hit efficiency are measured with cosmic-rays for all manufactured sTGC modules using techniques described in Chapter 6.

5

sTGC performance characterization

Performance studies of the small-strip Thin Gap Chamber (sTGC) technology are presented in this chapter in the context of the New Small Wheel (NSW) detector modules specifications defined in Section 3.3. The performance studies were carried out to validate the sTGC technology before the beginning of detector manufacturing in 2018. The first performance requirement under study is the intrinsic spatial resolution, which must be adequate to provide the rejection rate of fake muons required to maintain a Level-1 muon trigger rate within the experiment's readout capability. Additionally, the offline spatial resolution of the NSW detector modules must be similar to that of the current end-cap inner muon station precision detectors, which includes the MDT and CSC technologies, such that the reconstructed muon momentum resolution is not degraded following the NSW installation. Finally, the NSW modules must have a sufficiently low time jitter to perform an accurate bunch crossing identification of the detector hits.

Intrinsic strip spatial resolution measurements, using cosmic rays as a muon source, are presented in Section 5.1. Measurements were performed as a function of the muon angle of incidence. An intrinsic strip spatial resolution measurement in a test-beam setup with perpendicular pions is described in Section 5.2. A time jitter measurement of sTGC pads using cosmic rays is presented in Section 5.3. Finally, a summary of the measurements in the context of the NSW performance requirements is presented in Section 5.4.

5.1 Intrinsic spatial resolution measured with cosmic rays

Measurements presented in this section aim at characterizing the spatial resolution variations as a function of the muon angle of incidence and at comparing the impact on the spatial resolution of the two different charge cluster reconstruction algorithms planned to be used during NSW operation. The measurements are necessary to determine whether the intrinsic spatial resolution delivered by a sTGC detector plane is sufficient to perform fake muon discrimination in the NSW as well as perform a precise offline muon reconstruction. The weighted average cluster reconstruction algorithm will be used online as part of the Level-1 muon trigger reconstruction. The cluster reconstruction based on a Gaussian fit will be used in the offline reconstruction of muon candidates. The measurements were performed at the McGill sTGC Testing Facility, described in Chapter 6, using a prototype sTGC quadruplet. The spatial resolution measurement is performed by comparing the position of a strip space point measurement to that of a reference track. The measurement was performed in-situ, meaning that reference tracks were obtained from the quadruplet itself.

5.1.1 Experimental setup

A schematic of the setup used to measure the spatial resolution of strip electrodes using cosmic-ray muons is shown in Fig. 5.1. The tested sTGC quadruplet prototype had dimensions 40×60 cm^2. The quadruplet was manufactured following the same specifications as those to be used for the production of NSW modules. The quadruplet was positioned on one of the drawers of the cosmic-ray hodoscope of the Testing Facility. Two scintillator detector planes, which are part of the Testing Facility cosmic-ray hodoscope, were used to generate a data acquisition trigger signal. A trigger signal was issued upon the coincidence between signals from the top and bottom scintillator detector planes. A full description of the trigger signal processing is found in Chapter 6. Due to limitations in the availability of front-end readout electronics, strip and wire channels from only three of the four layers of the quadruplet were read out. An area corresponding to 64 strips was instrumented and provided the y-coordinate of the muon trajectory. Anode wires were ganged in groups of 10 resulting in wire readout channels corresponding to a 1.8 cm wide region of the detector. Wire readout channels provided the muon x-coordinate. The z-coordinate of the sTGC space points was defined as the z position of the anode wire planes. Pad readout channels were not used for this measurement. The operating voltage was set to the nominal value of 2.9 kV for all gas volumes under test.

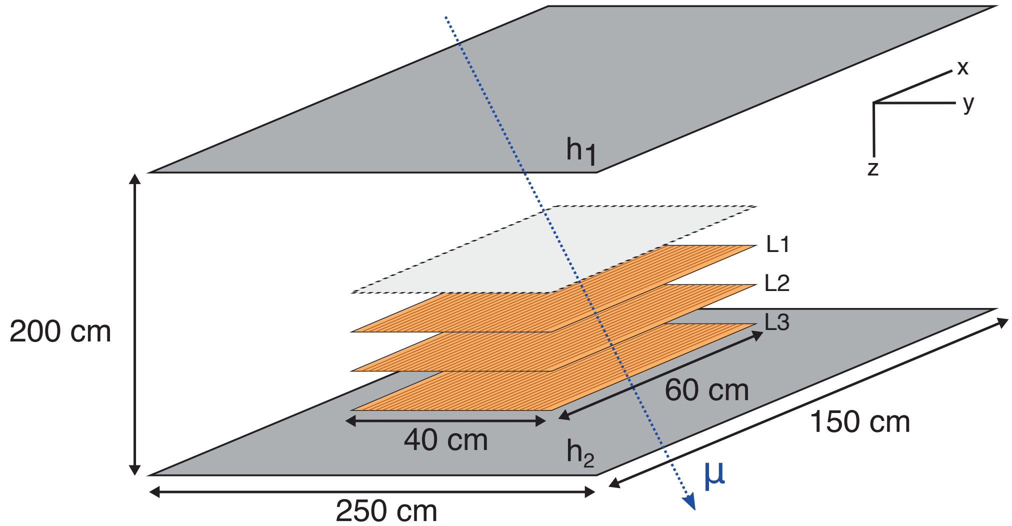

Figure 5.1: Schematic diagram of the experimental setup used for the strip intrinsic spatial resolution measurement performed with cosmic-ray muons. The plastic scintillator detector planes used to provide a data acquisition trigger signal are represented by the areas identified as h_1 and h_2. Three out of four gas volumes of the sTGC module prototype are read out. Layers under test are denoted L1, L2 and L3. The right-handed Cartesian coordinate system used to define the track space point coordinates is shown. The x-axis is parallel to the readout strips, drawn on each tested layer. The y-axis is perpendicular to the strips. The z-axis is perpendicular to the detector planes. The z-spacing between the gas volume is approximately 10.8 mm. The schematic diagram is not to scale.

A schematic diagram of the main components of the data acquisition system used to read out the wire and strip electrodes is shown in Figure 5.2. The signal from the strip and wire electrodes was read out using the NSW prototype readout ASIC[1], the VMM1 [109], developed for both sTGC and Micromegas detector technologies. A schematic diagram that describes the VMM1 signal processing is shown in Fig. 5.3. Each VMM1 ASIC has 64 channels with charge amplifier, shaper and discriminator functions. The VMM1 charge amplifier polarity is configurable which allows for the readout of the sTGC

1. Application Specific Integrated Circuit

anode wires and cathode strips signal. The shaper integration time and discriminator threshold are configurable. The threshold level can also be fine-tuned for each individual readout channel. Each VMM1 channel has an internal test pulser with configurable input charge used for calibration. The VMM1 records the detector signal peak and time of readout channels above threshold. The peak and time information is recorded as analog voltage levels and stored by an analog multiplexer built into the VMM1. The VMM1 can be configured, using the so-called "neighbour triggering" feature, to read out channels that are neighbours of those with a signal above threshold. Neighbour triggering is used for strip electrodes readout. Each individual VMM1 ASIC is fitted to a Front-End Board (FEB) that features all the necessary interfaces for configuration and readout. Adaptor boards, soldered directly to the sTGC, are used to provide the necessary connectivity between the electrode readout channels and the FEBs.

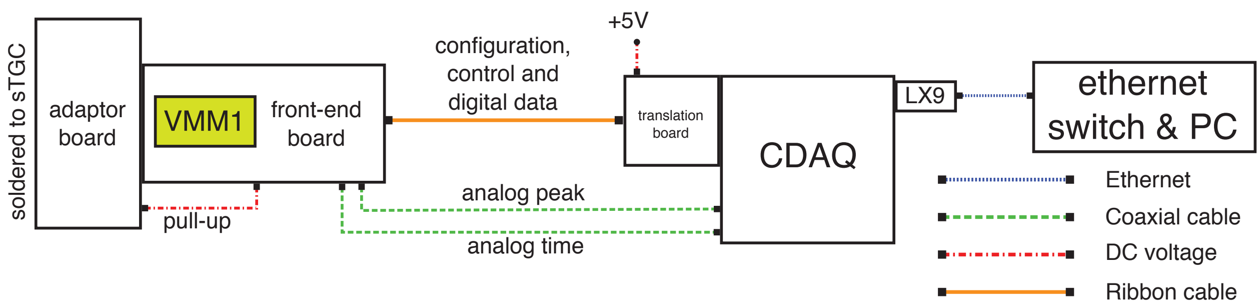

Figure 5.2: Schematic diagram of the data acquisition system associated with a single VMM1 ASIC used to read out wire and strip electrodes. The translation board is used to convert the digital voltage levels for communication between the CDAQ and the front-end board. The translation board also provides power to the CDAQ and the front-end board through the +5V input. The pull-up is a DC voltage level used to bias the signal from sTGC strips and is required by the VMM1 to read out a signal of positive polarity.

Custom-built Compact Data Acquisition (CDAQ) boards handle the configuration and control of each individual VMM1. A CDAQ is connected to a VMM1 FEB through a ribbon cable, used for digital communication, and two coaxial cables, for analog transmission. The hodoscope trigger signal is distributed in parallel to each individual CDAQ board. Upon receipt of a trigger signal, the CDAQ increments an internal counter and requests the peak and time voltage levels of each readout channel stored in the VMM1 analog multiplexer. The voltage levels are transmitted through the coaxial cables and the channel number through the ribbon cable. The CDAQ then digitizes the input analog voltage levels. The peak and time values are stored in the CDAQ buffer in arbitrary units called "ADC counts"[2]. The CDAQ then assembles data packets that contain the event number, provided by its built-in counter, and the digitized peak and time values. Then, data packets are transmitted to a commercial board[3] mounted on the CDAQ and used to transmit the data packets to a desktop computer through an Ethernet port using the UDP protocol. A DAQ software running on the desktop computer collects the CDAQ data packets. The DAQ software combines the CDAQ board IP[4] addresses to the data packets making data words. Finally, the data words are saved to permanent storage.

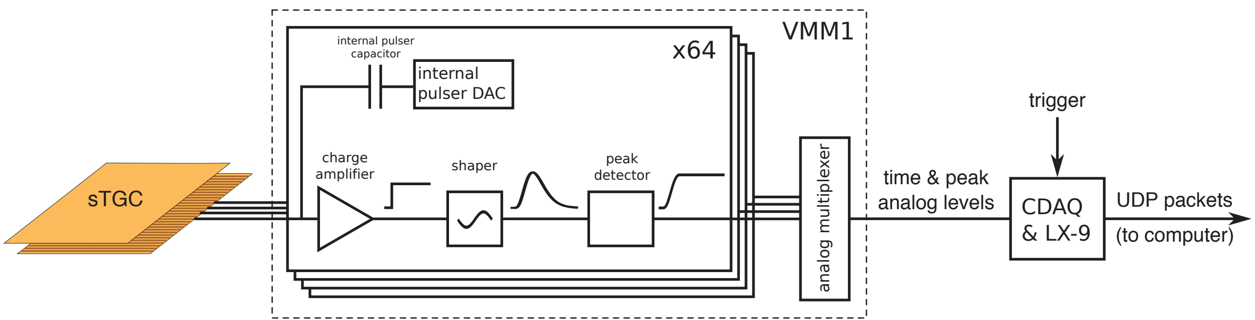

Figure 5.3: Schematic diagram of the VMM1 signal processing chain. The signal from sTGC electrodes (strips on the schematic diagram) is transmitted to one of the 64 VMM1 readout channels. Elements that are part of the VMM1 ASIC are enclosed in the dashed rectangle.

5.1.2 Data acquisition

Measurements from multiple data acquisition runs, performed between October 14$^{\text{th}}$ and November 18$^{\text{th}}$ of 2016, were combined to obtain the results presented in this section. The combined runs correspond to a total data taking time of approximately 8

2. Analog-to-Digital Converter counts.
3. Xilinx Spartan-6 FPGA LX9 Microboard, AES-S6MB-LX9-G.
4. Internet Protocol.

days. The typical data taking time of a single run is 24 hours. Approximately 10^8 trigger signals were issued by the trigger system over the data taking time. A total of 10.8×10^6 cosmic-ray muon events were recorded and included in the dataset. The VMM1 ASICs were configured with a gain of 3.0 mV/fC and an integration time of 25 ns for strip readout and a gain of 0.5 mV/fC and an integration time of 200 ns for wire readout.

5.1.3 Data preparation

Data preparation is the offline decoding and preprocessing of data words before muon track reconstruction. The data preparation process is described below.

Event building and decoding

The event building of a data acquisition run is performed by aggregating data words associated with the same event number. Events with corrupted data are identified and removed from the dataset during the event building stage. The binary event data is decoded and then compressed into a `ROOT` [110] format for offline analysis.

Identification of bad readout channels

A small fraction of sTGC channels is not responsive due either to a malfunctioning VMM1 readout channel or a bad connectivity in the signal line between the sTGC electrodes and the VMM1 readout channels. Nevertheless, data associated with bad channels can be recorded because of noise in the signal line or, in the case of strip readout channels, the neighbour triggering feature. Bad channels are identified offline using the decoded and pre-processed data. Bad channels feature an unusually small number of hits, or occurrences in data, during a data acquisition run. Additionally, the signal peak value of neighbour triggered bad channels is typically very small. Based on these attributes, the following conditions are required to identify a bad channel:

- Less than n hits on the channel over a predefined data acquisition time period.
- The fraction of hits on the channel that are below a threshold P_{th} must be greater than f.

The values $n = 10$, $f = 0.95$ and $P_{\text{th}} = 1200$ ADC counts are typically used for a data acquisition run of 24 hours. On average, approximately 2% of the VMM1 readout channels are identified as bad.

The data associated with bad readout channels are removed from the dataset. An accurate charge cluster centroid measurement cannot, however, be obtained if the ionization charge in the chamber is produced in a region overlapping a bad readout channel. Therefore, strip data of any sTGC layer that records information from a bad channel or one of its neighbour are discarded and not considered for further analysis.

Baseline subtraction

An input signal to the VMM1 charge amplifier is shaped with respect to a fixed DC baseline voltage. The amplitude A_i of a signal on a channel denoted i is therefore obtained by subtracting the baseline of a channel (baseline$_i$) from its measured signal peak value (peak$_i$). The input charge Q_i on an individual channel is then determined from the measured signal amplitude and amplifier gain using

$$Q_i \text{ [fC]} = \frac{A_i \text{ [mV]}}{\text{gain [mV/fC]}} = \frac{\text{peak}_i \text{ [mV]} - \text{baseline}_i \text{ [mV]}}{\text{gain [mV/fC]}}. \tag{5.1}$$

For the analysis presented here, the signal peak value is digitized and measured in units of ADC counts. Therefore, for most of the analysis, the charge, the signal amplitude and the baseline are also expressed in units of ADC counts. The charge amplifier gain is assumed identical for all readout channels of a given electrode type.

The channel-to-channel baseline variations correspond to approximately 2% of the typical signal peak value of a single readout channel. This variation is large compared to the electronic noise level that is of the order of 0.1%. Thus, baseline variations are sufficiently large to significantly bias the reconstruction of a charge cluster centroid value. The baseline value of each individual readout channel must therefore be measured for a precise charge cluster centroid reconstruction. An example of baseline variations from the 64 readout channels of a VMM1 is shown in Fig. 5.4.

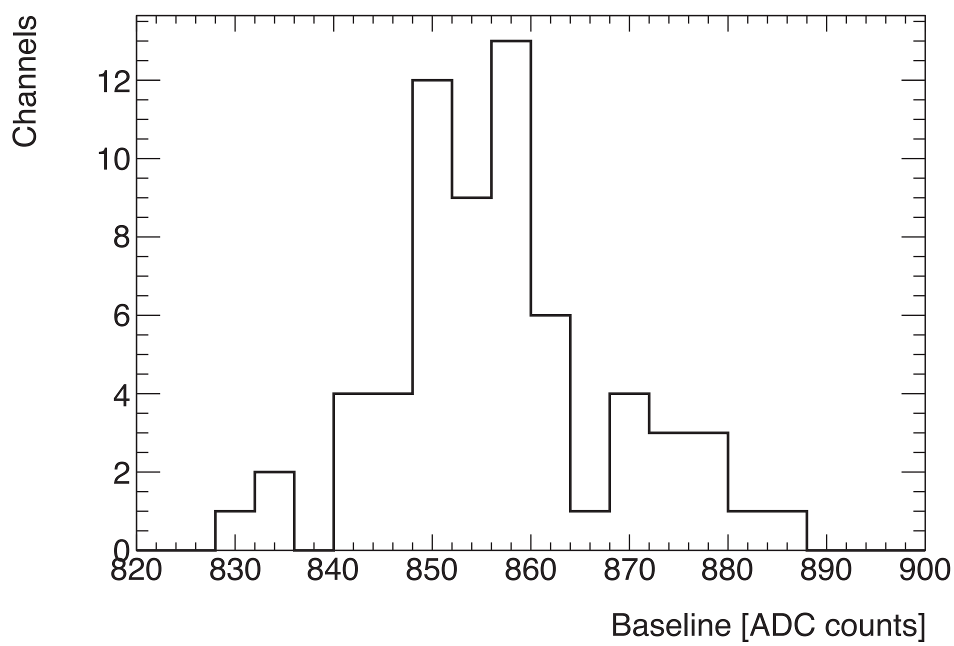

Figure 5.4: Baseline value distribution for the 64 channels of a representative VMM1 ASIC.

The baseline of a VMM1 readout channel is measured by injecting test pulses in one of the neighbour channels. If neighbour triggering is activated and the pulsed channel is above threshold, the VMM1 outputs the detected peak value of both the pulsed channel and the channel of interest. The peak value measured on the channel of interest corresponds to the baseline value assuming there is no capacitive coupling between readout channels. A description of VMM1 baseline measurement techniques, including the one used for this analysis, is found in [111]. The measured baseline values are subtracted, on a channel-by-channel basis, from the signal peak values of the dataset to obtain the signal amplitude. The signal amplitude is proportional to the charge collected on each readout channel as in Eq. 5.1.

Signal saturation

The dynamic range of the VMM1 charge amplifier is limited and, as a consequence, signal peak saturation is observed in the event of a large charge deposition on a VMM1 readout channel. Saturation effects are readily observed from the VMM1 charge calibration curve shown in Fig. 5.5(a). Signal saturation degrades the charge amplifier linearity which is important for an accurate charge cluster centroid reconstruction.

Saturated hits are identified by a signal amplitude value above a predefined saturation threshold P_{sat}. The chosen value of P_{sat} is the same for all channels of a VMM1 and depends on the charge amplifier and shaper configuration. As an example, the strip signal amplitude distributions obtained in cosmic-ray muon data for different choices of VMM1 amplifier gain and integration time are shown in Fig. 5.5(b).

In order to mitigate the effects of saturation, sTGC layers having one or more saturated strip channels are not used further in the analysis. Layers with saturated wire channels are not removed because charge cluster reconstruction is not performed on wire channels data.

5.1.4 Charge cluster reconstruction

A charge cluster is defined as a series of contiguous strip channels with non-zero signal amplitudes.

Some clusters are identified as incomplete because they are located on the sides of the instrumented area or in the neighbourhood of a bad channel. Incomplete clusters

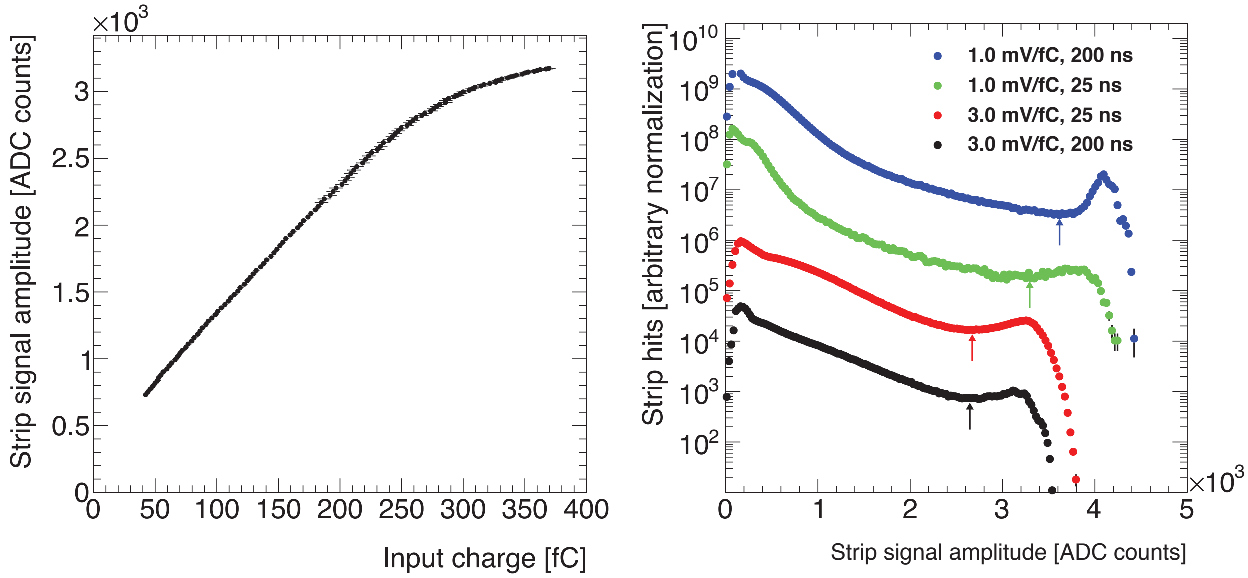

(a) **(b)**

Figure 5.5: (a) Charge response calibration of a VMM1 channel using a gain of 3.0 mV/fC and an integration time of 25 ns. The amplifier linearity is lost at an input charge of approximately 250 fC. (b) Distributions of strip signal amplitude in cosmic-ray muon data obtained with different VMM1 configurations. The arrows indicate the onset of saturation effects and are positioned at the approximate value of P_{sat} used for charge cluster reconstruction.

are rejected from the analysis because the reconstruction of their cluster centroid position would be biased. This data quality requirement removes approximately 20% of strip-clusters.

Based on simulation studies, clusters are expected to typically consist of signals from 3 to 5 strips [33]. The use of neighbour triggering in the VMM1 guarantees that all clusters contain information from at least 3 strips. Clusters larger than 5 strips likely originate from δ-ray production which broadens the spread of primary ionization in the sTGC gas volume. The distribution of the cluster size, or strip multiplicity, obtained in cosmic-ray data after applying all the cleaning cuts discussed above is shown in Fig. 5.6(a). For this analysis, clusters are required to be made of no more than 5 strips. Approximately 15% of clusters are rejected by this requirement. This rejection fraction varies as a function of the VMM1 integration time, gain and discriminator threshold used for the cosmic-ray data taking.

The distribution of the number of clusters on a single sTGC layer, after the application of all quality cuts discussed so far, is shown in Fig. 5.6(b). Approximately 1.5% of events recorded in cosmic-ray data taking runs are reconstructed to have more than one cluster on at least one sTGC layer. The small flux of cosmic-ray muons and the short readout time-window of the DAQ system makes the probability of recording data from two muons in a single event very small, of the order of 10^{-6}. Events with multiple clusters on a single layer are likely to originate from δ-rays or particle showers rather than events with two muons. Therefore, events with sTGC layers having more than one clusters are discarded from the dataset.

The cluster centroid position, which gives an estimate of the muon position in the sTGC gas volume, is obtained using the signal amplitudes Q_k and the positions y_k of the center of readout strips indexed k. The two centroid finding algorithms used in this dissertation, the Gaussian Fit (GF) and the Weighted Average (GA), are described below.

Gaussian Fit algorithm

Charge cluster centroid finding using the Gaussian Fit (GF) algorithm is performed by fitting a Gaussian function on the (y_k, Q_k) points of the strip charge profile. The Gaussian function is defined as

$$G(y; \mu_G, \sigma_G, Q_G) = \frac{Q_G}{\sigma_G\sqrt{2\pi}} \exp\left[-\frac{(y-\mu_G)^2}{2\sigma_G^2}\right] \tag{5.2}$$

where μ_G is the charge cluster centroid position, σ_G is the cluster width and Q_G is the cluster integral which gives an estimate of the total charge induction on the strip cathode.

For clusters of three strips, parameters of the Gaussian function are obtained di-

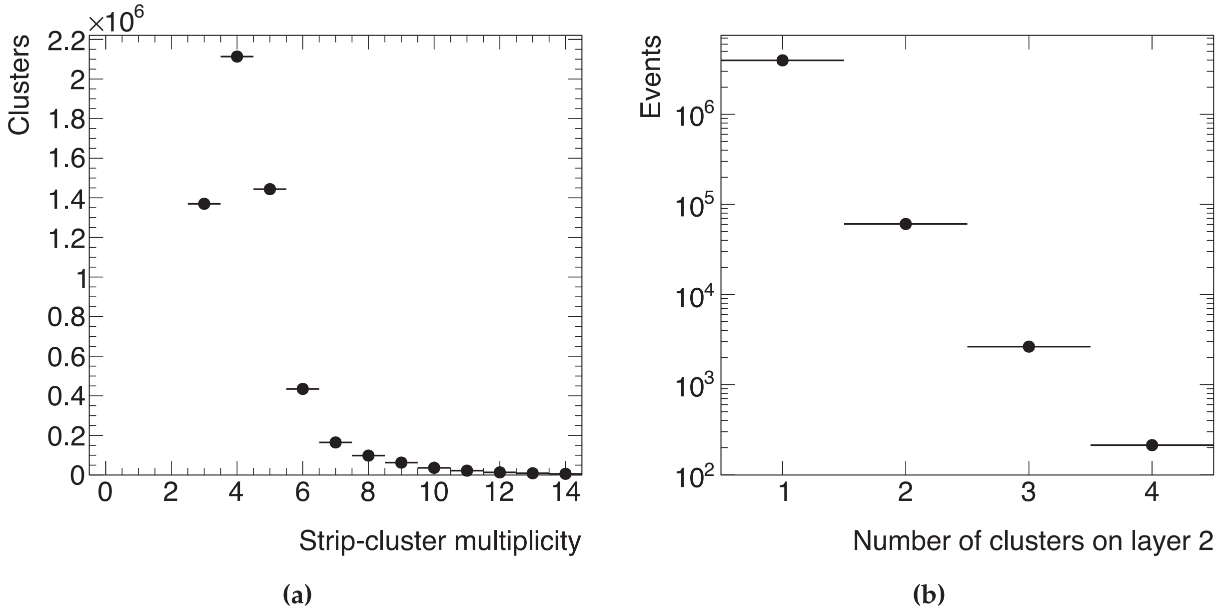

Figure 5.6: (a) Distribution of the charge cluster strip multiplicity for layer 2 and (b) distribution of the number of clusters for the same layer. The VMM1 gain is 3.0 mV/fC and the integration time is 25 ns.

rectly using the Caruanas analytic formula [112]. For clusters of more than three strips, an initial estimate is obtained using the Caruanas formula and then a least squares regression of the Gaussian function of Eq. 5.2 is performed. The cluster is not used further in the analysis if the fitted position μ_G is not located within the region spanned by the strips making up the cluster.

Weighted Average algorithm

The Weighted Average (WA) charge cluster centroid finding algorithm is performed by calculating the center of gravity of the strip charge profile using the values (y_k, Q_k):

$$\mu_W = \frac{\sum_k y_k Q_k}{\sum_k Q_k}. \tag{5.3}$$

The WA algorithm is advantageous since it is numerically stable, computationally efficient, and the cluster centroid position is systematically reconstructed to be within the region spanned by the strips making the cluster. Larger differential non-linearity biases are, however, expected when using the WA algorithm compared to other centroid finding techniques [63, 66]. The GF technique, for example, accounts for the bell shape of the charge profile of the cluster by effectively giving more weight to the outer strips thereby providing a more accurate cluster centroid value. The WA algorithm will be used by the NSW trigger algorithm for online cluster centroid finding [97].

5.1.5 Track reconstruction

Tracks are reconstructed independently in the y-z and x-z planes using, respectively, strip and wire data from the three readout sTGC layers. The y-coordinates of the space points is obtained based on the centroid position of the charge clusters that satisfied all quality cuts. The x-coordinates of the space points are taken to be the center of the wire group having the largest signal amplitude on each sTGC layer. The z-coordinates of the space points are taken to be the position of the anode wire planes. Tracks are obtained from a least-squares fit of the data to a first-order polynomial function.

5.1.6 Analysis

The spatial resolution measurement along the y-coordinate is obtained by comparing the position of the y-coordinate given by the strips with the expected position obtained from a reconstructed reference track. Space point coordinates measured by layer i of the sTGC quadruplet prototype are denoted x_i, y'_i and z_i. The value of y'_i is the charge cluster centroid position. Whether the cluster centroid position is obtained using the GF or the WA algorithm is specified in the text. Biases on the space points y-coordinates considered in this analysis are the inter-layer misalignments and the differential non-linearity bias. The method used to correct the space points y-coordinate for each of these two biases is described later in this section. The corrected value of y'_i, denoted y_i, is obtained from the transformation

$$y_i = y'_i - \delta y_i^{(\text{align})} - \delta y_i^{(\text{DNL})} \tag{5.4}$$

where $\delta y_i^{(\text{align})}$ and $\delta y_i^{(\text{DNL})}$ are, respectively, the corrections for inter-layer misalignments and the differential non-linearity bias for layer i. The y-coordinate of the space points obtained after applying just one of these two possible corrections is obtained with the transformations

$$y_i^{(\text{DNL})} = y'_i - \delta y_i^{(\text{DNL})} \tag{5.5}$$

and

$$y_i^{(\text{align})} = y'_i - \delta y_i^{(\text{align})}. \tag{5.6}$$

To measure the spatial resolution of a layer of interest, denoted j, two types of reference tracks are defined. An "inclusively" reconstructed track is a track obtained from a least-squares fit that includes the space point of layer j while an "exclusively" reconstructed track excludes the space point of layer j. The reconstructed reference track y-coordinate on the layer of interest (i.e. at $z = z_j$) is denoted $y_{\text{in},j}$ ($y'_{\text{in},j}$) for the inclusive case and $y_{\text{ex},j}$ ($y'_{\text{ex},j}$) for the exclusive case if the track is obtained using the values y_i (y'_i) of the corrected (non-corrected) y-coordinates of the space points. The same notation is used if the reference track is obtained using the values of $y_i^{(\text{DNL})}$ or $y_i^{(\text{align})}$, in which case the suffixes DNL or align are used, respectively, instead of the prime notation to denote the reference track y-coordinate on layer j.

Residuals obtained with respect to inclusively (exclusively) reconstructed tracks are defined as $y_j - y_{\mathrm{in},j}$ ($y_j - y_{\mathrm{ex},j}$). Both inclusive and exclusive residual distributions are used to obtain an estimate of a sTGC layer spatial resolution along the y-coordinate.

Correction factors for both misalignments and differential non-linearity effects are obtained using an iterative procedure whereby tracks are reconstructed at each iteration using y-coordinate values obtained using corrections from the previous iteration. New misalignment and differential non-linearity corrections are derived and the procedure repeats until it converges to stable values of misalignment and differential non-linearity corrections.

The procedures used to calculate misalignment corrections and differential non-linearity corrections, as well as the iterative procedure used in the analysis are described in the paragraphs below.

Inter-layer misalignments correction

The inter-layer misalignments correction parameters are obtained first at each step of the iterative procedure. The analysis presented in this chapter uses space points from three detector layers and assumes straight muon tracks. Strip muon tracks defined in the y-z plane are parameterized with two parameters which are the angle and the offset (i.e. the track position at $z = 0$). Therefore, misalignments can only be defined with respect to two "reference" detector planes, assumed to be at their nominal position with one plane assumed misaligned. For the analysis presented below, a misalignment of layer 3 in rotation and translation in the x-y plane is assumed with respect to layers 1 and 2 used as reference planes. Other potential misalignments, such as variations in the z position of the wire planes or shift in x of the space points are not corrected. The alignment correction is parameterized as

$$\delta y_i^{\text{align}} = \begin{cases} 0, & \text{i=1,2} \\ \phi\, x_{\text{in},i} + b, & \text{i=3} \end{cases} \tag{5.7}$$

where ϕ and b are obtained, at each step of the iterative procedure, using a matrix technique described in Appendix B. The variable $x_{\text{in},i}$ denotes the position on layer i of the inclusively reconstructed track in the x-z plane. A first degree polynomial fit of the mean of the inclusive reference track y-residuals as a function of $x_{\text{in},i}$ is shown in Fig. 5.7(a). In order to show the size of the inter-layer misalignments corrections, the space points y-coordinates are obtained using the GF algorithm and are corrected for the differential non-linearity bias; a correction that is explained later in the text. The slope and offset parameters of the first degree polynomial fit are used as inputs of the matrix technique used to obtain ϕ and b. The y-residuals used for the fit are obtained using tracks at an angle $|\theta_{yz}| < 150$ mrad. As expected, the y-residuals are consistent with being the same for the outer layers because of the z-symmetry. The mean of the inclusively reconstructed reference track y-residuals using corrected space points are shown in Fig. 5.7(b). The mean is close to zero for all x positions.

Differential non-linearity correction

The differential non-linearity correction parameters are obtained after the inter-layer misalignments calculation at each step of the iterative procedure. For the analysis presented in this chapter, differential non-linearity corrections are only applied to the charge cluster centroid positions obtained using the GF algorithm. The differential non-linearity bias is a function of the cluster centroid position relative to the closest inter-strip gap center y_i^{rel} and is parameterized as

$$\delta y_i^{(\text{DNL})} = a_m \sin\left(2\pi y_i^{\text{rel}}\right) \tag{5.8}$$

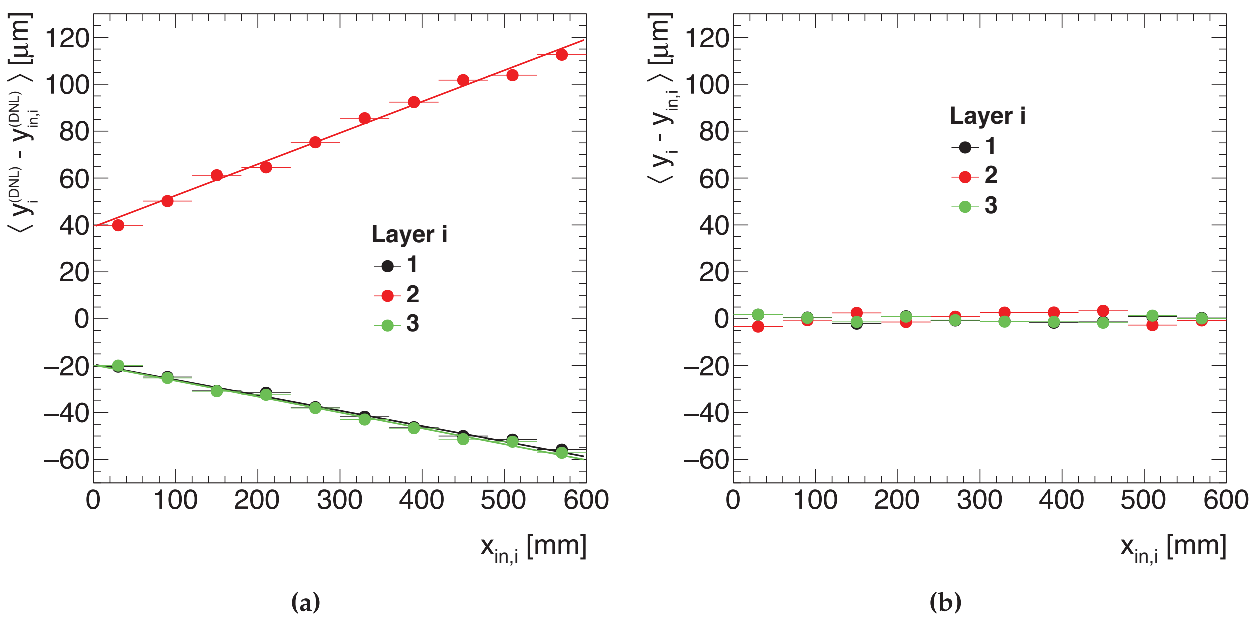

Figure 5.7: Mean of the inclusive reference track y-residuals for each tested layer i as a function of the reference track x-coordinate on the layer (a) without and (b) with inter-layer misalignments correction. The differential non-linearity corrections are applied in both cases to all space points. The non-corrected y-residuals are fitted to a first order polynomial.

where a_m is the amplitude of the differential non-linearity bias for a cluster strip multiplicity m. The amplitudes a_m are assumed to be the same for all layers of the sTGC under test since all layers have the same geometry and construction.

The differential non-linearity correction is obtained by minimizing the amplitudes of the measured differential non-linearity bias in the parameter space of the correction parameters a_m. The value of the amplitude parameters a_m at each step l of the minimization procedure is

$$a_{m,l} = a_{m,l-1} + \frac{w}{3} \sum_{i=1}^{3} a^{\text{fit}}_{m,l-1,i} \tag{5.9}$$

where the amplitude $a^{\text{fit}}_{m,l-1,i}$ is obtained from the fit of the function of Eq. 5.8 on the y-

residuals of layer i, denoted $y^{(\text{align})}_{i,l-1} - y_{\text{ex},i,l-1}$, as a function of y^{rel}_i. The values of $y_{\text{ex},i,l-1}$ are obtained using an exclusively reconstructed reference track corrected for the differential non-linearity bias using the amplitudes of the previous step $l-1$. The same inter-layer misalignments correction is applied for all steps l of the minimization. The parameter w is a weight, smaller than unity, that prevents the divergence of the amplitude parameters during the minimization. The minimization is stopped when the condition

$$\left|\frac{a_{m,l+1} - a_{m,l}}{a_{m,l+1}}\right| < \varepsilon_{\text{DNL}} \tag{5.10}$$

is met for a predefined value of ε_{DNL}. The value of ε_{DNL} can be arbitrarily small. The minimization is always started using the values $a_{m,0} = 0$ for all m. The convergence condition is typically reached within 50 minimization steps using $w = 0.7$ and $\varepsilon_{\text{DNL}} = 10^{-6}$. Reference tracks at small angle, corresponding to $|\theta_{yz}| < 150$ mrad, are used for the calculation of the differential non-linearity correction.

The mean of the y-residuals for layer 2 as a function of y^{rel}_2, is shown in Fig. 5.8(a). In order to better observe the effects of the differential non-linearity, the inter-layer misalignments corrections are applied to the space points. The differential non-linearity correction obtained at convergence of the iterative procedure is also shown in the figure. The mean of the y-residuals for layer 2, obtained after applying both inter-layer misalignments and differential non-linearity corrections, is shown in Fig. 5.8(b). The mean of the y-residuals is close to zero which demonstrates that the corrections found at convergence of the minimization procedure are successful in reducing the differential non-linearity bias.

Iterative procedure

The correction parameters ϕ, b and a_m are ultimately obtained from the iterative procedure which combines the two techniques described earlier. At each iteration k, the

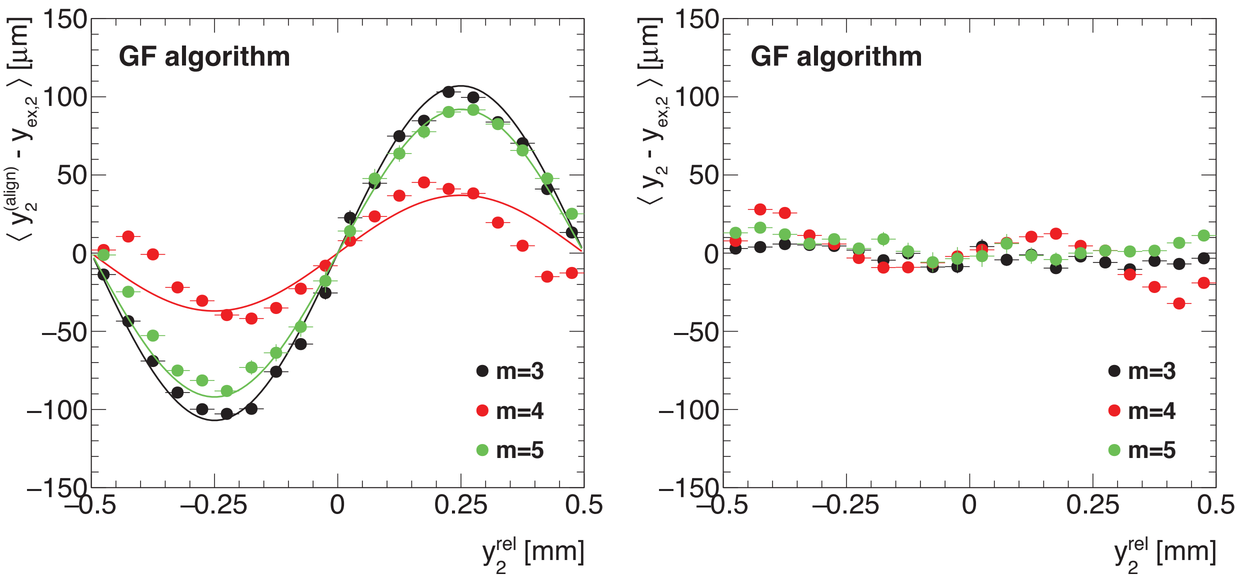

(a) **(b)**

Figure 5.8: Mean of the layer 2 y-residuals as a function of y_2^{rel} for different cluster strip multiplicities m (a) without and (b) with the differential non-linearity correction applied on the space points of layer 2. The exclusively reconstructed reference track space points are corrected for differential non-linearity effects in (a) and (b). The space points of all layers are corrected for inter-layer misalignments. The differential non-linearity corrections obtained at convergence of the iterative procedure are drawn as continuous lines in (a).

matrix technique used to correct the inter-layer misalignments and the differential non-linearity bias minimization procedure are used successively to obtain an increasingly accurate value of the correction parameters.

The correction parameters at each iteration k are denoted ϕ_k, b_k and $a_{m,k}$. The procedure stops at convergence, meaning that the conditions

$$\left|\frac{\phi_k - \phi_{k-1}}{\phi_k}\right| < \varepsilon, \qquad \left|\frac{b_k - b_{k-1}}{b_k}\right| < \varepsilon, \qquad \left|\frac{a_{m,k} - a_{m,k-1}}{a_{m,k}}\right| < \varepsilon \tag{5.11}$$

are met for a predefined value of ε. The value of ε can be arbitrarily small. Each iteration k comprises the following steps:

1. The parameters ϕ_k and b_k are obtained using the matrix technique with space points corrected for differential non-linearity only. The differential non-linearity correction is calculated using the amplitude parameters of the previous iteration $a_{m,k-1}$.

2. The amplitude parameters $a_{m,k}$ are obtained by following the minimization procedure. The space points used at this stage are corrected for inter-layer misalignments using the parameters ϕ_k and b_k of the current iteration.

The amplitude parameters are initialized with the value $a_{m,0} = 0$ for all m. Convergence with a tolerance $\varepsilon = 10^{-6}$ is reached at the third iteration ($k = 3$). The correction parameters obtained at convergence are shown in Table 5.1.

Parameter	Value
ϕ	(396±0.005) μrad
b	(113±2) μm
a_3	(107±13) μm
a_4	(37.0±4.1) μm
a_5	(92.0±8.4) μm

Table 5.1: Correction parameters obtained from the iterative procedure. The error on the ϕ and b parameters is obtained from the error on the linear fits to the mean y-residuals as a function of $x_{\text{in},i}$. The error on the amplitude parameters a_m is obtained from the sum in quadrature over all layers i of the fitted amplitudes $a^{\text{fit}}_{m,k,i}$ obtained at convergence.

Track residuals

The y-residuals are obtained using inclusively and exclusively reconstructed reference tracks with space points corrected using the parameters of Table 5.1. For comparison purposes, track residuals on the layer of interest are obtained using both the GF and WA cluster reconstruction algorithms. The NSW online track reconstruction algorithm uses the WA cluster reconstruction algorithm without applying a correction for differential non-linearity effect. Thus, in order to accurately measure the expected online intrinsic spatial resolution of the NSW sTGC detectors, the differential non-linearity correction is not applied to the space points obtained in this analysis using the WA algorithm.

The y-residuals are classified in bins of different inclusively reconstructed reference track angle θ_{yz}. Although the parameters of Table 5.1 were obtained using tracks at small angle, simulation studies suggest that the differential non-linearity bias parameters are invariant as a function of the angle θ_{yz} [66]. The misalignment correction is also not expected to vary as a function of the angle θ_{yz}. The distribution of the exclusive and inclusive y-residuals, denoted $\delta y_{\text{ex}} = y_i - y_{\text{ex},i}$ and $\delta y_{\text{in}} = y_i - y_{\text{in},i}$ respectively, are obtained for each individual angle bin. The y-residual distributions are fitted to a double Gaussian function defined as

$$G(\delta y_{\text{X}}) = \frac{A_s}{\sigma_s\sqrt{2\pi}} \exp\left[-\frac{(\delta y_{\text{X}} - \mu)}{2\sigma_s^2}\right] + \frac{A_b}{\sigma_b\sqrt{2\pi}} \exp\left[-\frac{(\delta y_{\text{X}} - \mu)}{2\sigma_b^2}\right] \tag{5.12}$$

where A_s and σ_s are the amplitude and width of the "signal" Gaussian function while A_b and σ_b describe the "background" Gaussian function. Both the signal and background Gaussian functions have the same mean μ. The index X denotes the residual type: "in" or "ex".

As an example, the y-residuals distributions for layer 2, obtained using the GF algorithm and selecting reference tracks at an angle $|\theta_{yz}| < 29$ mrad, are shown in Fig. 5.9.

Results

The width of the y-residual distributions provides a biased estimate of the intrinsic spatial resolution. The width of the exclusive y-residual distribution overestimates the spatial resolution because of the error on the calculated position of the exclusively reconstructed track on the tested layer. Conversely, the width of the inclusive y-residual

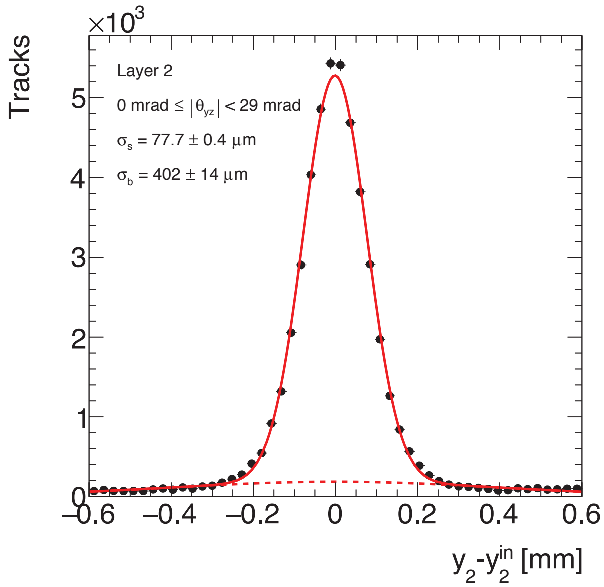

(a)

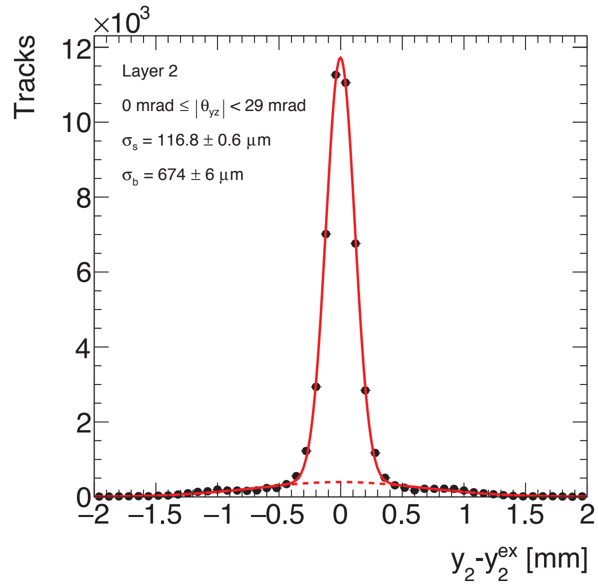

(b)

Figure 5.9: Distributions of reference track y-residuals on layer 2 for the (a) inclusive and (b) exclusive cases. The double Gaussian function fitted to the data is drawn on the distributions as a continuous red line. The background term of the fit function is drawn with a dashed line. The signal term accounts for about $A_s/(A_s + A_b) = 85\%$ of the events for both distributions. The signal fraction is approximately constant as a function of the reference track angle.

distribution underestimates the spatial resolution because the reference track is reconstructed using the strip cluster on the tested layer. For equally spaced detector planes, an unbiased estimate of the spatial resolution is obtained from the geometric mean of the widths of the inclusive and exclusive y-residual distributions [113, 114]

$$\sigma^2_{sTGC} = \sigma_{s,\text{in}}\, \sigma_{s,\text{ex}}. \tag{5.13}$$

The spatial resolution is obtained for each individual $|\theta_{yz}|$ angle bin. Results for layer 2 are shown in Fig. 5.10 with tracks reconstructed using the GF or the WA algorithms.

The spatial resolution is measured to significantly degrade with increasing track

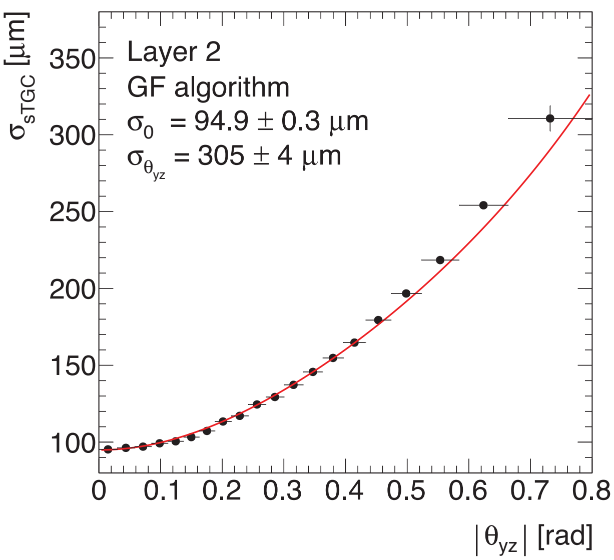

(a)

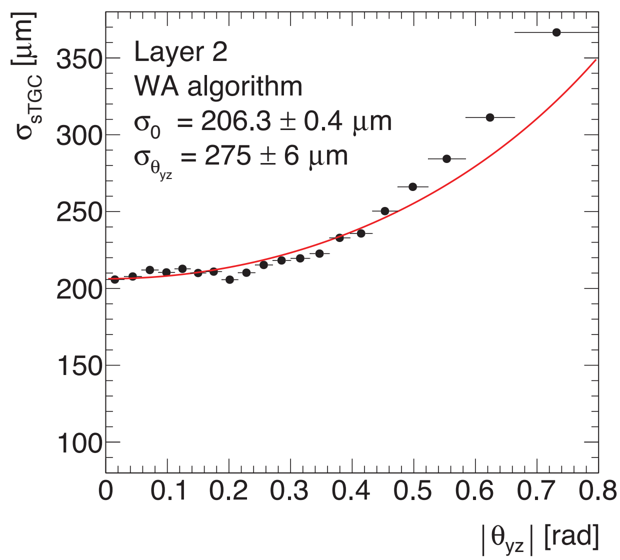

(b)

Figure 5.10: Intrinsic strip spatial resolution as a function of the reference track angle θ_{yz}. The y-coordinate of the space points on all layers is obtained using the (a) GF and (b) WA cluster reconstruction algorithms. The red line is a fit of the expected spatial resolution using the parameterization described in the text.

angle. The variation of the spatial resolution as a function of the θ_{yz} angle is due to statistical fluctuations of the primary ionization along the y-axis. The θ_{xz} angle is expected to have a lesser impact on the degradation because the primary ionization fluctuations along the x-axis do not influence the cluster centroid position measurement. The degradation in spatial resolution is expected to depend on the y-component of the muon trajectory in the gas volume, which is proportional to $\tan(\theta_{yz})$. Thus, the spatial resolution can be expressed using the parameterization

$$\sigma_{\text{sTGC}}^2 = \sigma_0^2 + \sigma_{\theta_{yz}}^2 \tan^2(\theta_{yz}) \tag{5.14}$$

which is a sum in quadrature of the intrinsic spatial resolution with perpendicular muons σ_0 and the contribution of charge production fluctuations in y denoted $\sigma_{\theta_{yz}} \tan(\theta_{yz})$. The parameter $\sigma_{\theta_{yz}}$ characterizes the angular dependence in the y-z plane. Following Rehak and Gatti [115], the parameter $\sigma_{\theta_{yz}}$ can be expressed as

$$\sigma_{\theta_{yz}} = \frac{2h}{\sqrt{12}} \frac{\sigma_Q}{\langle Q \rangle} \tag{5.15}$$

where h is the cathode-to-anode spacing and σ_Q and $\langle Q \rangle$ are respectively the width and mean of the distribution of charge production in the sTGC gas volume. The parameters σ_0 and $\sigma_{\theta_{yz}}$ are obtained from a fit of the parameterization of Eq. 5.14 to the resolution curves of Fig. 5.10.

As expected, the spatial resolution degrades as a function of the track angle in the y-z plane for both tested algorithms. The fitted curve is not in good agreement with the data points obtained using the WA cluster reconstruction algorithm due to distortions caused by the differential non-linearity bias, not corrected for in the WA algorithm case. As expected, the value of σ_0 is lower for the GF algorithm case because the differential non-linearity correction improves the strip spatial resolution. The measured value of $\sigma_{\theta_{yz}}$ is approximately 300 µm and is within 10% for both tested cluster reconstruction algorithms which shows that the impact of the algorithm on the spatial resolution variations as a function of the angle is small. The value of $\sigma_{\theta_{yz}}$ is an important parameter as it describes the variations of the strip intrinsic spatial resolution over the area of an NSW sTGC wedge.

The best strip spatial resolution obtained when using the WA algorithm and without correcting for the differential non-linearity bias is approximately 205 µm. This value is an estimate of the best possible resolution achievable in the ATLAS online trigger reconstruction which will use the WA algorithm. A more accurate measurement of the σ_0 parameter using the GF algorithm with a pion beam is presented in the next section to complement the conclusions of the current section.

5.2 Intrinsic strip spatial resolution measured in test-beam

The intrinsic strip spatial resolution measurement in a test-beam setup was performed in May 2014 at the Fermilab [5] Test-Beam Facility using a 32 GeV pion beam [67]. The goal of the test-beam measurement was the precise measurement of the spatial resolution for perpendicular track corresponding to the σ_0 parameter of Eq. 5.14. The measurement is important to confirm whether the intrinsic spatial resolution of the sTGC technology is sufficient to meet the NSW muon momentum resolution specifications. One detector plane of a sTGC quadruplet was read out during the test-beam measurement. Precise reference pion tracks were provided by a silicon pixel telescope detector. Unlike what is measured using cosmic-ray muons, all pions traversed the sTGC gas volume at an incident angle with an angular spread smaller than 10 mrad, limited by the angular coverage of the scintillator detectors used for data acquisition trigger.

5.2.1 Experimental setup

The experimental setup comprised the sTGC module under test, the pixel telescope, the trigger system and readout electronics. A schematic diagram of the experimental setup is shown in Fig. 5.11. The sTGC quadruplet under test was a prototype QS3 module. The module was mounted on a motion table to allow for measurements in multiple locations of the gas volume. The operating voltage was 2.85 kV for all measurements.

The sTGC module was placed between two arms of an EUDET [6] pixel telescope [116]. The telescope consists of six Mimosa [7] planes [117]. Each sensor has an active area of 224 mm^2 with pixels organized in a matrix of 576 rows and 1152 columns with a pitch of 18.4 µm. Each arm consists of three sensors spaced by about 15 cm. The two arms of the

5. Fermi National Accelerator Laboratory
6. European Detector.
7. Minimum Ionizing MOS Active pixel sensor.

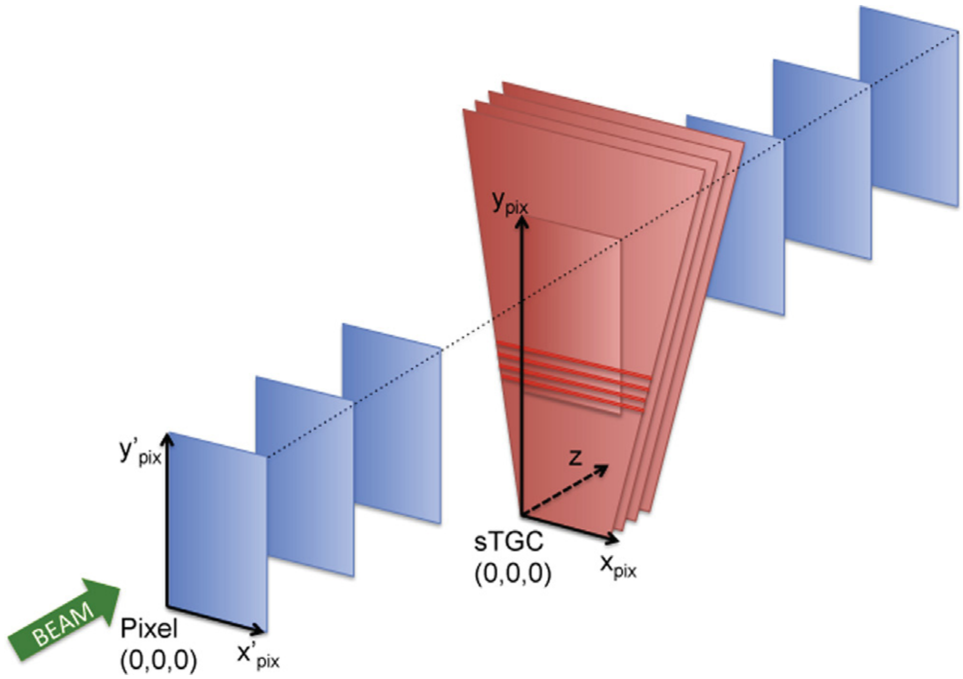

Figure 5.11: Schematic diagram of the experimental setup used for the intrinsic strip spatial resolution measurement with a pion beam. The blue planes indicate the pixel telescope sensor planes. The red trapezoid shapes indicate the sTGC quadruplet gas volumes. The orientation of the sTGC readout strips is shown on the first gas volume. The pixel and sTGC coordinate systems are indicated. The scintillator detectors used for trigger are not shown. The schematic diagram is not to scale.

telescope are spaced by 64 cm. A spatial resolution of approximately 3 μm is expected by combining pion track coordinate measurements from all the telescope sensor planes [118].

Data acquisition trigger was provided by two $1{\times}2$ cm^2 scintillator detectors placed in front and behind the outermost sensor planes of the pixel telescope, overlapping the Mimosa sensors. Coincidences of the scintillator signals were distributed to the telescope and the sTGC readout electronics by a Trigger Logic Unit (TLU). An Arduino microcontroller board [119] controlled the TLU system and synchronized the telescope and sTGC readout systems.

The sTGC strips were read out using the same data acquisition system used for the measurements of Section 5.1. The VMM1 ASIC was configured with a gain of 3.0 mV/fC and an integration time of 25 ns, the same configuration as for cosmic-ray measurements with strip readout. For the test-beam spatial resolution measurement, the x and y coordinates of the reference tracks are provided by the external silicon pixel telescope. Thus, signals from wire channels were not used, unlike for the cosmic-ray measurements.

Two left-handed Cartesian coordinate systems are used for the measurement. A schematic diagram of the two coordinate systems is shown in Fig. 5.11. The first coordinate system is defined with respect to the pixel telescope. The origin of the pixel coordinate system is on the bottom left corner of the first pixel plane. The second coordinate system is defined with respect to the sTGC module. The origin of the sTGC coordinate system in on the bottom left corner of the first gas volume. The axes of both coordinate systems are not exactly parallel due to a potential rotation of the sTGC with respect to the pixel coordinate system in the x-y plane. In the sTGC coordinate system, the z-axis is perpendicular to the surface of the sTGC module and points along the pion flight direction. The x-axis is parallel to the sTGC readout strips and the y-axis is perpendicular to the strips.

5.2.2 Data preparation and track reconstruction

The pixel and sTGC data were recorded independently by separate data acquisition systems. The trigger signal was distributed in parallel to both data acquisition systems. The data acquisition systems incremented an internal counter upon receipt of a trigger signal that generated an event number. The pixel and sTGC datasets were synchronized offline based on the event number.

The sTGC data decoding, data preparation procedure and charge cluster quality cuts used in the analysis of test-beam data are identical to those presented in Sections 5.1.3 and 5.1.4. For this test-beam analysis, in order to obtain a spatial resolution measurement closest to the detector intrinsic resolution, the charge cluster centroid position was reconstructed using the Gaussian fit algorithm. The charge cluster centroid position provides the y-coordinate of the sTGC space points denoted y'_{sTGC} in the following analysis description.

For the reconstruction of pion trajectories using the pixel telescope, a clustering algorithm is used to extract the space point x and y coordinates measured by a sensor based on individual pixel hits. Only events with exactly one space point on each pixel sensor are selected for analysis. A pixel track is then obtained from a straight line least-squares fit of the space points of each sensor. A pixel track quality parameter related to the track fit χ^2 is obtained for each pixel track. A distribution of the quality parameter is shown in Fig. 5.12(a). Tracks having a quality parameter larger than 10 are removed from the dataset to minimize the effects of multiple scattering on the resolution measurement. The effect of changing the track quality parameter cut on the measured spatial resolution is shown in Fig. 5.12(b). As shown in the figure, the spatial resolution decreases with decreasing track quality parameter cut until it reaches a plateau of spatial resolution values statistically consistent with being the same. The chosen cut of 10 for the track quality parameter is located at the end of the plateau where the statistical error on the spatial resolution is a minimum. This quality requirement removes 65% of the reconstructed tracks from the pixel telescope. The pixel track coordinates on the sTGC layer under test are denoted $(x'_{\mathrm{pix}}, y'_{\mathrm{pix}})$.

A total of 2795 pion tracks remain after all sTGC and pixel data quality cuts are applied.

5.2.3 Analysis

A measurement of the intrinsic sTGC detector resolution is obtained by comparing the calculated pion trajectory reconstructed using the external pixel telescope, with the sTGC charge cluster position measurement. The resolution is obtained by fitting the

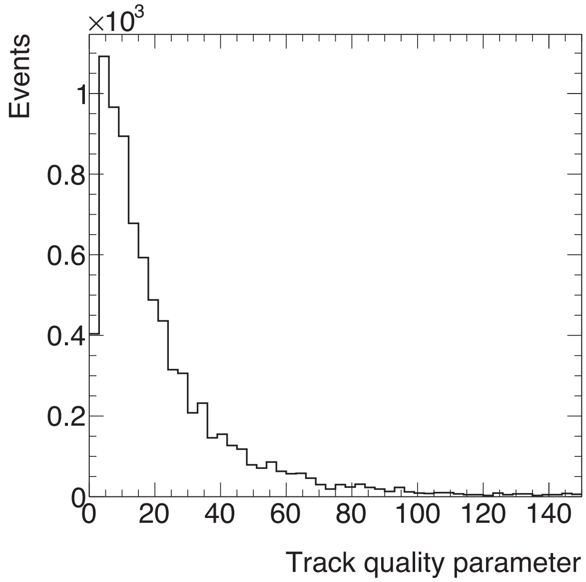

(a)

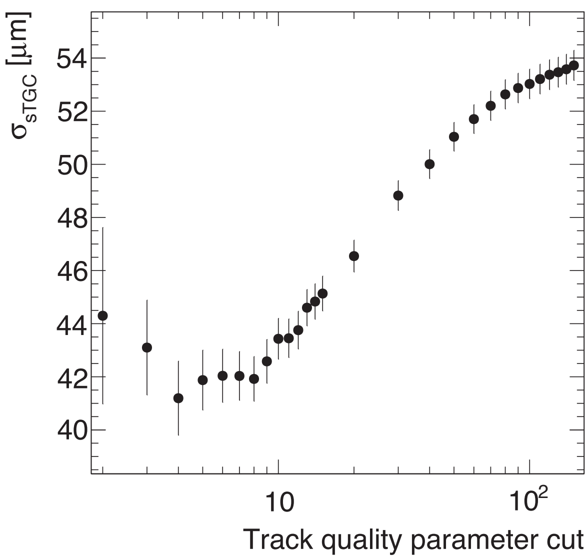

(b)

Figure 5.12: (a) Distribution of the track quality parameter for reconstructed tracks from the pixel telescope. (b) Measured spatial resolution as a function of the cut on the pixel telescope track quality parameter.

residual distribution $y_{\text{sTGC}} - y_{\text{pix}}$, obtained using the corrected sTGC and pixel pion track space points y-coordinate in the sTGC coordinate system, with a Gaussian model discussed later. In this global Gaussian fit, two systematic effects are accounted for: the differential non-linearity bias, and the effect of the misalignments between the pixel and sTGC coordinate systems. The parameters that describe the systematic effects are obtained from the Gaussian fit.

The sTGC measurements y'_{sTGC} are corrected for the differential non-linearity bias using, as was done previously, the sinusoidal function

$$y_{\text{sTGC}} = y'_{\text{sTGC}} - a_m \sin\left(2\pi y^{\text{rel}}_{\text{sTGC}}\right) \tag{5.16}$$

where $y^{\text{rel}}_{\text{sTGC}}$ is the charge cluster centroid position relative to the closest inter-strip gap center of the sTGC layer under test. The variable y_{sTGC} denotes the corrected sTGC measurement. The amplitude parameters a_m for each strip cluster multiplicity m ($m = 3, 4, 5$) are free parameters in the global fit. The values of the amplitude parameters obtained from the global fit to data are shown in Table 5.2. The values of a_m are compatible with being equal for all cluster strip multiplicities m; therefore a single universal amplitude parameter is used in the final global fit to data. The two-dimensional distribution of y-residuals as a function of $y^{\text{rel}}_{\text{sTGC}}$ is shown in Fig. 5.13(a) with the universal differential non-linearity function. The two-dimensional y-residual distribution obtained after correcting for differential non-linearity is found to be reasonably flat as shown in Fig. 5.13(b).

Charge cluster strip multiplicity m	Amplitude parameter a_m [μm]
3	205 ± 9
4	206 ± 4
5	211 ± 5

Table 5.2: Values of amplitude parameters for the differential non-linearity correction obtained from the global fit to data for different charge cluster strip multiplicity.

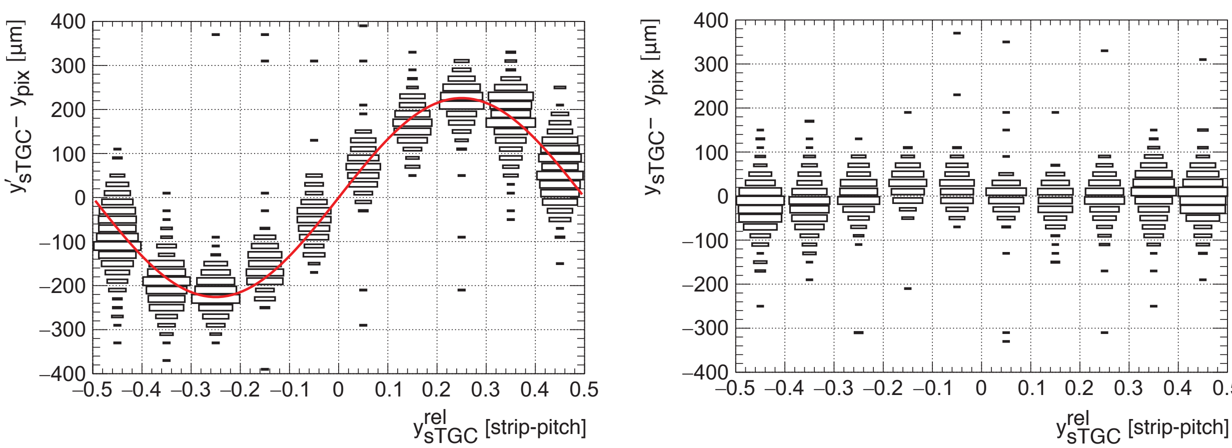

(a) **(b)**

Figure 5.13: Two dimensional distributions of the y-residuals as a function of the the cluster position $y^{\text{rel}}_{\text{sTGC}}$ relative to the inter-strip spacing for a representative data acquisition run. The differential non-linearity correction has been omitted in (a). The red line highlights the universal differential non-linearity correction used for correcting all cluster strip multiplicities. The corrected y-residuals are shown in (b).

The pion track position extrapolated on the tested sTGC layer in the pixel coordinate system is corrected for translation and rotation to obtain the track position in the sTGC coordinate system. The transformation

$$y_{\text{pix}} = -x'_{\text{pix}} \sin\phi + y'_{\text{pix}} \cos\phi + b \tag{5.17}$$

is used to correct for this relative misalignment, where parameters ϕ and b correspond, respectively, to a rotation of the sTGC layer in the x-y plane around the z-axis and to a shift in y. The variable y_{pix} denotes the y-coordinate of the pixel track in the sTGC coordinate system. The two-dimensional distribution of y-residual as a function of x'_{pix} without the alignment correction is shown in Fig. 5.14(a). The alignment correction obtained from the global fit to the data is superimposed over the distribution. The mean of the y-residual increases as a function of x'_{pix} which suggests a misalignment in rotation between the pixel and sTGC coordinate systems. The two-dimensional distribution of y-residuals from the corrected dataset is shown in Fig. 5.14(b). The dependence of the average y-residual as a function of x'_{pix} is removed.

The global model fitted to the data is a double Gaussian function designed to account for both a Gaussian-distributed signal and background components. This Gaussian model is described by the function

$$\begin{aligned} F_m &= F_m(y'_{\text{sTGC}}, y^{\text{rel}}_{\text{sTGC}}, x'_{\text{pix}}, y'_{\text{pix}}; b, \phi, a_m, \sigma_s, f, \sigma_b) \\ &= fG(y_{\text{sTGC}} - y_{\text{pix}}; 0, \sigma_s) + (1-f)G(y_{\text{sTGC}} - y_{\text{pix}}; 0, \sigma_b) \end{aligned} \tag{5.18}$$

where G denotes a normalized Gaussian function. The index m is the charge cluster strip multiplicity. The value of f corresponds to the fraction of tracks that are part of the signal Gaussian distribution of index s. The value of f is equivalent to the expression $A_s/(A_b + A_s)$ when expressed using the Gaussian function amplitudes of Eq. 5.12. The

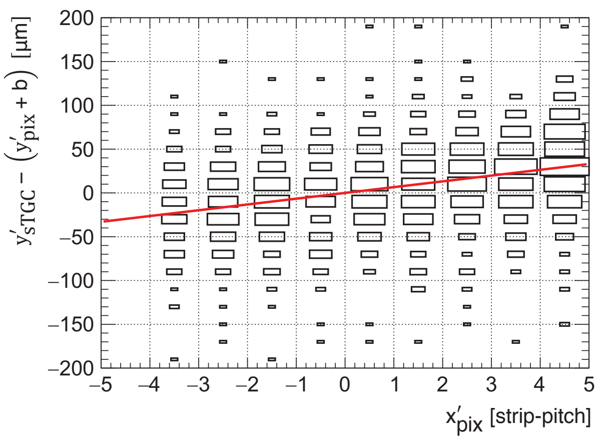

(a)

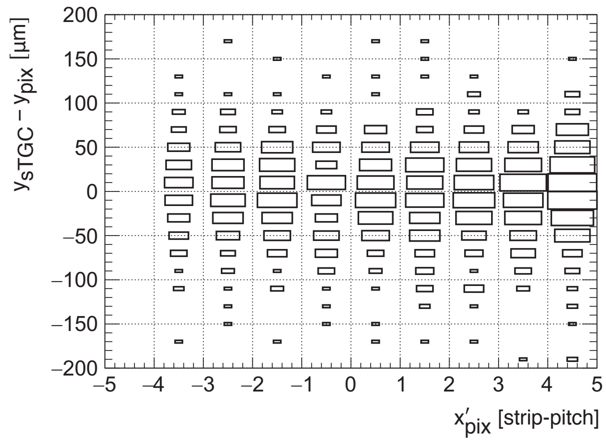

(b)

Figure 5.14: Two-dimensional distributions of y-residuals as a function of x'_{pix} for a representative data acquisition run. The rotation correction (red line) has been omitted in (a) for computing the residuals, whereas the corrected y-residual distribution is shown in (b).

variables ϕ, b and a_m, which were used in Eqs. 5.16 and 5.17 are taken as free parameters of the fit.

5.2.4 Results

The distribution of reference track y-residuals, obtained using the corrected pixel and sTGC space points, is shown in Fig. 5.15. The double Gaussian, whose parameters are obtained from the global fit, is shown as a red line on the distribution. The measured spatial resolution is the width parameter of the signal Gaussian σ_s.

The value of the spatial resolution measured with beam is lower than the σ_0 parameter obtained in a cosmic-ray setup partly because measurements are performed on a very small area (~1 cm^2) of the detector. Thus, the test-beam measurement is less sensitive to variations of construction non-conformities over the detector plane area. Moreover, the differential non-linearity correction applied for the test-beam analysis is specific to the layer under test unlike for the cosmic-ray analysis for which the same correction is ap-

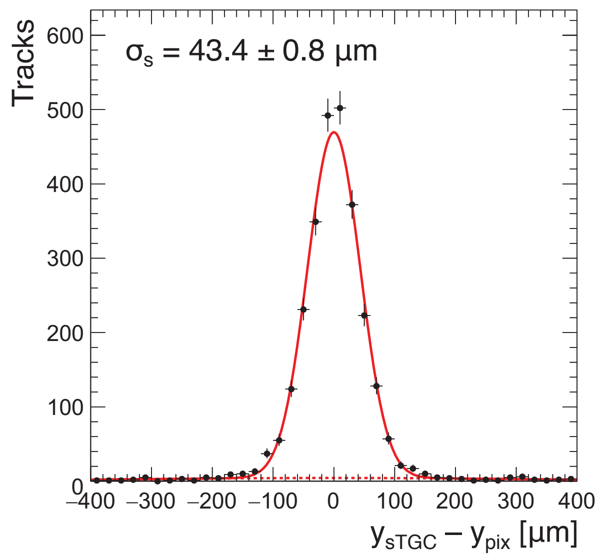

Figure 5.15: Distribution of the reference track y-residual obtained after both differential non-linearity and misalignment corrections are applied. The red line shows the results of the global model fit to the data based on a double Gaussian function. The red dashed line indicates the resulting contribution from the background Gaussian distribution. The value of the fitted σ_s parameter, which corresponds to the width of the signal Gaussian function and interpreted as the spatial resolution, is indicated.

plied to 3 independent detector planes. For cosmic-ray measurements, the differential non-linearity amplitude measured using the corrected space points varies layer-to-layer.

In conclusion, the test-beam measurement provides a value for the spatial resolution that is more independent of the detector construction and the differential non-linearity bias than the cosmic-ray measurements. The impact of these systematic effects can then be studied in dedicated simulation studies such as the one presented in Section 4. An accurate estimation of the offline NSW strip spatial resolution can be obtained by combining the angular dependence parameter $\sigma_{\theta yz}$ obtained with cosmic rays to the accurate intrinsic angular resolution σ_0 obtained in test-beam and using Eq. 5.14. Assuming a perfect construction and alignment of the sTGC detector planes, and assuming that the differential non-linearity is corrected for, an offline strip spatial resolution varying between approximately 60 and 200 μm per individual sTGC detector plane is expected.

5.3 Pads time jitter

The pad electrodes of the sTGC modules installed in the NSW must perform bunch crossing identification of detector hits from muon candidates track segments. This requirement implies that the time jitter, or time spread, of the trigger signal from an NSW module must be within the LHC bunch crossing time of 25 ns. The time jitter of a sTGC detector must therefore be known to validate the use of the sTGC technology for NSW trigger. The sTGC pad time jitter measurement presented in this section is performed by comparing the measured time of a sTGC pad signal with the measured time of a reference plastic scintillator detector. Measurements were carried out at the McGill sTGC Testing Facility, described in Chapter 6, using a full-size sTGC production quadruplet module.

5.3.1 Experimental setup

The sTGC quadruplet under test is a production module of type QS3. A schematic diagram of the experimental setup is shown in Fig. 5.16. The sTGC module is positioned on a tray of the cosmic-ray hodoscope between the scintillator planes h_1 and h_2, located at the top and at the bottom of the hodoscope. One sTGC readout pad located on an outermost layer of the module is read out using the VMM3 ASIC. Strip and wire channels are not used for the time jitter measurements.

The VMM3 is the third prototyping cycle of the ASIC developed to read out the sTGC and Micromegas detectors in the NSW [120]. Compared to the VMM1 ASIC, the VMM3 analog front-end features improved high rate capabilities, enhanced stability for high input charge events, and additional configuration options. The VMM3 has integrated analog-to-digital converters used to digitize the sTGC signal peak and time measurements. A picture of the VMM3 setup used for the measurements is shown in Fig. 5.17. The VMM3 used for the time jitter measurement is fitted on a front-end board that hosts

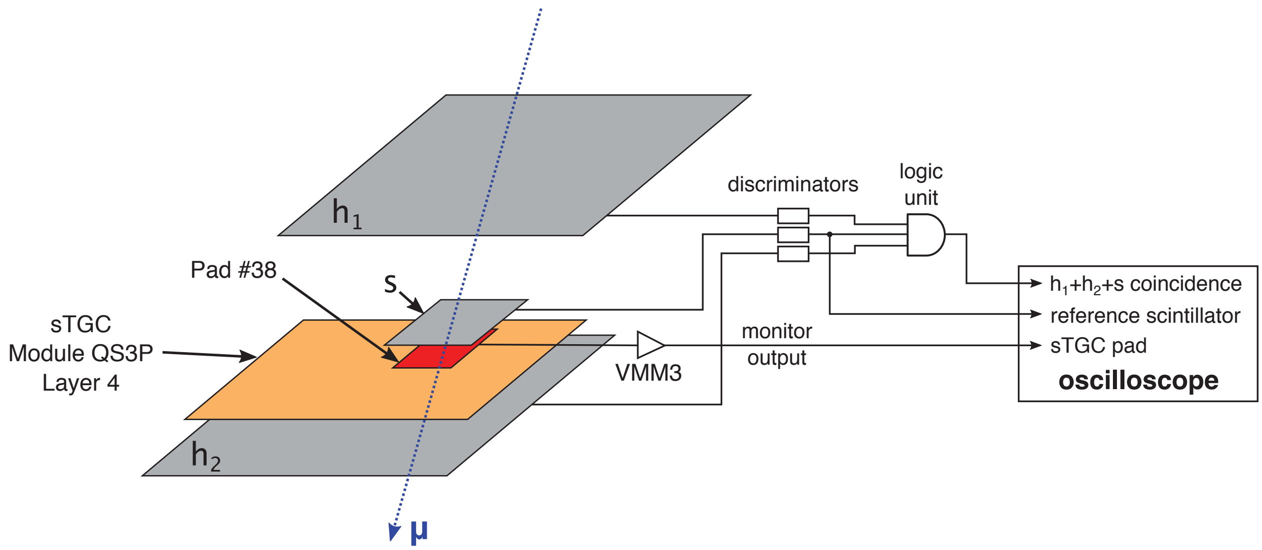

Figure 5.16: Schematic diagram of the experimental setup used for the pad time jitter measurement. The signals from the s, h_1 and h_2 scintillator detectors are processed by discriminators. The coincidence between the three scintillators is provided by a NIM logic unit. Signals from the VMM3 monitor output, the reference scintillator s and the triple coincidence are recorded by the oscilloscope.

a total of three VMM3 ASICs. The configuration and control of the front-end board are performed with a KC-705 board [121] mounted with a custom mezzanine board allowing connectivity to multiple VMM3 front-end boards. The VMM3 can be configured to output the amplified and shaped signal of any readout channel via a so-called "monitor output". The monitor output is routed to an MMCX connector [122] on the front-end board.

During data taking, the VMM3 is configured to output the analog signal of the pad of interest via the monitor output. The VMM3 charge amplifier is configured with a gain of 1.0 mV/fC and the shaper with an integration time of 50 ns.

A small rectangular plastic scintillator detector, named s, of approximate dimensions 5×5 cm^2 is positioned just over the sTGC pad under test. The tested sTGC pad has a trapezoid shape of approximate dimensions 7×35 cm^2. The analog signal of the scintillator detector is processed by a discriminator that outputs a digital NIM logic signal. The scintillator detector s is used to provide a time reference for the pad time jitter measure-

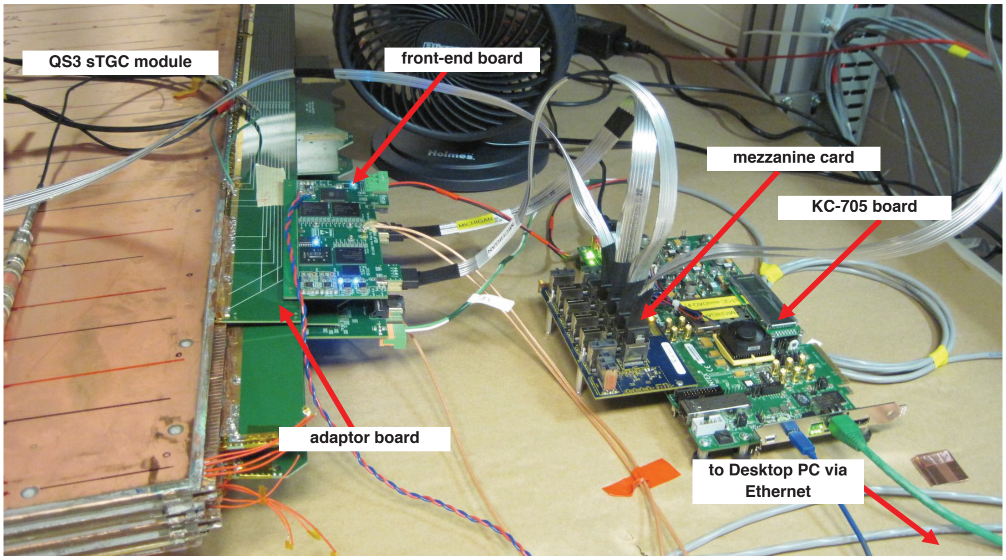

Figure 5.17: Picture of the VMM3 DAQ system used for the pad time jitter measurement. The KC-705 board communicates with a desktop computer via Ethernet for the configuration and control of the DAQ system. The mezzanine card provides the necessary connectivity between the front-end board and the KC-705 board. The adaptor board is soldered to the QS3 sTGC module and provides the connectivity between the front-end board and the sTGC pad readout channel under test.

ment. The time resolution of the scintillator detector s is approximately 2 ns RMS.

The time resolution of the scintillator detector s was obtained by fitting a Gaussian function to the distribution of the time difference between the coincident hits of the scintillator detector s and another scintillator detector of similar size when exposed to cosmic-ray muons. The time difference distribution and the fitted Gaussian function are shown in Fig. 5.18. Assuming that both scintillator detectors have a similar time resolution, the time resolution of the scintillator detector s is obtained by dividing the width of the fitted Gaussian function by $\sqrt{2}$.

The pad analog signal and the digital signal of the scintillator detector s are connected to the channels of a Keysight MSOX4054A oscilloscope. The oscilloscope is configured to trigger on the triple coincidence between the discriminated signals of the s, h_1 and h_2 scintillator detectors. The triple coincidence is processed by a CAEN N405 NIM logic

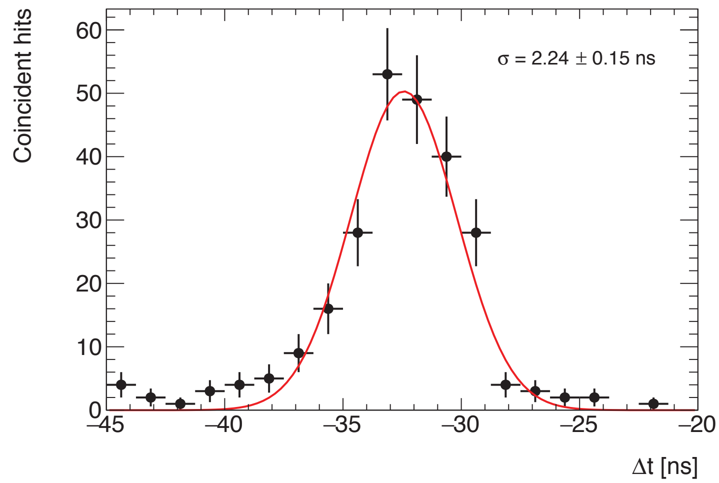

Figure 5.18: Time difference between the coincident hits of the scintillator detector s and another reference sintillator detector of similar size. The Gaussian function fitted to the distribution is shown as a red line. The horizontal axis of the plot has an arbitrary offset.

unit. A representative oscilloscope segment for one cosmic-ray muon event is shown in Fig. 5.19.

5.3.2 Analysis

An oscilloscope segment is recorded upon the receipt of a trigger signal. Approximately 1000 oscilloscope segments were recorded and analysised offline. Oscilloscope segments are selected for analysis if the pad pulse peak value is above a predefined software threshold of 20 mV. The sTGC pad time measurement, denoted t_{sTGC}, is defined as the software threshold crossing time of the sTGC analog signal. The reference scintillator detector time measurement, denoted t_s, is defined as the time at which the digital signal is at half-way between the “low” and “high” TTL digital voltage levels which is at approximately 1.5 V.

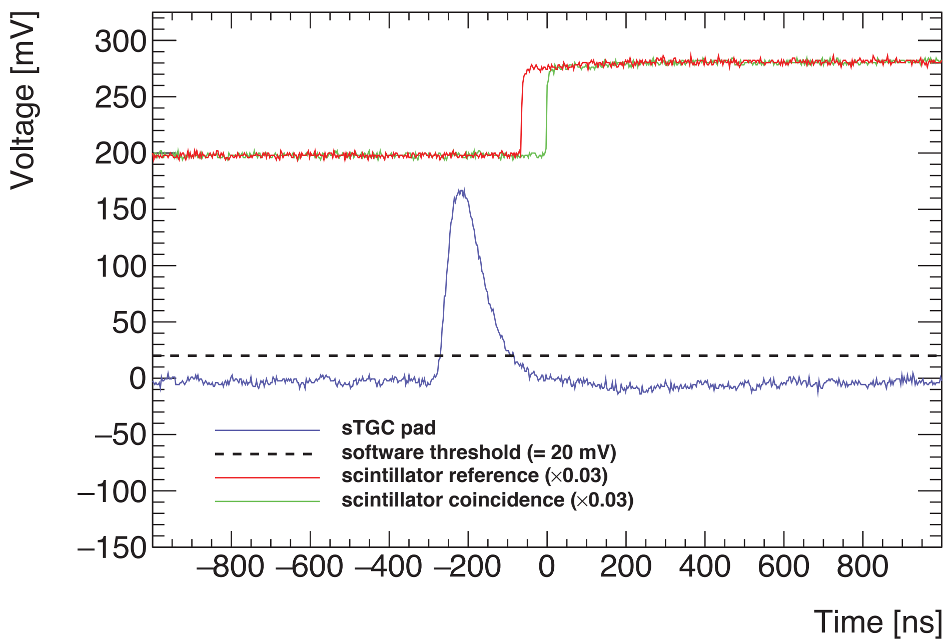

Figure 5.19: Oscilloscope segment of a representative pad analog signal from a cosmic-ray muon amplified and shaped by the VMM3 ASIC. The scintillator detector reference and coincidence signals are digital TTL logic pulses. The digital pulses are scaled by a factor $\times 0.03$ and offset on the voltage scale for display purposes. The origin of the time axis is the leading edge of the scintillator detector coincidence pulse, which triggers the oscilloscope. The sTGC pulse time measurement is taken as the time when the pulse leading edge crosses the offline software threshold. The reference scintillator detector time measurement is taken as the leading edge of the scintillator detector discriminated pulse (red line).

5.3.3 Results

One of the main tasks of the sTGC pads in the NSW is the bunch crossing identification of detector hits. For a single detector plane, this requirement implies that, following the passage of a muon, the sTGC pad signal is recorded within a time-windows equal to the LHC bunch crossing time of 25 ns. Thus, the chosen metric used to quantify the sTGC pad timing performance is the “bunch crossing identification efficiency” (BCID efficiency), defined as the fraction of pad hits falling within an optimal 25 ns time-windows.

The distribution of time differences $t_{\text{sTGC}} - t_s$ between the pad and the reference scintillator detector signals for an operating voltage of 3.0 kV is shown in Fig. 5.20(a). The optimal 25 ns time-window within which a maximum number of pad signals falls is shown as two vertical blue solid lines. The BCID efficiency that corresponds to this time-window is 57 $\pm$ 1 %. The tail of the time difference distribution is due to tracks falling in the low field regions between two anode wires [33].

The measured BCID efficiency as a function of operating voltage is shown in Fig. 5.20(b). The time jitter improves as a function of increasing operating voltage due to the corresponding increase in gas gain, lowering the primary ionization threshold in the critical region, and lowering the drift time of primary ionization electrons. An increase of the operating voltage must, however, be carefully considered as it could lead to an accelerated detector ageing due to the increase in charge production in the gas volume.

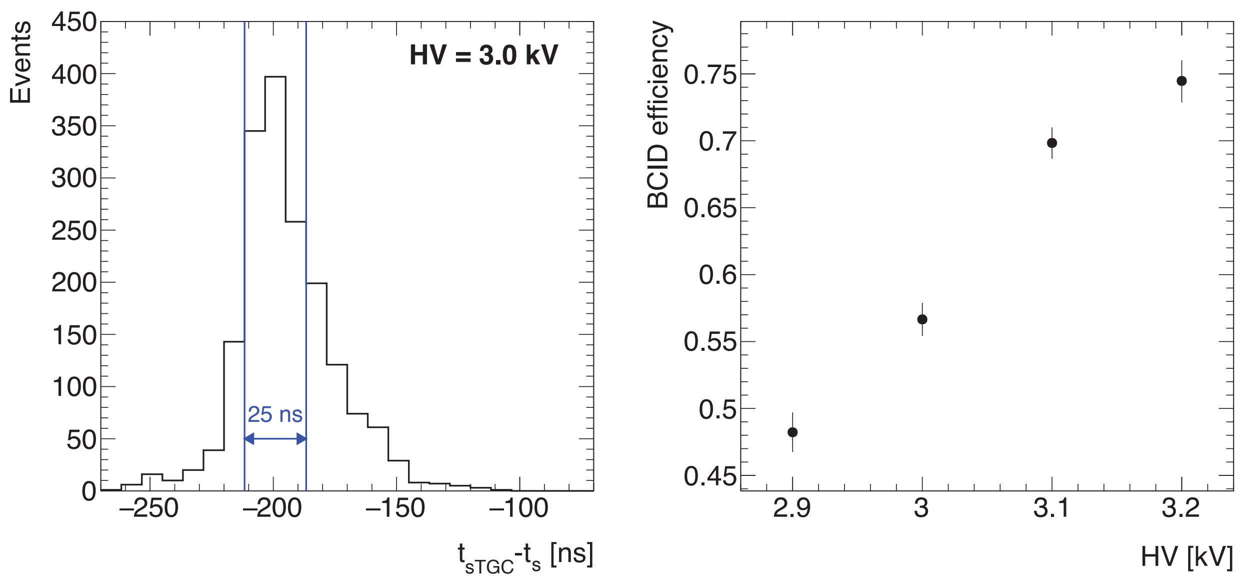

(a) **(b)**

Figure 5.20: (a) Pad time jitter at an operating voltage of 3.0 kV and (b) fraction of hits contained in an optimal 25 ns time-window as a function of the operating voltage. The optimal 25 ns time-window, used to calculate the BCID efficiency, is highlighted with blue lines on the (a) distribution.

The measured BCID efficiency shows that a single sTGC detector plane cannot provide an accurate bunch crossing identification of sTGC hits even when operating with a voltage higher than the nominal value of 2.9 kV. The NSW sTGC modules are, however, made up of 4 independent detector planes with staggered anode wires. Given this anode wire configuration, a muon is not expected to traverse the low electric field regions of all four gas volumes of a module. Moreover, the current foreseen requirement for the NSW trigger is a pad hit from 3-out-of-4 detector planes. Therefore, the time jitter for the combined four detector planes of a quadruplet is anticipated to be significantly better.

Sophistications of the trigger algorithms are also foreseen if the trigger efficiency of a sTGC module is not sufficient. For example, a sliding time-window algorithm could be used for triggering to match pad hits from multiple bunch crossings rather than just one. Such a sliding time-window algorithm could relax the pad time jitter requirement from one bunch crossing time to more than one.

Additionally, the time jitter of sTGC pads is expected to vary as a function of different parameters of the readout electronics configuration. For example, the VMM3 integration time is expected to have an impact on the time jitter because it relates to the slope of the leading edge of VMM3 analog pulses. The time resolution for a system with constant voltage discrimination such as the VMM3 is typically inversely proportional to the slope of the analog pulse leading edge [52].

In conclusion, the optimal trigger algorithm and electronics configuration required to fulfil the NSW time jitter specifications have yet to be defined. Nevertheless, the measurements presented here define a necessary baseline for the upcoming hardware integration work carried-out for the NSW.

5.4 Summary of performance measurements

Measurements of the strip intrinsic spatial resolution and pad time jitter were carried out to confirm whether the sTGC technology meets the NSW performance specifications.

The NSW trigger algorithm will use the WA algorithm for charge cluster centroid finding [97]. Furthermore, the angular coverage of the NSW in the bending plane, perpendicular to the strips, is between 0.12 and 0.56 rad. Therefore, based on cosmic-ray measurements using the WA algorithm, the expected spatial resolution will range between 210 and 280 µm, which, as demonstrated in the simulation studies of Chapter 4, is sufficient to deliver an online spatial resolution of 1 mrad.

For offline analysis, more computationally expensive algorithms with a performance at least as good as the GF algorithm will be used for cluster centroid finding. Cosmic-ray measurements showed that the value of the $\sigma_{\theta_{yz}}$ parameter, which describes the degradation of spatial resolution with the angle of incidence, is 305 ± 4 µm. For perpendicular tracks, the intrinsic spatial resolution $\sigma_0 = 43.4 \pm 0.8$ µm was measured in a test-beam setup. Based on the combined cosmic-ray and test-beam results, an intrinsic strip spatial resolution varying between approximately 60 and 200 µm is expected from individual NSW sTGC detector planes. When combined into quadruplets, the sTGC modules will deliver a spatial resolution comparable to that of the current MDT modules which is 35 µm [8]. This figure assumes, however, a perfect detector construction and module alignment. The track reconstruction performance of the NSW will ultimately surpass that of the current muon end-cap inner station when sTGC and Micromegas offline space-points are combined.

8. The spatial resolution for a combination of N detector planes is a fraction $1/\sqrt{N}$ of the spatial resolution of a single plane. Thus, the spatial resolution of a sTGC module that measures 4 space points is expected to be half that of a single detector plane.

Finally, the sTGC pad BCID efficiency in a 25 ns time-window was measured and varies between approximately 50% and 75% for operating voltages between 2.9 and 3.2 kV. The pad time jitter for a single sTGC detector plane is not sufficient to deliver an accurate bunch crossing identification. Integration work is ongoing to optimize the detector and readout electronics running parameters as well as to define a trigger algorithm that could work around this modest BCID efficiency.

6

Quality control of sTGC modules using cosmic rays

The sTGC modules manufactured for the New Small Wheel (NSW) follow a stringent set of Quality Assurance (QA) procedures and Quality Control (QC) tests during manufacturing and after they have been constructed [123]. Modules satisfying the QC tests are expected to meet the track reconstruction performance and longevity standards defined by the NSW specifications.

The sTGC production for the NSW is divided into 5 production lines, each located in a different country and responsible for manufacturing one or two modules types [124]. The different steps of manufacturing and quality control are shared between different institutes that make up a production line [1]. The production lines follow a common manufacturing and quality control procedure, which is summarized in this section.

As part of the QC tests developed for sTGC manufacturing, a data acquisition is performed with the finished sTGC modules during an exposure to cosmic rays. A set of performance metrics that characterize the detector response to ionizing radiation are measured using cosmic-ray data. A set of candidate performance metrics to be considered during detector production is explored in this chapter.

The chapter is arranged as follow. A summary of the QC tests performed during the manufacturing of sTGC modules is given in Section 6.1. The McGill sTGC Testing Facility, a laboratory commissioned for the cosmic-ray testing of sTGC modules assembled in Canada, is described in Section 6.2. The analysis techniques used for the measurement

1. The sTGC construction sites are PUC (Chile), Shandong (China), TRIUMF, Carleton and McGill (Canada), Technion, TAU and Weizmann (Israel), and PNPI (Russia).

of the cosmic-ray performance metrics as well as proof-of-concept measurements using a small-size prototype sTGC module are presented in Section 6.3. A summary of the performance metrics proof-of-concept measurements is presented in Section 6.4.

6.1 Quality control of sTGC modules

The Quality Control (QC) of a sTGC module starts with the testing of individual components prior to assembly. First, as described in Chapter 4, non-conformities of the pad and strip cathode boards electrode patterns are measured using a CNC router. In addition, the thickness of the detector frames, glued on the sides of the gas volumes, structural supports and cathode boards are measured at multiple locations to control the variations of the gas volumes thickness. Gas volume thickness variations could result in unacceptable gas gain variations over the detector area and systematic shifts in the reconstructed muon track space points. Finally, the uniformity of the graphite coating sheet resistance, after being sprayed on the cathode boards, is checked to ensure that the width of the charge induction on the readout electrodes is uniform and to keep the charge cluster strip multiplicity below 5, as expected by the NSW trigger processor. Furthermore, a high graphite sheet resistance may give rise to inefficiencies in the detector when operating at high particle fluxes by lowering the effective operating voltage because of ohmic effects as described in Section 2.4.5.

Quality control tests are also performed at every assembly step of a sTGC module. First, the gas tightness of individual detector planes is checked after the gluing of the detector frames and cathode boards into a gas volume. The thickness uniformity of the detector planes is measured to check the effects of gas volume gluing on the planarity of the detector planes. The gain variations of the detector planes are directly measured with an x-ray scan. The test consists of measuring the current drawn by an operating detector plane while varying the position of a collimated x-ray beam on the surface of the detector plane. The x-ray intensity is kept constant during the test and, therefore, the current drawn by the detector is proportional to the gas gain. Regions of the detector plane having an anomalous gas gain (either too small or too large) can indicate construction defects. The test also provides a measure of the level of leakage current which can indicate potential defects in the dielectric materials of a detector plane or in the soldered signal and ground connections.

As described in Section 4.3.1, individual detector planes are first glued into doublets. Then, doublets are glued into quadruplets. Paper honeycombs are placed between the detector planes for spacing and to provide additional rigidity. The thickness uniformity of the doublet and quadruplet assemblies is measured to check for potential gluing defects. The strip alignment between the four detector planes of a sTGC module is measured using a microscope and a quantitative image analysis software. Adaptor boards, which consist of Printed Circuit Boards (PCB) having the necessary circuitry for connecting the VMM3 Front-End Boards (FEBs), are soldered to the readout channels of the detector planes. The readout channels connectivity is checked by a pulser test, which consists of injecting voltage pulses in the operating voltage input line of a detector plane and reading out the induced voltage on each individual channel via the FEB connector of the adaptor boards using custom electronics.

The response of sTGC modules to ionizing radiation is ultimately tested using cosmic rays. The sTGC module must be operational and fully instrumented with readout electronics during cosmic-ray testing. Data acquisition is triggered on the passage of a cosmic ray by using hits from plastic scintillator detectors. The duration of cosmic-ray data taking is foreseen to be approximately a couple of days. The data taking time has a direct impact on the statistical error on the value of the cosmic-ray performance metrics. The sources of uncertainties on the measurement of the cosmic-ray performance metrics are discussed in Section 6.3.

Performance metrics are obtained from the analysis of cosmic-ray data. The performance metrics considered in this chapter are

- the hit efficiency,
- the strip spatial resolution,
- the strip pattern misalignments between layers and
- the gas gain uniformity.

Values of the performance metrics are obtained for each individual detector plane of a small-size prototype module and as a function of position over the area of the detector planes. The hit efficiency and gas gain uniformity measurements are performed for the strip, pad and wire electrodes of the tested module. The spatial resolution and layer misalignments measurements are only performed for the strip electrodes because they are used for precision track reconstruction.

Cosmic-ray testing is a good complement to other tests performed as part of the QC procedure. For example, the hit efficiency measurement determines if the signal to noise ratio of the readout channels is sufficient to detect MIPs, a measurement which cannot be done with the pulser test. A large detector noise can indicate issues with grounding or detector shielding. Cosmic-ray misalignment measurements are sensitive to inter-layer misalignments inside the detector plane, unlike the microscope measurements which can only access the sides of a module. The gain measurement with cosmic rays is expected to provide a more detailed description of the detector response than x-ray measurements because a distribution of the charge production rather than the mean current is measured. The cosmic-ray gas gain measurement also combines the effects of the detector capacitance, capacitive coupling between channels and readout electronics response. Furthermore, the cosmic-ray gas gain measurements are more representative of the detector response to muons because the most probable charge deposition of x-ray radiation is large compared to that of MIPs.

6.1.1 Cosmic-ray testing requirements

The detector QC tests are defined such that the manufactured sTGC modules meet the NSW performance requirements with respect to the trigger efficiency and muon track reconstruction. In addition, the QC tests allow one to identify non-uniformities in the detector construction which could help identify issues with the manufacturing of a module and lead to its rejection.

Trigger efficiency

The current Level-1 trigger efficiency of the ATLAS muon spectrometer for single muons at $p_T > 25$ GeV in the end-cap regions has a plateau at 85% [94]. The trigger efficiency is required to be at least equal to or better than the current efficiency following the NSW installation. Simulation studies of the NSW trigger algorithm have shown that, assuming a hit efficiency of 95% for strip and pad electrodes, the Level-1 trigger efficiency averages at 89% [93]. Simulation studies did not, however, account for structural supports which cover approximately 5% of the detector planes. As shown in Appendix A (Section A.2), a degradation of the hit efficiency of the detector planes results in a lower NSW trigger efficiency. Therefore, based on the simulation studies, the results of Section A.2 and accounting for the structural supports in the sTGC gas volume, a hit efficiency of at least 98% over the sensitive areas of the sTGC detector planes is required to meet the NSW performance goals.

Spatial resolution

Simulation studies of Chapter 4 and the experimental measurements of Chapter 5 show that the online sTGC strip spatial resolution meets the performance requirements of the NSW trigger algorithm even if increased by a factor of 2. The focus of the cosmic-ray strip spatial resolution measurement presented later is on a demonstration of the ability to measure the uniformity of the resolution. Isolated regions of a detector plane that present an anomalous spatial resolution could also indicate a detector defect.

Detector plane alignment

Layer misalignments are closely related to the effective spatial resolution of a module because they create systematic shifts of the muon track space points which increases the Root Mean Square (RMS) of the muon track residuals[2]. Thus, to avoid biases in the reconstruction, the typical shift of the strip pattern should be, at most, of the order of the intrinsic spatial resolution. Two-dimensional distributions of y-residuals, presented later, are used as a way to identify such misalignments or even issues that occurred during the detector gluing process. The measurements of inter-layer misalignments with cosmic rays are also valuable for the offline analysis of hits from the NSW and during detector operation.

Gain uniformity

Cosmic-ray data may be used to measure the gain uniformity of each chamber. Although sTGC module acceptance criteria will not rely on this kind of measurement, the ability to measure the gain uniformity of a chamber is a useful complementary tool to understand the characteristics of a sTGC module that may not behave as expected, or one that nearly misses the acceptance criteria. Given the tight timescale of the NSW construction project, imperfect modules may need to be used in the construction of the NSW, and understanding their behaviour will be important.

2. RMS $= \sqrt{\mu^2 + \sigma^2}$

6.2 The Canadian sTGC Testing Facility

The McGill sTGC Testing Facility, located in Montréal (Canada), was commissioned for testing the NSW sTGC modules assembled in Canada [125]. A total of 60 sTGC modules will be tested at the facility over a period of approximately 18 months. Module testing has started in June 2018 at the facility.

The facility consists of a gas system, which provides the necessary n-pentane/CO_2 gas mixture for operating sTGC modules, and of a cosmic-ray hodoscope. Both systems are described later in the section.

The operating high voltage (HV) for the sTGC modules and low voltage (LV) for the readout electronics are delivered by a CAEN power supply crate [3] that hosts HV [4] and LV [5] cards. Each tested detector plane is connected to an individual HV channel. The HV and LV channels are monitored by the slow control system [125]. The HV supply is automatically shut down, or tripped, by the power supply if the HV current exceeds a programmable trip current in order to avoid potential damage to the detectors. The trip current is set to 1 μA during cosmic-ray data taking. The typical current during cosmic-ray data taking is lower than 1 nA [6].

The VMM3 DAQ system described in Section 5.3.1 is used for the cosmic-ray testing of production NSW modules. The proof-of-concept measurements shown later in Section 6.3 were, however, carried out using the first DAQ prototype system of the testing facility described in Section 5.1.1.

3. CAEN SY4527
4. CAEN A1535D
5. CAEN A2519
6. Currents of up to a few mA are expected during operations at a high rate with sTGC detectors. This current level would, however, indicate an issue with the detector during cosmic-ray testing.

6.2.1 Gas system

The Testing Facility gas system is designed to provide an n-pentane/CO_2 gas mixture in the ratio 45:55 or pure CO_2 to the tested sTGC modules. A full description of the McGill Testing Facility gas system is given in [125]. The gas system can support up to 10 independent gas channels, each designed to deliver the gas mixture to an individual sTGC module. The gas volumes of an sTGC module can be daisy-chained to deliver the gas mixture to all detector planes using a single gas line. The gas system is monitored and controlled by a slow-control system which allows for a safe and continuous operation of the gas system even in the absence of an operator.

The CO_2 supply of the gas system is provided by a gas cylinder. The CO_2 pressure at the output of the cylinder is controlled by a two-stage regulator set. The initial CO_2 flow is set using a mass flow controller. The n-pentane is initially liquid and contained in an airtight mixing vessel kept at room temperature. The n-pentane/CO_2 mixture is obtained by flowing CO_2 into the mixing vessel through a dip tube going under the n-pentane level. The CO_2 gas is diffused in the n-pentane using bubbling stones. The room temperature gas mixture then flows through a condenser and is cooled down to a preset temperature using a Peltier cooler. The n-pentane ratio of the mixture is lowered by condensation until the saturation level is reached. The gas mixture then flows into a manifold that divides the flow into one or more gas channels connected to the sTGC modules. The gas flow of each individual gas channel is controlled by a rotameter equipped with a needle valve. The gas flow of the gas channels downstream from the sTGC modules is collected by a manifold and directed to a recovery system. The recovery system, which consists of a condenser and a cold airtight vessel placed inside a flammable-gas fridge, collects some fraction of the n-pentane in the mixture by condensation. Finally, the remaining gas mixture is exhausted via the building vent to the outside.

The procedure through which the gas mixture is delivered to a sTGC module in preparation for cosmic-ray data taking is the following. First, the gas volumes of the tested sTGC module are purged with pure CO_2 gas. The CO_2 purge is performed as a safety measure to remove traces of oxygen and any other potential impurities. The initial purging is done at a flow rate of 100 ml/min. Then, sTGC modules are flushed with the n-pentane/CO_2 mixture at a rate of 40 mL/min. The purging operations are performed until the gas composition of the gas volumes is considered stable which occurs after flowing approximately the equivalent of twice the volume of the gas gaps. Thus, the duration of gas purging is typically a couple of hours and depends on the detector size and the flow rate. During cosmic-ray operations, the flow rate of the n-pentane/CO_2 mixture is reduced to 10 mL/min. The operating mixture must be replenished during data taking because of the degradation of the n-pentane molecules during detector operation. Micro-leaks can also be a source of contaminants [46] in the gas volumes. Gas contaminants, if present in large quantity, can prevent a stable operation of the sTGC modules [62]. After cosmic-ray operations, pure CO_2 is flowed at a rate of 100 mL/min to purge any residual n-pentane from the gas volumes. The n-pentane gas must be removed when the module is not used to avoid potential n-pentane condensation which could damage the resistive graphite coating and other internal components of the gas volumes.

6.2.2 Cosmic-ray hodoscope

The cosmic-ray hodoscope consists of an extruded aluminum structure having the overall dimensions 2.6 m $\times$ 2.6 m $\times$ 2.2 m (height). The hodoscope has four drawers placed at equal vertical spacings. Each drawer can hold a QS3 sized sTGC module in a horizontal position. A drawing of the structure design is shown in Fig. 6.1.

The hodoscope has two layers of plastic scintillator detectors located over and under the structure. Each scintillator detector layer is made of four adjacent 1.6 m $\times$ 0.65 m scintillator slabs of 2.5 cm in thickness. A waveguide is glued at each end of the slabs to di-

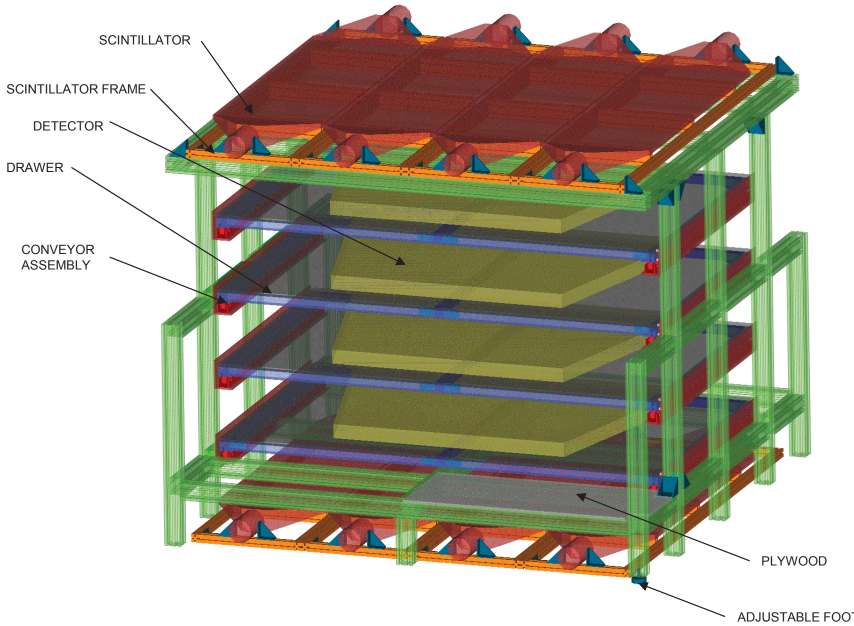

Figure 6.1: Schematic of the cosmic-ray hodoscope. The extruded aluminum parts are coloured green and orange. The assemblies of scintillators, waveguides and PMTs are coloured red and are located over and under the structure. The flat trapezoid sTGC modules are coloured olive and are located over the blue drawers where they are partially seen.

rect the scintillation light to photomultiplier tubes (PMTs) [7]. The PMTs are powered with a negative voltage of approximately 1.6 kV provided by the power supply mainframe and controlled by the slow-control system. The signal output by the PMTs is transmitted to the hodoscope trigger system.

The hodoscope trigger system processes hits from the scintillators and issues trigger signals to the sTGC readout electronics. The readout electronics start data acquisition upon receipt of a trigger signal. The trigger signals are issued in the event of hits on any PMT of the top scintillator layer in coincidence with hits from any PMT of the bottom scintillator layer. The trigger system also counts the number of trigger signals issued and the elapsed data taking time. The trigger system is manually started and stopped using push-buttons on a gate generator module.

7. Hamamatsu H6410.

The trigger system fans out the trigger signals to the sTGC readout electronics using independent signal lines. The width of the trigger pulses and the delay between pulses is set to 1 µs and 6 µs respectively. The timing parameters are tuned as to mitigate the probability of desynchronization of the CDAQ boards due to reflections in the signal lines. The trigger system consists of a set of NIM modules sharing a common crate. The signal transmission between modules and to the CDAQ boards is done using LEMO cables.

A block diagram of the trigger processor is shown in Fig. 6.2. The signal processing algorithm is the following. Signals from the PMTs are transmitted to a CAEN N843 constant fraction discriminator module. The discriminated digital signals of the top and bottom PMTs are then transmitted to independent logic `OR` units of a CAEN N113 module. The signals from the `OR` logic units are transmitted to one unit of a CAEN N405 logic module configured in the `AND` logic gate mode. One output of the `AND` logic gate is transmitted to a CAEN 2255B gate generator configured to output 1 µs wide pulses. The gate generator output is transmitted to a CAEN N625 fan-out module which divides the signal into up to 4 independent lines. The fan-out module outputs signals having NIM logic levels. Since TTL levels are required by the CDAQ boards, the signal is converted from NIM to TTL using a CAEN N89 module before being transmitted. The second output of the `AND` logic gate is transmitted to another unit of the CAEN N625 fan-out module which divides the signal into two signal lines. The first line is transmitted to a LeCroy 222 gate generator configured to output 6 µs wide pulses. The pulse is used to veto the `AND` logic gate. The other output of the fan-out module is transmitted to the input of the counting unit of a CAEN N1145 scaler module.

The trigger system is started and stopped using the push-buttons of a gate generator unit of a LeCroy 222 module configured in latch mode. The latch signal is transmitted to one of the inputs of the `AND` logic gate. The latch signal is also transmitted to the `LOAD` input of the CAEN N1145 scaler. The built-in timer of the scaler is started upon receipt of the `LOAD` signal. The scaler outputs a `END MARKER` signal when the timer ends. The `END MARKER` signal restarts the counter provided the latch is still activated. The number of `END MARKER` signals issued is counted by another counting unit of the scaler. The timer counting time is set to 10.003 ms. The counting time is tuned using an oscilloscope such that the `END MARKER` signal is output at exactly every 10 ms when accounting for wire and internal module delays. Thus, the `END MARKER` count provides the elapsed data taking time in hundredths of a second.

The gate of the scaler counting units is the latch signal. Therefore, the counting of time and of the number of trigger signals are stopped immediately when pressing the latch stop push-button.

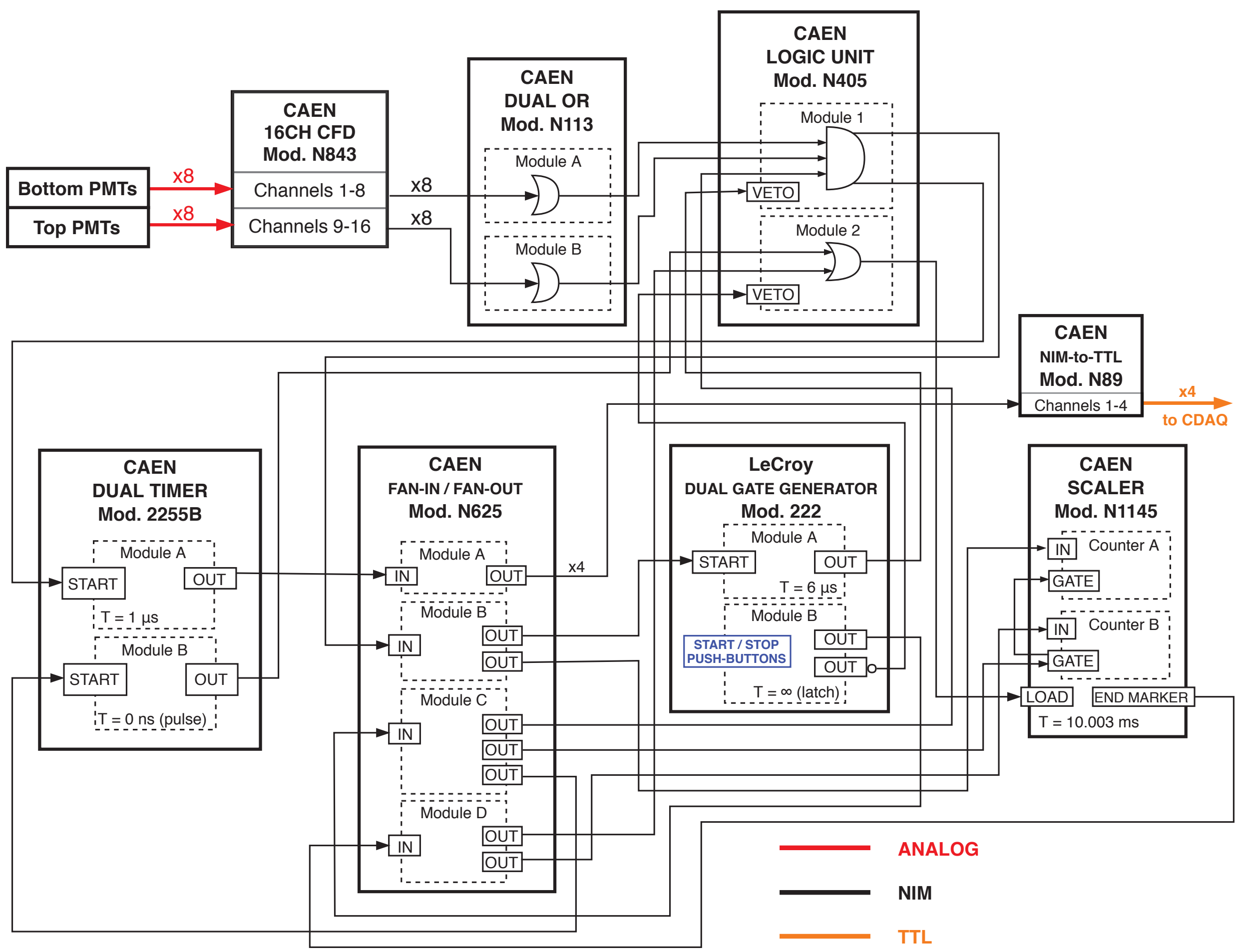

Figure 6.2: Block diagram of the cosmic-ray hodoscope trigger system. The bold rectangles indicate individual NIM modules. The arrows indicate the direction of the signal. The colour of the arrows is associated with the logic levels of the signal lines. The CAEN N89 NIM-to-TTL module is used only for the CDAQ prototype boards which require TTL levels. More than 4 independent trigger lines can be used if additional fan-out modules are daisy-chained to the first one.

6.3 Cosmic-ray quality control testing

As part of cosmic-ray QC testing, the cosmic-ray data are first analyzed using the procedure for data preparation, space point measurement and muon track reconstruction described in Section 5.1. Then, specific algorithms used to extract the performance metrics are applied. For all tested performance metrics, a reference muon track is required to match the measurements to a particular region, or measurement bin, of the tested layer. The 4 detector planes of a tested sTGC module are considered as being independent detector units during testing. Thus, instead of using an external tracker, the reference muon track used for testing a given detector plane is obtained in-situ using hits from the other detector planes of the tested module. Inclusive and exclusive reference muon tracks, which include or exclude the detector plane under test, are used for cosmic-ray testing.

Measurements of each performance metric are reported in two-dimension over the area of the detector plane. The dimensions of the two-dimensional bins are chosen to achieve the smallest systematic and statistical errors on the measurements. For the cosmic-ray testing of mass produced sTGC modules, a fixed size binning will be used to allow a one-to-one comparison between sTGC modules tested.

The proof-of-concept measurements of the cosmic-ray performance metrics considered (trigger efficiency, spatial resolution, inter-layer misalignment, gain uniformity) were obtained using data from the 40×60 cm^2 sTGC prototype and the VMM1 DAQ, both described in Chapter 5. The measurements were carried out at the McGill sTGC Testing Facility. The performance metrics that are shown were computed using data from different data acquisition runs of varying data taking time. The exact data taking time and number of muon tracks used for the measurement will be specified in the text.

6.3.1 Hit efficiency

The hit efficiency of a detector plane is defined as the fraction of exclusively reconstructed reference muon tracks matched with a hit anywhere on the tested detector plane. Reference tracks that consist of at least 3 wire and 2 strip space points are used for the efficiency measurement. The wire readout electrodes consist of relatively wide wire groups that are half staggered from one detector plane to another. Using hits from at least 3 different planes prevents the reference wire track from being made up of only two wire group which could potentially be aligned, thereby cancelling the positive effects of staggering on the wire track resolution. The resolution of exclusively reconstructed tracks using wire hits is discussed in Appendix C. The resolution on the y-coordinate, provided by the strips, is much better than the resolution on the x-coordinate and, therefore, hits from two layers of strips are sufficient. The finite spatial resolution of the reference track is a systematic effect which is discussed later in the text. Hits from strip, wire and pad readout channels of the tested layer are processed independently to obtain a value for the hit efficiency of each individual electrode type. Analysis cuts are not applied on the tested layer to factor the effects of the analysis cut efficiency on the measured hit efficiency. The calculated position of the reference track on the tested layer is used to define in which bin the measurement lies.

Results

Efficiency maps for strip, wire and pad electrodes are shown in Fig. 6.3. The dataset used for the efficiency maps required 22 hours of data taking for strips (3.2×10^5 reference tracks), 50 hours for wires (6.1×10^5 reference tracks) and 23 hours for pads (3.3×10^5 reference tracks). The bin size was chosen to be (36 mm $\times$ 6.4 mm) in the coordinates (x, y) aiming for an absolute statistical error better than 1% and a binning identification accuracy of at least 95% in both the x and y coordinates. The bins are larger in x because the spatial resolution of the wire reference tracks is much larger than that of the strip reference tracks. The bin identification accuracy is discussed in Appendix D and the statistical and systematic errors are discussed later in the text. White bins were matched with a number of exclusive tracks lower than a predefined threshold. The threshold is set to 50 reference tracks for the efficiency maps shown which corresponds to a statistical error of 10%.

The striped pattern observed horizontally in Fig. 6.3(a) corresponds to the readout strips which have a varying hit efficiency. Similarly, the vertical bands of different efficiency in Fig. 6.3(b) correspond to the wire groups which, like the strips, have varying hit efficiencies. The wire groups are 18 mm wide which corresponds to half the x width of the bins. Inefficient spots are observed on all efficiency maps. The spots are due to the presence of 7 mm disk-shaped button supports used to keep the gas volume thickness uniform.

Operating high voltage tuning

The hit efficiencies measured on the efficiency maps of Fig. 6.3 are lower than the 98% requirement of the NSW specifications. The low efficiency, as explained later, can partly be explained by the electronics configuration used during data taking. Other running parameters such as the operating high voltage have a direct impact on the hit efficiency.

The NSW sTGC modules are expected to operate efficiently at a nominal operating voltage of 2.9 kV. Due to small differences in construction, the exact operating voltage used for each sTGC layer can require some optimization if the target hit efficiency is not reached. The average hit efficiency of layer 1 of the 40×60 cm^2 sTGC prototype is measured as a function of the operating voltage to obtain an “efficiency curve”, shown in Fig. 6.4. The maximum efficiency is reached when a plateau is reached on the efficiency

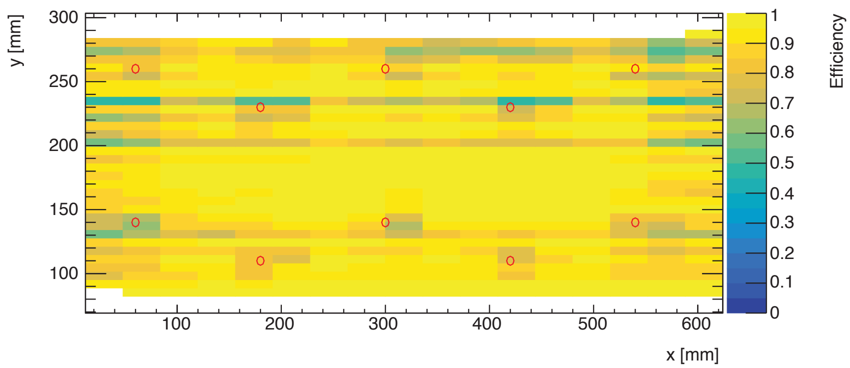

(a)

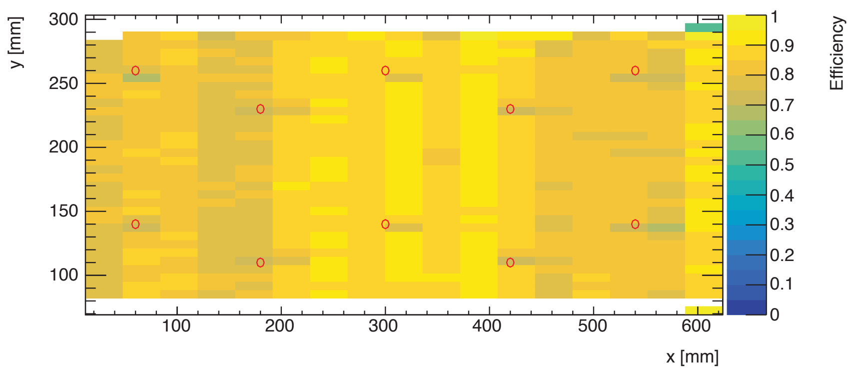

(b)

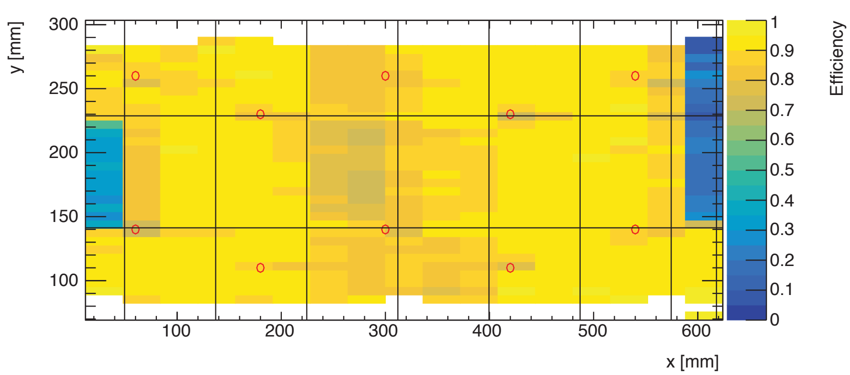

(c)

Figure 6.3: Efficiency maps of the (a) strip, (b) wire and (c) pad electrodes for layer 4 of the 40×60 cm^2 sTGC prototype. The pad electrodes layout is indicated as black lines in (c). The operating voltage is 2.9 kV. The VMM1 gain is 1.0 mV/fC for strips and 0.5 mV/fC for pads and wires. The VMM1 integration time is 200 ns for all electrode types. The readout electronics configuration is the same for both the tested layer and the reference layers of the module. The position of button supports in the gas volume of the tested layer is indicated by red circles.

curve, which, for layer 1, occurs at a high voltage of approximately 3.1 kV. The maximum efficiency on the plateau is limited by the non-sensitive regions of the detector plane.

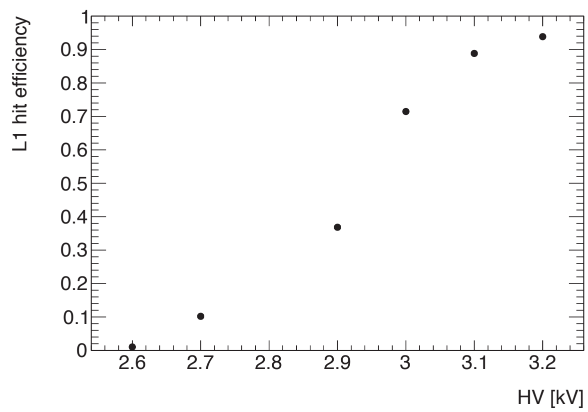

Figure 6.4: Average hit efficiency for layer 1 of the 40×60 cm^2 sTGC prototype as a function of the operating voltage.

Figure 6.5 shows the efficiency maps of layer 1 at the nominal voltage of 2.9 kV, and at the optimal voltage of 3.1 kV. The disc-shaped button supports are clearly visible at 3.1 kV, appearing as regions of decreased efficiency. At the operating voltage of 2.9 kV, the hit efficiency is, for most of the detector sensitive area, significantly lower than the 98% target; however, the efficiency target is met at 3.1 kV. It is important to note that a low average hit efficiency at nominal operating voltage could indicate manufacturing defects of the sTGC module, in which case the particular module would need to be thoroughly investigated to find the cause for the low efficiency. Only if appropriate, will the operating voltage be tuned to the optimal value based on the efficiency curve.

Uncertainties

The statistical uncertainty on the hit efficiency measurement depends on the number of reference tracks and the average hit efficiency of the measurement bin. The statistical error as a function of the number of reference tracks obtained using the Clopper Pearson method [126] with a confidence interval of 68% is shown in Fig. 6.6. The average

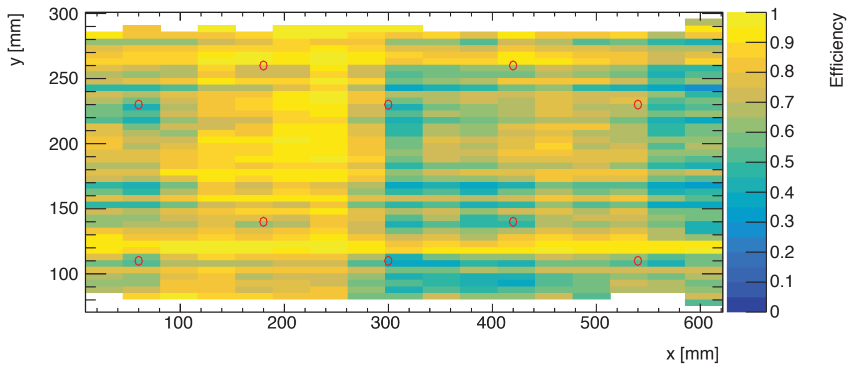

(a)

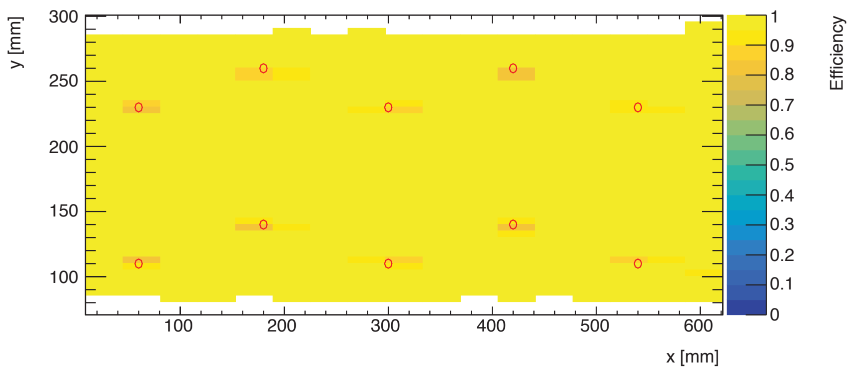

(b)

Figure 6.5: Strip efficiency maps for layer 1 of the $40{\times}60$ cm^2 sTGC prototype at an operating voltage of (a) 2.9 kV and (b) 3.1 kV. The position of button supports in the gas volume of the tested layer is indicated by red circles.

data taking time based on the reference track density measured during a typical cosmic-ray run is indicated. Bins of dimensions 6.4×36 mm^2 are assumed. Assuming that a statistical error lower than 1% is desired, a data taking time of approximately 10 hours is required. The bin dimensions must be increased if the available data taking time is shorter for a given statistical error target.

The main systematic effect for the hit efficiency map is the accuracy on the identification of the measurement bin based on the reference track. The Bin Identification Accuracy (BIDA) is limited by the spatial resolution of the strip and wire electrodes. The BIDA typically increases as a function of the bin width. The bin width must, however, be

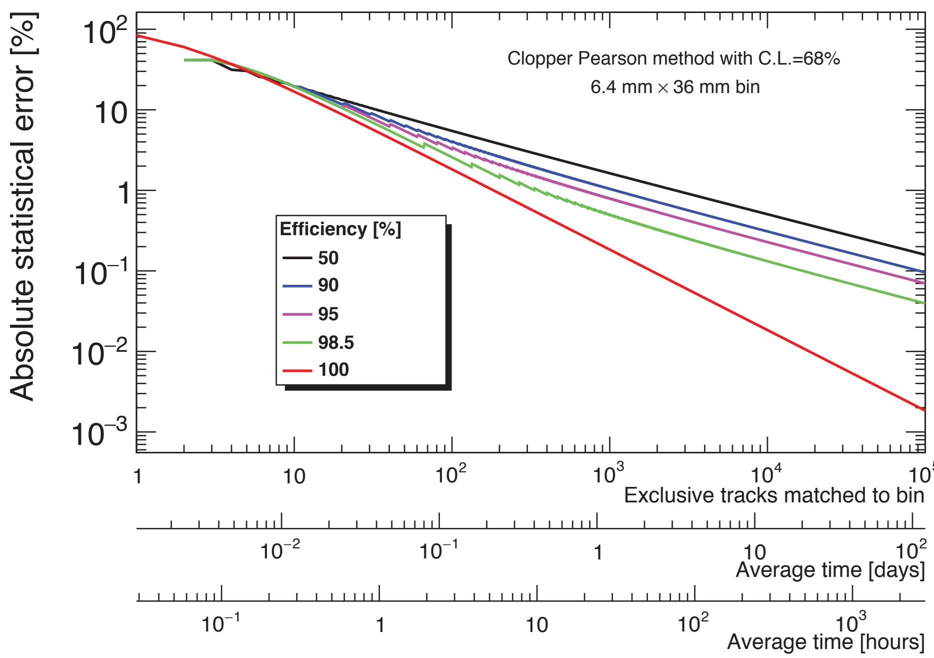

Figure 6.6: Absolute statistical error on the hit efficiency measurement obtained using the Clopper Pearson method with a confidence interval of 68% for different measured hit efficiencies. The calculated error is the maximum deviation from the measured efficiency within a confidence interval width of 68%. The corresponding average data taking time is indicated assuming bins of dimensions 6.4×36 mm^2 and the reference track density of a typical cosmic-ray run using the 40×60 cm^2 prototype sTGC.

small enough to observe the localized effects of structural supports and manufacturing defects on the hit efficiency. Using a Monte Carlo simulation described in Appendix D, the BIDA was calculated as a function of the bin width. The x and y bin dimensions for the efficiency maps shown in this chapter correspond to a BIDA equal or better than 95%.

Discussion

The hit efficiency target of 98% is not met for most sensitive areas of the detector planes. The low efficiency is partly explained by the voltage threshold levels of the VMM1 that could not be properly fine-tuned on a channel-by-channel basis because of limitations in the ASIC design. Therefore, some readout channels had higher effective thresholds for reading out signal pulses than others, leading to a lower efficiency associated with those readout channels. This effect explains the striped efficiency regions observed in the strip and wire efficiency maps. The efficiency of individual pads also varies significantly, as observed in Fig. 6.3(c), due to this effect.

A better performance is expected with the VMM3 ASIC because the VMM3 design has an improved threshold fine tuning capability. The pad efficiency map shows that at least 2 pad channels have a hit efficiency close to zero. A third pad has an average efficiency of approximately 40%. The exact cause for these low hit efficiency regions has not been investigated further in order to instead pursue studies on a full-scale sTGC prototype module.

In summary, operational parameters such as, for example, the global threshold, the threshold fine-tuning, the gain, the integration time and the high voltage must be optimized in order to demonstrate that the module under test can achieve the required efficiency. Given an appropriate optimization of the operational parameters, a satisfactory hit efficiency should be achievable, in which case the hit efficiency would be a useful metric for the QC testing of sTGC modules.

6.3.2 Strip spatial resolution and layer misalignments

The strip spatial resolution and layer misalignments are obtained using the reference track y-residual distributions. The inclusively and exclusively reconstructed reference tracks are associated with the measurement bin located at the position of the inclusively reconstructed reference track on the tested layer. Each individual measurement bin is associated with the exclusive and inclusive y-residual distributions of the matched muon tracks. Events with one charge cluster on each of the 4 layers of the tested sTGC module are used for analysis. Reference tracks at an angle $|\theta_{yz}| < 0.25$ rad are used for analysis because the spatial resolution is better and relatively constant, to within 30%, as seen in Fig. 5.10(a). Additionally, at least 3 wire space points must be recorded on any detector plane to obtain a x-z reference track with a good bin identification accuracy, as explained before. The x-z reference track provides the x-coordinate of the measurement bin.

The spatial resolution is obtained for each measurement bin using the techniques described in Section 5.1 but without correcting for differential non-linearity and inter-layer misalignment in order to save computing time. First, the y-residual distributions are fitted to a double Gaussian function. Then, the value for the spatial resolution σ is obtained based on the signal width of the double Gaussian functions using the formula $\sigma_{\text{sTGC}}^2 = \sigma_{s,\text{in}}^2 + \sigma_{s,\text{ex}}^2$.

The metric used to describe the layer misalignments on each tested layer is the mean of the inclusive track residuals, μ_{in}, a parameter of the double Gaussian fit on the inclusive y-residual distribution. The true layer shifts are not computed for QC testing because they depend on the arbitrary choice of the reference detector planes.

Results

The intrinsic strip spatial resolution (σ_{sTGC}) and the fitted μ_{in} parameter are shown as a function of position in Fig. 6.7 and Fig. 6.8 respectively. The dataset used for both figures required 68 hours of data taking corresponding to a total of 1.2×10^5 muon tracks. The bin dimensions are 30 mm $\times$ 28 mm in the (x, y) coordinates and were optimized as to obtain a statistical error of a few microns on the fitted μ_{in} parameter. The measurement bins associated with a number of reference tracks below a predefined threshold are white to remove values with a large statistical error. The threshold is set to 50 muon tracks for the displayed results.

The measured spatial resolution is shown to vary between 80 and 150 microns over the area of the detector plane. A full row of bins at $y = 200$ mm is white due to the presence of bad strip channels on detector planes other than the tested layer which reduces the number of inclusive reference tracks incident in this region. The bin row at $y = 225$ mm has a larger spatial resolution than neighbour rows also explained by the presence of bad channels on the other layers. The bad channels effectively reduce the number of perpendicular tracks available for the measurement of the spatial resolution for the layer under test. The spatial resolution of inclined tracks is larger as measured in Chapter 5. Conversely, the measured spatial resolution is smaller on the sides of the detector plane because reference tracks at low angle $|\theta_{yz}|$ angle are favoured.

The value of the measured μ_{in} varies between -100 and -10 microns over the area of the tested layer. The parameter is observed to increase as a function of x which indicates a misalignment in rotation. The misalignment was also observed in Chapter 5 when reading out 3 detector planes.

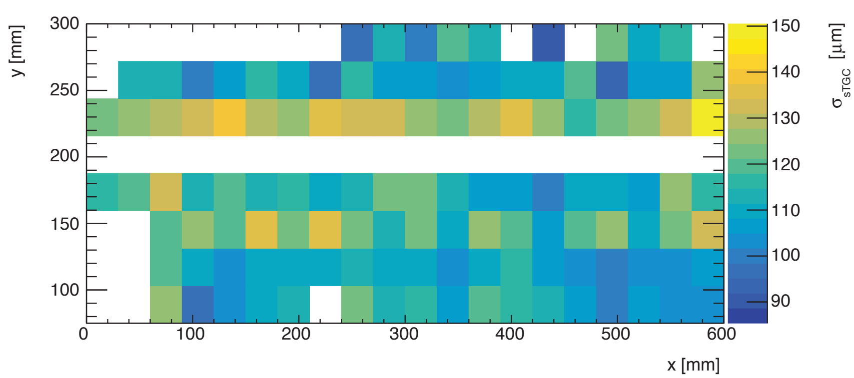

Figure 6.7: Strip intrinsic spatial resolution as a function of position for layer 4 of the 40×60 cm^2 sTGC prototype.

Uncertainties

The error on the spatial resolution is derived by the error propagation of Eq. 5.13 and using the errors on the fitted parameters of the double Gaussian likelihood fits on the inclusive and exclusive y-residuals distributions. The relative error varies between 2%

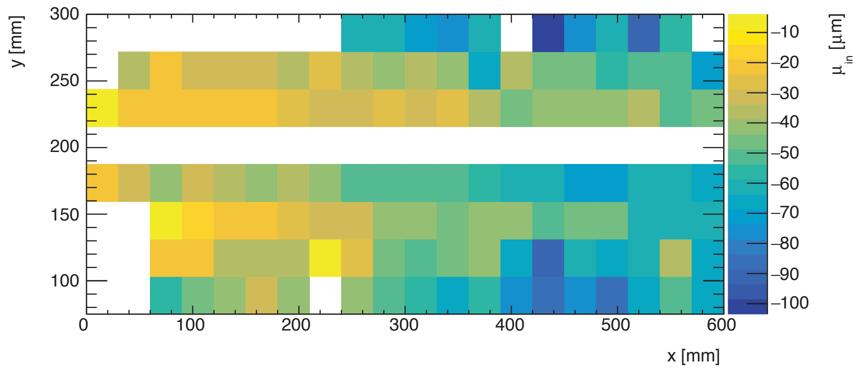

Figure 6.8: Value of the mean obtained from the fitted double Gaussian function to the exclusive y-residual distribution for layer 4 of the 40×60 cm^2 sTGC prototype.

and 10% depending on the number of entries N in each measurement bin, which varies between 50 and 2800. The relative error is observed to follow a $1/\sqrt{N}$ trend where N is the number of entries in a bin.

The error on the mean of the inclusive y-residuals, also obtained from the fit, varies between 1 and 6 µm and also varies as $1/\sqrt{N}$ as a function of the number of entries N in each measurement bin.

The systematic errors on both spatial resolution and mean of residuals measurement include channel-by-channel variations of the electronic charge gain and threshold which distort the shape of charge clusters. The binning identification accuracy, as for the hit efficiency measurement, is also a source of systematic error.

Discussion

The measurements presented in this section demonstrate that the spatial resolution is not a robust cosmic-ray performance metric. The value of the spatial resolution is highly dependent on the angle of incidence of the reference tracks which leads to acceptance biases. As shown in Fig. 6.7, the variations of spatial resolution due to this effect (in the vicinity of the bad channels) are over 50%, which is of the order of the acceptance criteria target defined earlier for this metric.

On the other hand, the mean of y-residuals is not affected by acceptance biases and is sensitive to inter-layer misalignments that should result in the rejection of a sTGC module. In fact, given that the error on the mean y-residual varies between 1 and 10 µm and that the typical size of a production module is 1 m, the technique would be sensitive to inter-layer misalignments of the order of $0.001°$. The mean y-residual metric would have the ability to identify modules that are out of specification considering that the construction tolerance for a rotation of the strip-board pattern is 0.004° (from Table 4.1).

After investigation, it was found that one brass insert of the sTGC module used for the measurement did not have a proper contact with the alignment pin during the doublet gluing construction step which caused the rotation of a detector plane.

6.3.3 Gain uniformity

The gas gain uniformity of the detector planes is tested by measuring the charge Q inducted on the strip, wire or pad electrodes as a function of position. The charge associated with a strip hit is defined as the sum of the signal peak values of all strips making a charge cluster including neighbour triggered strips. Charge clusters of any strip multiplicity higher than 3 are used for analysis. For pad and wire electrodes, the charge Q read out by the electrode is used provided that the tested detector plane has no more than one readout channel above threshold for the tested electrode type. The signal peak value must be below the saturation level in all cases.

The Q values are matched to the measurement bins corresponding to the calculated x and y coordinates of an exclusive reference track on the tested layer. Distributions of the Q values are obtained for the strip, pad and wire electrodes for each measurement bin. A Landau function is fitted to the distribution of Q values. The gain uniformity map is a plot of the MPV parameter of the fitted Landau functions as a function of position. The measurement of the gain uniformity metric assumes that the electronic noise is small enough such that the Q distribution is not smeared.

An example of a Landau fit on the strip charge distribution for a single measurement bin of a gain uniformity map of the 40×60 cm^2 sTGC prototype is shown in Fig. 6.9. As shown in the figure, the distribution of Q values is well described by a Landau function and, therefore, the Most Probable Value (MPV) parameter of the fitted Landau function is a good approximation for the MPV of the Q distribution.

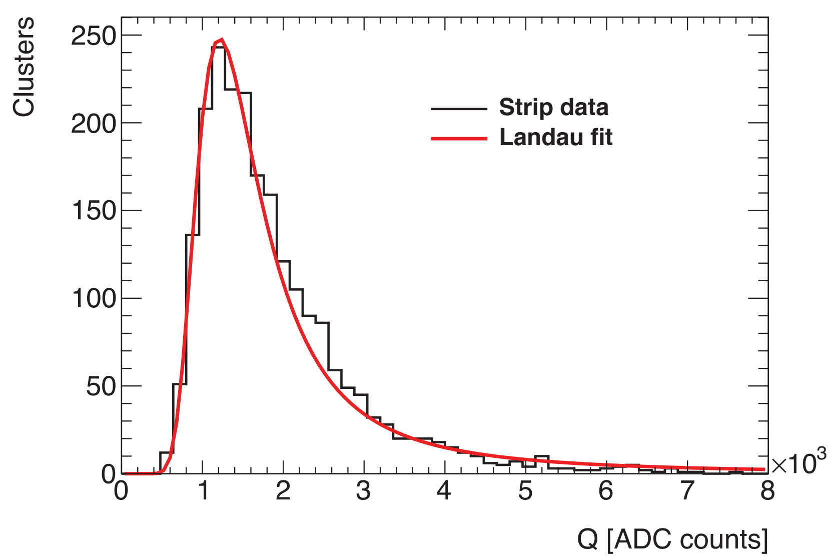

Figure 6.9: Distribution of the strip cluster charge with Landau fit for a single measurement bin of the gain uniformity map located at 280 mm $\leqslant x <$ 300 mm and 270 mm $\leqslant y <$ 280 mm. Measurements were performed on layer 2 of the 40×60 cm^2 sTGC prototype.

Results

Gain uniformity maps for strip, wire and pad electrodes are shown as an example in Fig. 6.10. The dataset used for the gain uniformity map required 68 hours of data taking for strips (1.0×10^6 charge clusters), 68 hours for wires (4.2×10^5 wire hits) and 24 hours for pads (3.2×10^5 pad hits). The bin dimensions are 20 mm $\times$ 10 mm in (x, y) and were optimized to obtain an error on the fitted Landau parameter better than 1% while keeping a binning identification accuracy better than 95%. White bins are matched with a number of hits that is less than a predefined threshold. The threshold is set to 100 hits for the displayed results. This requirement corresponds to a relative error on the fitted MPV parameter better than approximately 1% for the measured distributions.

The MPV is observed to vary between 1000 and 2400 ADC counts for the strips, 800 and 2000 ADC counts for the wires and 300 and 700 ADC counts for the pads. The fitted MPV value of measurement bins on the sides of the detector planes is almost half of the MPV of inner bins as observed, for example, in Fig. 6.10(a) and Fig. 6.10(b). The effect is due to the smaller acceptance of side measurement bins to tracks at large polar angle which, on average, create more primary ionization in the gas volume. The MPV value is directly observed to increase as a function of the $|\theta_{yz}|$ angle as shown in Fig. 6.11. The effect also explains the high MPV region at $y = 200$ mm on the wire uniformity map. Bad strip channels are located over that region on other layers which increases the average angle $|\theta_{yz}|$ of the reference muon tracks uses to provide the bin y-coordinate.

The pad gain uniformity map is observed to correlate with the pad electrode pattern. This effect is due to the charge gain and the threshold of the readout channels which, although they are configured to be the same for all pads, varies as a function of the pad channel. The variations in threshold effectively cut the measured Q distributions and bias the Landau fits.

Finally, the row of white bins observed in Fig. 6.10(a) is due to dead strip readout channels on the tested layer. The button supports can be seen as regions of relatively lower gain on the strip and wire efficiency maps.

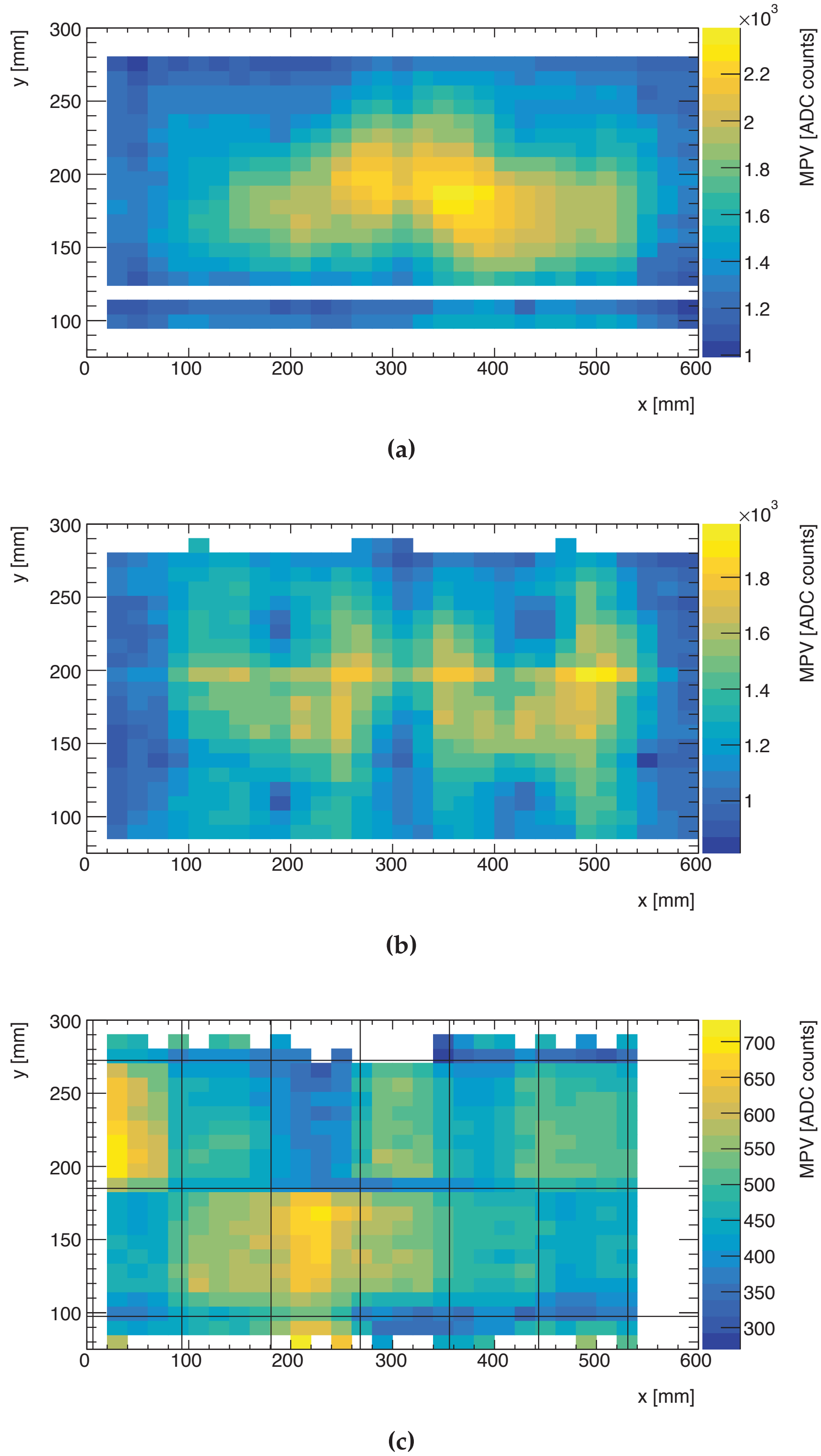

Figure 6.10: Value of the MPV parameter of the fitted Landau functions as a function of position for (a) layer 2 strip, (b) layer 4 wire and (c) layer 1 pad electrodes of the $40{\times}60$ cm^2 sTGC prototype. The black lines indicate the pad electrodes pattern in (c).

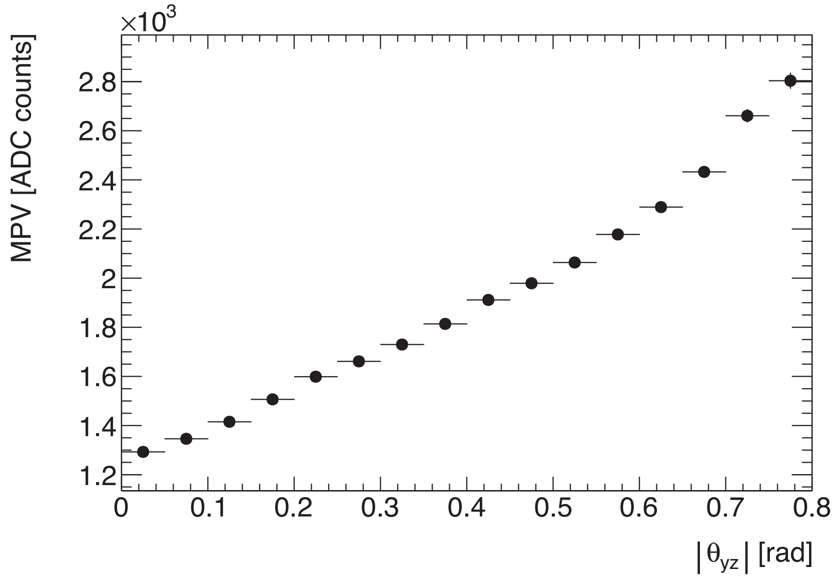

Figure 6.11: Most probable value of the fitted Laudau function of the strip Q values as a function of the muon track angle $|\theta_{yz}|$.

Gain correlation

The charge Q is observed to correlate between electrode types of a single layer. The correlation is observed in the two-dimensional distributions of the Q values of an electrode type as a function of another of the same gas volume as shown in Figure 6.12. The charge induction on the anode and the cathodes is expected to be the same but of opposite signs as described in Chapter 2. The measured charge induction on the cathode and anode electrodes have the same sign because the VMM1 charge amplifier is configured to output a positive signal in any case. The charge correlation could help identify the sources of potential issues with a gain uniformity map and indicate whether the problem originates from the connectivity of a readout channel or the gas gain.

The correlation is weaker for the strip-pad correlation because some fraction of the pad charge is lost by capacitive coupling to neighbouring pads. In this case, the picked-up signal of neighbour pads is below threshold and was not acquired by the DAQ system. The strips are less sensitive to this effect because of neighbour triggering. The capacitive

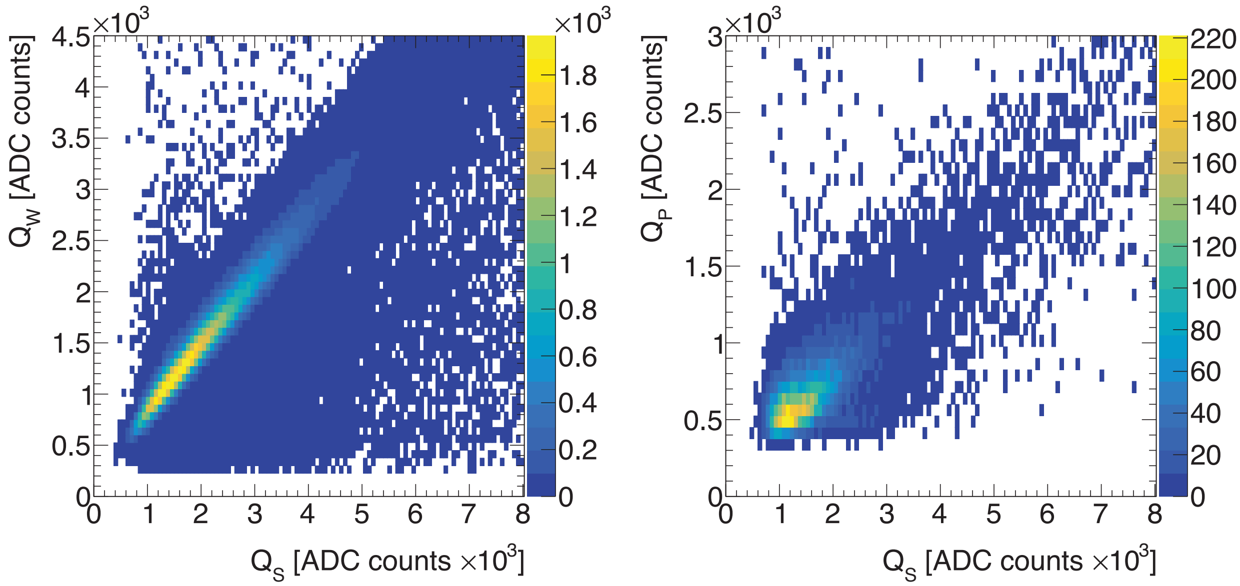

(a) **(b)**

Figure 6.12: Two-dimensional distributions of Q for (a) layer 2 strips and wires and (b) layer 3 strips and pads measured with the 40×60 cm^2 sTGC prototype.

coupling between wire channels is relatively smaller than for pads which limits this effect for wire electrodes.

Uncertainties

The relative error on the fitted MPV values, which is obtained from the Landau likelihood fit, varies between 0.1 and 0.6%. The error is observed to vary as $1/\sqrt{N}$ where N is the number of entries in a measurement bin.

The main systematic effect is the variation of charge deposition as a function of the track angle. Other systematic effects such as the channel-by-channel electronic charge gain and threshold variations can bias the Landau fit for specific channels. This effect is especially important for pads for which individual electrodes cover a large area. As with other cosmic-ray performance metrics, the bin identification accuracy is a source of systematic error.

Discussion

The variations of gain uniformity that are due to the reference track angular acceptance are too large to conclude on the uniformity of the actual gas gain or electrode connectivity of the tested detector layer. The values provided by the gain uniformity map are not robust enough to be used as a cosmic-ray performance metric.

The angular acceptance bias could potentially be corrected by the precise knowledge of the muon polar angle θ which would provide the path length of muons in the gas volume. The polar angle is not, however, known precisely using in-situ data because the track angle in the x-z plane, provided by the wire readout, is known with a poor accuracy.

6.4 Summary of cosmic-ray quality control measurements

Proof-of-concept measurements of candidate cosmic-ray QC performances metrics were shown in this chapter. The hit efficiency was shown to be a robust and easy to interpret metric. Some tuning of the operation parameters, such as the readout electronics charge threshold and gain, and the high voltage, are required in order to reach the full potential of the tested sTGC modules.

The measurement of inter-layer misalignments using the mean of the y-residuals was shown to identify misalignments of the tested module with a sufficient accuracy to certify a sTGC module. The error on this performance metric is smaller than the target construction tolerance for detector misalignments.

On the other hand, the spatial resolution and gain performance metrics were shown to be bad indicators of a detector quality. In both cases, the measured value of the metric is dominated by systematic effects linked to the variations of spatial resolution or primary ionization as a function of the reference track polar angle. These systematic effects, since they are related to the angular acceptance of reference tracks, cannot easily be corrected for.

7

Summary and outlook

Characterization studies of sTGC detectors were performed under the scope of the NSW upgrade of the ATLAS detector at the CERN laboratory. The aim of the studies was to provide an assessment of the muon track reconstruction performances delivered by the sTGC detector technology and to explore possible performance metrics that can be used to certify the manufacturing and quality control procedures of sTGC detectors.

The track reconstruction performances of an NSW sector were simulated in order to study the impact of sTGC module construction non-conformities. A set of sTGC modules strip cathode boards non-conformities was considered and simulated. The intrinsic sTGC spatial resolution and hit efficiency were taken into account in the simulation. The effect of the considered non-conformities on the muon track segment angle reconstructed by the simulated NSW sector was characterized. Simulation results showed that current construction tolerances and the measured sTGC technology performance metrics are adequate to deliver detector modules that meet the NSW specifications.

The intrinsic sTGC strip spatial resolution was measured with cosmic-rays, using the cosmic-ray hodoscope of the McGill University sTGC Testing Facility, and in a test-beam setup, at the Fermilab Test-Beam Facility, using pions. The cosmic-ray measurements were performed using a small $40{\times}60$ cm^2 sTGC quadruplet prototype. The spatial resolution was obtained using reference tracks reconstructed in-situ from sTGC detector hits. Layer misalignments and differential non-linearity biases were corrected using a novel iterative approach. The spatial resolution was measured as a function of the track angle and using two different cluster centroid reconstruction algorithms. The spatial resolution dependence as a function of the track angle was found to be well described by a charge production fluctuations model. This is the first in-situ cosmic-ray measurement to achieve a spatial resolution less than 100 µm with sTGC detectors, approaching the results obtained in a test-beam using an external tracker. Test-beam measurements were performed using a pixel tracker which provided a precise reference pion track. A full-size sTGC prototype quadruplet was used for the test. The detector misalignments and differential non-linearity biases were corrected by fitting the dataset to a Gaussian model. An intrinsic strip spatial resolution of 43.4 ± 0.8 µm was measured for perpendicular tracks.

A measurement of the time jitter of sTGC pads was performed using cosmic-rays. The fraction of hits inside an optimal 25 ns time window, or bunch crossing identification efficiency, is shown to increase as a function of the operating voltage. This effect is due to the increased electron drift velocity and lowered primary ionization threshold in the critical region of amplification. Without any optimization of readout parameters, the bunch crossing identification efficiency was measured, using a full-size sTGC prototype quadruplet, to be 75% when using a 3.1 kV operating voltage. This result provides a baseline measurement for the development and optimization of the NSW trigger processor.

A procedure for the quality control of sTGC modules using cosmic rays was developed. The modules quality control is performed in-situ, without the use of an external tracker detector, which required the development of novel analysis strategies. Possible performance metrics to be used for the certification of sTGC modules were studied using a 40×60 cm^2 sTGC prototype. Proof-of-concept measurements of the detector hit efficiency, spatial resolution, layer misalignments, and gain uniformity for all electrode types of a module were presented. Possible sources of biases for each type of measurement were discussed. The hit efficiency measurement has been shown to be the simplest, most robust and easiest to interpret performance metric for characterizing the detector quality. The mean of the track y-residuals has been shown to identify misalignments between the detector layers with a sufficient accuracy to be used as a quality control performance metric.

The McGill sTGC Testing Facility is anticipated to start testing NSW modules in 2018. The certification of a large number of full-size modules will be an opportunity to validate and tune, if necessary, the algorithms for cosmic-ray testing. More realistic quality control measurements are expected as full-size modules will be read out with the VMM3 ASIC, which features less dead channels and a better channel-by-channel threshold fine tuning capability.

The completion of the NSWs is planned for 2020. First data taking with sTGC modules is expected in 2021 when the muon track reconstruction performances of the sTGC detectors, as part of the ATLAS muon spectrometer, will be measured using p-p collision data.

The sTGC detection technology is likely to be used for muon detection in future high energy experimental projects. They are cost-effective and deliver good track reconstruction performances even at high particle fluxes. These qualities are crucial considering the increasing size of experimental projects and the anticipated luminosity of the next generation of particle accelerators [127]. Alternatives to multiwire chamber detection systems, such as micropattern gaseous detectors, which include Micromegas, Micro-Strip Gas Chambers (MSGC) and Gas Electron Multipliers (GEM), emerged during the last three decades [128, 129]. These detectors feature a high granularity and a very high spatial resolution even at high particle fluxes (approaching MHz/mm^2). Micropattern gaseous detectors, however, are more complex to manufacture, especially for large fiducial areas, and are more sensitive to ageing and discharges. They also require a high bandwidth readout with sensitive low-noise readout electronics [109]. Thus, multiwire chambers remain a relevant option for future large-scale high energy physics projects.

A

Analytic expression for the track reconstruction angular resolution

An analytic expression for the angular resolution of a sTGC sector as a function of the track angle, the intrinsic spatial resolution and the hit efficiency is derived in this Appendix. The expression assumes a perfect detector construction and infinite detector planes.

A.1 Angular resolution of arbitrarily spaced detector planes

The analytic formula used to perform a linear fit using the space point coordinates (z_i, y_i) measured by the detector planes is

$$m = \frac{SS_{zy} - S_z S_y}{SS_{zz} - (S_z)^2} \qquad b = \frac{S_{zz} S_y - S_z S_{zy}}{SS_{zz} - (S_z)^2} \tag{A.1}$$

where m and b are, respectively, the slope and the offset fit parameters. The S symbols are sums over the space points coordinates

$$S = \sum_i \frac{1}{\sigma_i^2} \qquad S_{zy} = \sum_i \frac{z_i y_i}{\sigma_i^2} \qquad S_y = \sum_i \frac{y_i}{\sigma_i^2} \qquad S_z = \sum_i \frac{z_i}{\sigma_i^2} \qquad S_{zz} = \sum_i \frac{z_i^2}{\sigma_i^2} \tag{A.2}$$

where σ_i is the error on the y-coordinate of the space points. The value of σ_i can be interpreted as the sTGC intrinsic spatial resolution σ_{sTGC}. The errors on the track slope m and the offset b are obtained from, respectively, the expressions

$$\sigma_m^2 = \frac{S}{SS_{zz} - (S_z)^2} \qquad \text{and} \qquad \sigma_b^2 = \frac{S_{zz}}{SS_{zz} - (S_z)^2}. \tag{A.3}$$

The track angle θ is obtained from $m = \tan(\theta)$. The error on the track angle, or angular resolution $\sigma_{\Delta\theta}$, is derived using error propagation:

$$\sigma_{\Delta\theta}^2 = \left|\frac{d\theta}{dm}\right|^2 \sigma_m^2 = \frac{1}{(m^2+1)^2}\sigma_m^2 = \frac{1}{(\tan^2\theta + 1)^2}\sigma_m^2. \tag{A.4}$$

Using Eqs. (A.2) to (A.4), the angular resolution of a set K of n detectors is

$$\sigma_{\Delta\theta,K}(\theta, \sigma_{\text{sTGC}}) = \frac{1}{\tan^2\theta + 1} \sqrt{\frac{n}{n\sum_{i\in K} z_i^2 - \left(\sum_{i\in K} z_i\right)^2}}\ \sigma_{\text{sTGC}}. \tag{A.5}$$

In the special case for which all detector planes of a NSW sTGC sector record a hit, and using the z values of Table 4.2, the angular resolution is

$$\sigma_\theta\,[\mu\text{rad}] = \frac{2.111}{\tan^2\theta + 1}\ \sigma_{\text{sTGC}}\,[\mu\text{m}]. \tag{A.6}$$

The result is the same for both small and large sector types, since the z spacing between the detector planes is unchanged.

A.2 Sector trigger efficiency

Assuming a 3-out-of-4 algorithm for trigger, the angular resolution of a sTGC sector is obtained from the average of the angular resolutions measured with the sets of all possible triggered tracks which are made up of 6, 7 or 8 space points. In general, for a set of N detector planes of hit efficiency ε, the probability of having n detectors planes recording a hit is

$$P_n(N,\varepsilon) = (1-\varepsilon)^{N-n}\varepsilon^n \frac{N!}{n!(N-n)!}. \tag{A.7}$$

One sTGC sector is made up of two wedges each having 4 independent detector planes. The probability of having 3 or 4 hits in either of the wedges is

$$P_{\text{L1 trigger}}(\varepsilon) = \left[P_3(4,\varepsilon) + P_4(4,\varepsilon)\right]^2. \tag{A.8}$$

The value of $P_{\text{L1 trigger}}$ as a function of the single plane hit efficiency is shown in Fig. A.1.

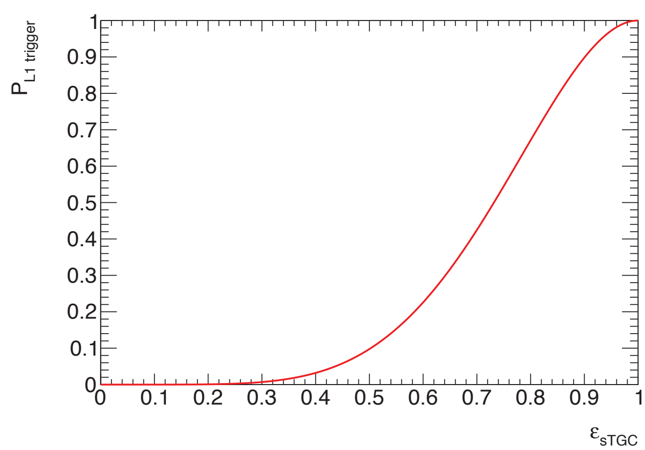

Figure A.1: Trigger efficiency as a function of the single plane sTGC hit efficiency

Assuming all detector planes making up a sector have the same hit efficiency, the probability of having a set K of detector planes i recording a hit is

$$P_K(\varepsilon) = \prod_{i\in K}\varepsilon \prod_{i\notin K}(1-\varepsilon) \tag{A.9}$$

Let T be the set which contains all sets of triggered detector planes K that result in a Level-1 trigger. In T, there is 1 set for which all detectors planes record a hit, 8 sets with 7 detector planes and 16 sets with 6 detector planes. The sector angular resolution is obtained from the average of the variance of $\Delta\theta$ for the sets K weighted with the probability of observing each individual set. The angular resolution $\sigma_{\Delta\theta}$ is obtained from

$$\sigma^2_{\Delta\theta}\left(\theta, \sigma_{\mathrm{sTGC}}\right) = \frac{\sum\limits_{K \in T} P_K(\varepsilon) \;\; \sigma^2_{\Delta\theta,K}\left(\sigma_{\mathrm{sTGC}}\right)}{P_{\mathrm{L1\ trigger}}\left(\varepsilon\right)}. \tag{A.10}$$

The angular resolution calculated using Eq. A.10 and assuming the z spacing of the NSW sTGC sectors is shown in Fig. A.2.

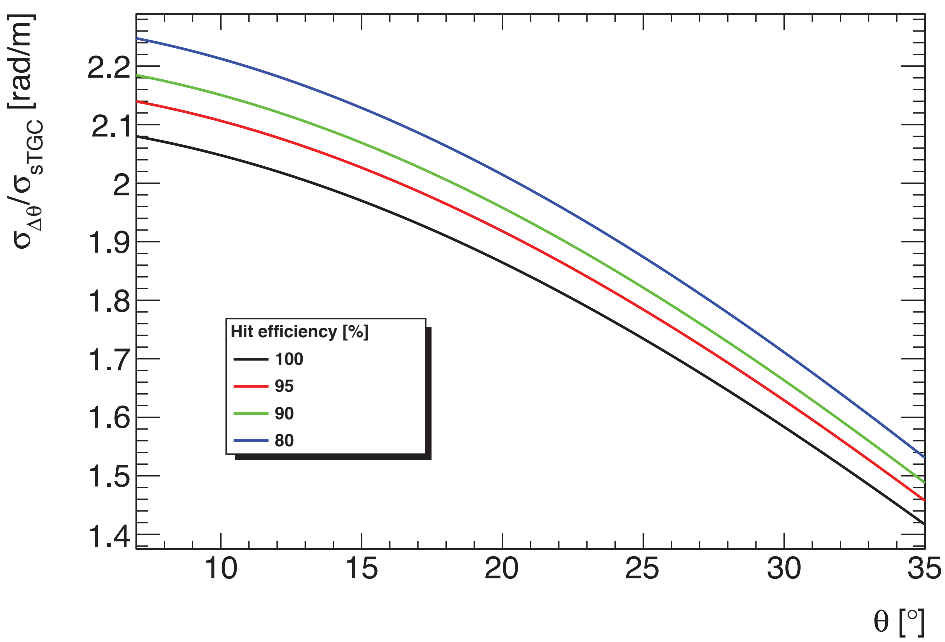

Figure A.2: Angular resolution of a NSW sTGC sector scaled to the intrinsic spatial resolution as a function of the track angle for different values of the hit efficiency. The angular acceptance of a sTGC sector is approximately between 7° and 35°.

B

Matrix technique for deriving layer misalignments

Assuming the error on the y-coordinate is equal for all space points, the expression of Eq. A.1 for the track slope m and the offset b is

$$m = \frac{N \sum_i z_i y_i - S_z \sum_i y_i}{\mathcal{Z}} \qquad b = \frac{S_{zz} \sum_i y_i - S_z \sum_i z_i y_i}{\mathcal{Z}}. \tag{B.1}$$

where the sums are over all space points, N is the number of space points and S_z and S_{zz} are defined in Eq. A.2 omitting the errors σ_i. The variable $\mathcal{Z}$ is defined as

$$\mathcal{Z} \equiv N S_{zz} - (S_z)^2 \,. \tag{B.2}$$

The inclusive track y-residuals are given by

$$\Delta_i = y_i - m z_i - b. \tag{B.3}$$

The expressions for the slope and the offset are linear with respect to the y-coordinates of the space points. Therefore, the expression of Eq. B.3 can conveniently be expressed in a matrix form

$$\mathbf{\Delta} = \mathbf{M}\mathbf{y} \tag{B.4}$$

where the elements of the vectors $\mathbf{\Delta}$ and $\mathbf{y}$ are respectively the y-residuals and the y-coordinates of the hit points. The elements of the $N \times N$ matrix $\mathbf{M}$ are:

$$M_{ij} = \delta_{ij} + \frac{z_i(S_z - Nz_j) + z_j S_z - S_{zz}}{\mathcal{Z}} \tag{B.5}$$

where δ_{ij} is the Kronecker delta. Local detector plane misalignments can be expressed by the transformation

$$\mathbf{y} \to \mathbf{y} + \delta\mathbf{y} \tag{B.6}$$

where the elements of $\delta\mathbf{y}$ are the y displacements of the space points. Using the transformation of Eq. B.6, Eq. B.4 becomes:

$$\mathbf{\Delta} = \mathbf{M}\mathbf{y} + \mathbf{M}\delta\mathbf{y}. \tag{B.7}$$

Assuming the y-coordinate of the space points is not biased with respect to the true track position, the mean of the residuals of a perfectly aligned detector is zero which implies that

$$\langle \mathbf{M}\mathbf{y} \rangle = 0 \tag{B.8}$$

where each element of the vector $\langle \mathbf{M}\mathbf{y} \rangle$ is the mean over many tracks of the corresponding element in $\mathbf{M}\mathbf{y}$. It follows that

$$\langle \mathbf{\Delta} \rangle = \langle \mathbf{M}\mathbf{y} \rangle + \langle \mathbf{M}\delta\mathbf{y} \rangle = \langle \mathbf{M}\delta\mathbf{y} \rangle = \mathbf{M}\delta\mathbf{y}. \tag{B.9}$$

The vector $\mathbf{M}\delta\mathbf{y}$ is not a random variable and therefore is equal to its statistical mean. The system of Eq. B.9 cannot be solved directly for $\delta\mathbf{y}$ because the matrix $\mathbf{M}$ is singular and therefore cannot be inverted. This is expected as layers misalignments are only meaningful if expressed with respect to an external geometric reference. The system of equations can be solved if at least two space points are defined as being the geometric reference [1].

A valid geometric reference is obtained by fixing the value of two elements of the vector $\delta\mathbf{y}$. The system of equation is then overdetermined as it lost two unknowns. By using Gaussian elimination the system can be reduced to a $(N-2)$-dimensions system of equations. The reduced system of equations is

$$\langle \boldsymbol{\Delta} \rangle^* = \mathbf{M}^* \delta \mathbf{y}^* \tag{B.10}$$

where the asterisk $(*)$ denotes variables of the reduced system. The system can be solved by first computing the inverse of $\mathbf{M}^*$ to solve for $\delta\mathbf{y}^*$, and then applying the inverse Gaussian elimination on the $\delta\mathbf{y}^*$ vector to return to the original $\delta\mathbf{y}$ vector.

As an example, details of the procedure to derive the inter-layer misalignments of the 40×60 cm^2 sTGC prototype used in Chapters 5 and 6 are shown below. The sTGC module has 3 readout layers positioned at $z = 0$ mm, 11 mm, 21.8 mm. Track residuals are observed to vary linearly as a function of the x-coordinate as shown in Fig. 5.7(a). Thus, the following parameterization of the vector $\langle \boldsymbol{\Delta} \rangle$ is used

$$\langle \boldsymbol{\Delta} \rangle = \mathbf{m}_{\boldsymbol{\Delta}} x + \mathbf{b}_{\boldsymbol{\Delta}} \tag{B.11}$$

where the components of the vectors $\mathbf{m}_{\boldsymbol{\Delta}}$ and $\mathbf{b}_{\boldsymbol{\Delta}}$ are obtained from the linear fits of the mean of the tracks y-residuals on each layer. The numerical values of $\mathbf{M}$, $\mathbf{m}_{\boldsymbol{\Delta}}$ and $\mathbf{b}_{\boldsymbol{\Delta}}$ are

1. As an illustration for $N = 3$, take any 3 random points in the 2D space. Any one point can be displaced to form a perfect straight line with the 2 other points.

$$\mathbf{M} = \begin{bmatrix} 0.164 & -0.330 & 0.167 \\ -0.330 & 0.667 & -0.336 \\ 0.167 & -0.336 & 0.170 \end{bmatrix}, \tag{B.12}$$

$$\mathbf{m}_{\boldsymbol{\Delta}} = \begin{bmatrix} -65.7 \times 10^{-6} \\ 133.4 \times 10^{-6} \\ -67.6 \times 10^{-6} \end{bmatrix}, \qquad \mathbf{b}_{\boldsymbol{\Delta}} = \begin{bmatrix} -19.5\,\mu\mathrm{m} \\ 39.2\,\mu\mathrm{m} \\ -19.7\,\mu\mathrm{m} \end{bmatrix}$$

Components of M and $\mathbf{m}_{\boldsymbol{\Delta}}$ are unitless. As a consequence of the linear parameterization of Eq. B.11, the layer misalignments also vary linearly as a function of the x-coordinate. Layers 1 and 2 are taken as the reference layers and are assumed perfectly aligned. Thus, the layer displacement vector is

$$\delta\mathbf{y} = \boldsymbol{\phi}_{\delta\mathbf{y}}\, x + \mathbf{b}_{\delta\mathbf{y}} = \begin{bmatrix} 0 \\ 0 \\ \phi_3 \end{bmatrix} x + \begin{bmatrix} 0 \\ 0 \\ b_3 \end{bmatrix} \tag{B.13}$$

where ϕ_3 and b_3 are the slope and offset of the layer 3 displacement. The slope can be interpreted as the angle of rotation of the plane. The reduced system of equations is obtained by subtracting the 3$^{\text{rd}}$ row of the system with the 1$^{\text{st}}$ and the 2$^{\text{nd}}$ rows. The reduced system consists of the 3$^{\text{rd}}$ row of the previous system and the 3$^{\text{rd}}$ column of the matrix M. The reduced one-dimensional system of equations is

$$\mathbf{M}^*(\boldsymbol{\phi}^*_{\delta\mathbf{y}}\, x + \mathbf{b}^*_{\delta\mathbf{y}}) = \mathbf{m}^*_{\boldsymbol{\Delta}}\, x + \mathbf{b}^*_{\boldsymbol{\Delta}} \tag{B.14}$$

where $\mathbf{M}^* = [0.339]$, $\mathbf{m}^*_{\boldsymbol{\Delta}} = [-135.3 \times 10^{-6}]$ and $\mathbf{b}^*_{\boldsymbol{\Delta}} = [-39.4\ \mu\mathrm{m}]$. The parameters $\boldsymbol{\phi}^*_{\delta \mathbf{y}} = [\phi_3]$ and $\mathbf{b}^*_{\delta \mathbf{y}} = [b_3]$ are unknowns. The solution must be valid for all values of x and, therefore, the system must be solved independently for all powers of x. The final solution is

$$\begin{aligned} \boldsymbol{\phi}^*_{\delta \mathbf{y}} &= \left(\mathbf{M}^*\right)^{-1} \mathbf{m}^*_{\boldsymbol{\Delta}} = [396 \times 10^{-6}] \\ \mathbf{b}^*_{\delta \mathbf{y}} &= \left(\mathbf{M}^*\right)^{-1} \mathbf{b}^*_{\boldsymbol{\Delta}} = [113\ \mu\mathrm{m}]. \end{aligned} \tag{B.15}$$

In summary, the mean track y-residuals for each detector plane of a multi-layer detector can be expressed as a linear system of equations with the layer displacements being unknowns of the system. The system of equations is initially singular. The singular system is solved by defining two arbitrary planes as the geometric reference and applying Gaussian elimination to reduce the N-dimensions singular system to a $N-2$ dimensions non-singular system. An example of the application of the technique was presented using cosmic-ray data from the 40×60 cm^2 sTGC prototype. In this case, the y-residuals are linear as a function of the x-coordinate. The layer displacements, which are also assumed linear, are parameterized with a slope ϕ and an offset b which are found by solving the non-singular system of equations independently for each power of x.

C

Track reconstruction with wire groups

Track reconstruction in the x-z plane with sTGC modules is performed using the wire channels which consist of multiple anode wires ganged together to form a single readout channel. The x-coordinate of the sTGC space points is taken as the center of the wire group having the largest peak value on each detector plane. A wire hit is typically not spread over more than one wire channel. The z-coordinate of the space points is the position of the planes formed by the anode wires of a gas volume.

A linear fit on the wire hits is performed to obtain the reconstructed track in the x-z plane. The width of the wire groups is of the order of a few centimeters, larger than the inter-plane spacing. Therefore, in some cases, the reconstructed track significantly differs from the true muon track. A Monte Carlo simulation is used to verify that reconstructed tracks obtained using a linear fit are representative of the cosmic-ray muons triggering the McGill sTGC Testing Facility Hodoscope.

The simulation assumes a constant inter-plane spacing of 10.8 mm and a wire group width, denoted d, of 18 mm. The wire groups are staggered by half the group width between layers. The simulated geometry is similar to the configuration of the 40×60 cm^2 sTGC prototype tested in Chapters 5 and 6. The simulated muon tracks are straight with a random polar angle generated from a $\cos^2\theta$ probability density function similar to the observed distribution for cosmic rays [5].

Only wire tracks using three detectors plane are relevant for detector performance and quality control measurements. Thus, wire tracks using two or four hits are not considered. As shown in Fig. D.3, only a small set of reconstructed wire tracks is possible for cosmic-ray data taking at the McGill University sTGC Testing Facility considering the limited angular acceptance of the cosmic-ray hodoscope. If the $\pm x$ symmetry is taken into account, only two types of reconstructed tracks are possible in extrapolation and three in interpolation. Reconstructed tracks of different types differ in their slope and are displayed with different colours in Fig. D.3.

For each type of track, the position distribution of the simulated muon track on the excluded layer, whose hit is not used for the linear fit, is obtained. The mean of the position distribution, denoted x_{MC}, is compared to the result of the linear fit, denoted x_{fit}, and to the center of the limits of the angular acceptance of the considered wire groups, denoted $\bar{x}$. Results of the simulation are shown in Fig. C.1 for the extrapolation case and in Fig. C.2 for the interpolation case. The bottom of the figures shows the pattern of the simulated sTGC module wire groups. The excluded layer is displayed by dotted boxes. Wire groups traversed by the simulated muon track are displayed with bolder lines. The position of the wire space points is indicated by red markers. The red line indicates the reconstructed track obtained from a linear fit to the wire space points. The red arrow indicates the position of the reconstructed track on the excluded layer. The blue lines are muon tracks pointing to extremum positions on the excluded layer. The simulated position distribution is shown as a black line in the top part of the figures. The distribution has the same normalization for all the shown figures. The red curve denotes the Gaussian probability density function of the reconstructed track position assuming that the wire space points have a Gaussian error of width $d/\sqrt{12}$. The blue dotted lines indicate the extremum track positions for the considered wire groups. The black and blue arrows respectively denote the position of x_{MC} and $\bar{x}$. The top and the bottom parts of the figures share the same x axis.

For the extrapolation case, the value of x_{fit} is within 2 mm of x_{MC} for the perpendicular fitted track type. The difference is 10 mm for the angled fitted track type, which is less likely to occur. For the interpolation case, values of x_{fit}, x_{MC} and $\bar{x}$ are within 2 mm of each other for all track types. In any case, the difference between x_{fit} and x_{MC} is small compared to the spread of the simulated position distribution. In some cases, the value of $\bar{x}$ offers a better estimate of the value of x_{MC} than x_{fit}. However, the difference is not significant and the simplicity of the linear fit algorithm lcompensates its lower accuracy.

In conclusion, due to its good performances and simplicity, the linear fit algorithm is used for wire track reconstruction to carry out sTGC performance and quality control measurements.

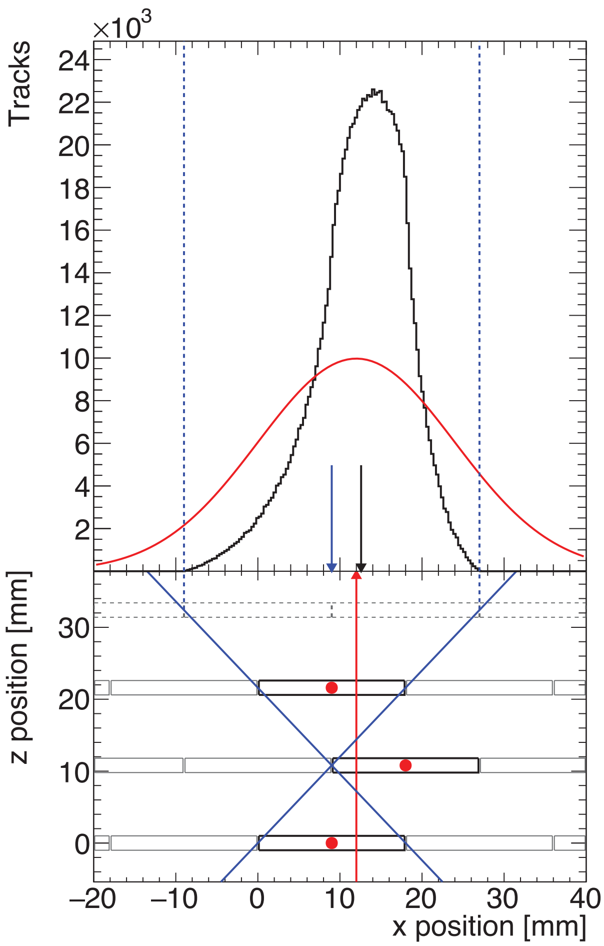

(a)

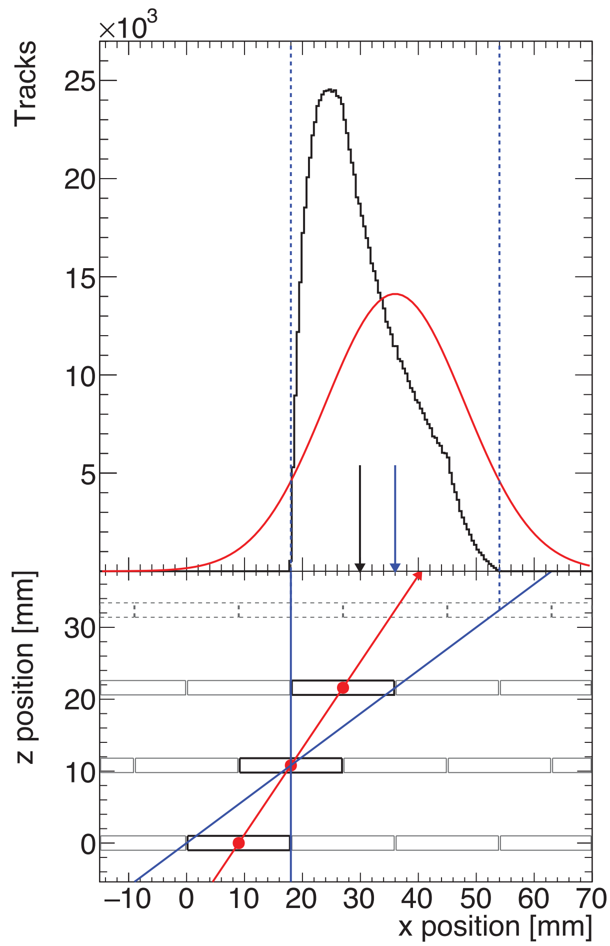

(b)

Figure C.1: Results of the wire track **extrapolation** simulation for the two track types considered.

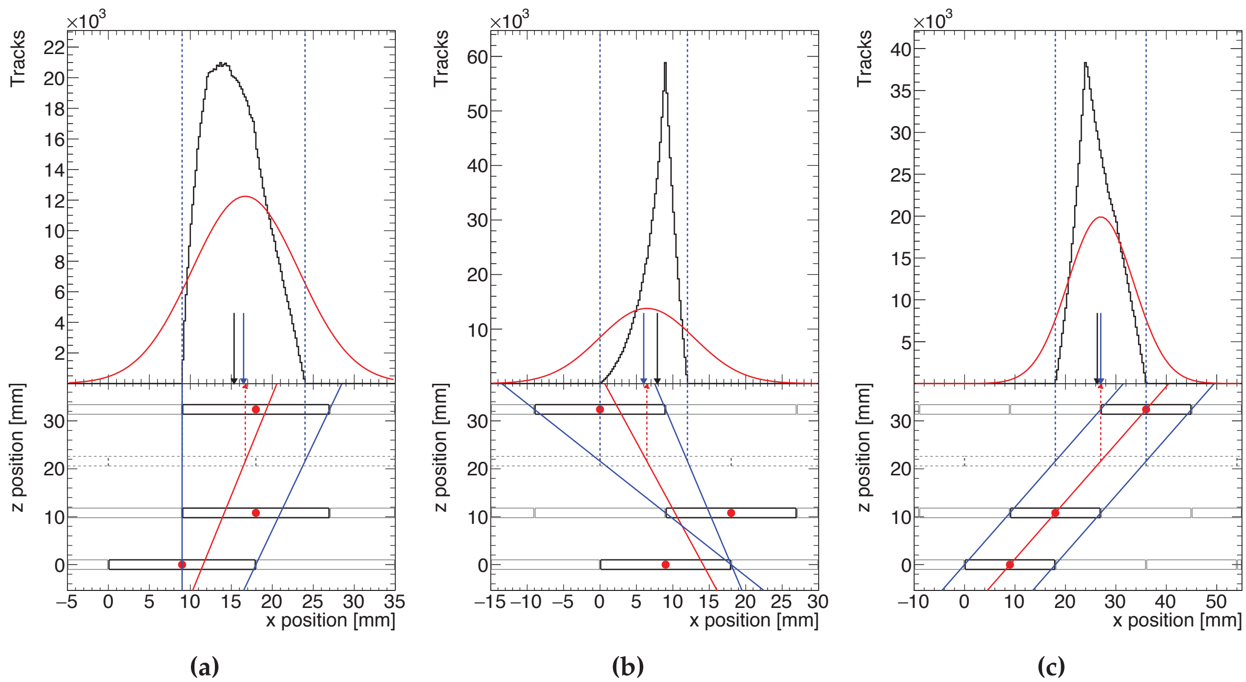

Figure C.2: Results of the wire track **interpolation** simulation for the three track types considered.

D

Bin identification accuracy

The value of the cosmic-ray performance metrics is obtained as a function of position by dividing the detector plane area in rectangular x-y bins. For the hit efficiency measurement, the y-z and x-z reference tracks used to identify the measurement bin are exclusively reconstructed.

Due to the finite spatial resolution of the reference tracks, there is a probability that the measurement bin identified by the reference track does not match the bin that would be identified by the true muon track. The Binning Identification Accuracy (BIDA) is defined as the probability that the bins identified by both the reconstructed and true tracks match. The BIDA is different for x and y binning because the strip and wire track reconstruction strategies are different. The calculation of the BIDA for y and x binning are presented in Sections D.1 and D.2 respectively.

D.1 Study of the bin y-dimension

The spatial resolution on the tested layer of the exclusive y-z track, obtained using the strip hits, is estimated from the distribution of y-residuals. The spatial resolution is related to the width of the y-residual distributions. The width actually provides an upper limit on the value of the spatial resolution because the y-residual distributions are smeared by the finite spatial resolution of the tested layer. The measured y-residuals distributions are shown in Fig. D.1 for the extrapolating case (tested layer is 4) and for the interpolating case (tested layer is 3). Reference tracks selected using the analysis cuts described in Section 6.3.2 are used to obtain the distributions but with a varying number of space points. No correction for layer misalignments or the differential non-linearity bias are applied for simplicity.

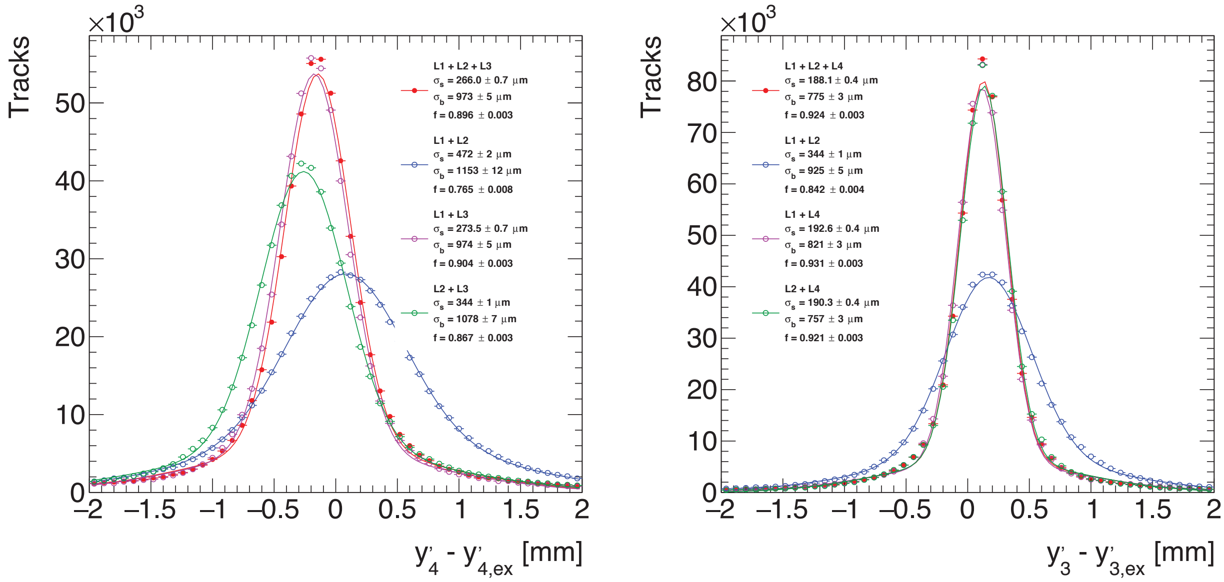

(a) **(b)**

Figure D.1: Exclusive y-residual distributions for (a) an outer tested layer (layer 4) and for (b) and inner tested layer (layer 3). The full red markers denote the track y-residuals from a track reconstructed with all 3 exclusive layers. The other markers indicate tracks reconstructed with only 2 exclusive layers. The distributions have the same normalization. The distributions are fitted to a double Gaussian function. The width of the signal (σ_s) and background (σ_b) Gaussians and the signal fraction f are shown.

The BIDA is estimated by assuming that the difference between the reconstructed track and the true track positions on the tested layer follows a probability density function $F(y; y_T, \sigma_T)$ parameterized by the reference track position y_T and the reference track spatial resolution σ_T. Assuming the y dimension of the measurement bin is w, the bin identification accuracy is

$$\mathcal{A}(y_T) = \int_0^w F(y; y_T, \sigma_T)\, dy. \tag{D.1}$$

The accuracy averaged over the bin width, assuming that all reference track positions are equally likely, is

$$A = \frac{1}{w} \int_0^w \mathcal{A}(y_T)\, dy_T. \tag{D.2}$$

The value of A corresponds to the BIDA along the y-axis. Assuming F is a Gaussian p.d.f. parameterized with $y_T = \mu$ and $\sigma_T = \sigma$, the expression for the BIDA is:

$$A = \mathrm{erf}\left(\frac{w}{\sqrt{2}\sigma}\right) + \sqrt{\frac{2}{\pi}} \left[\exp\left(-\frac{w^2}{2\sigma^2}\right) - 1\right] \frac{w}{\sigma}. \tag{D.3}$$

Eq. D.3 can be modified for a spatial resolution expressed as a double Gaussian function by adding one term for the background Gaussian function. The signal fraction f weights the signal and background terms. The BIDA value as a function of the bin width w is computed using the double Gaussian fit parameters of Fig. D.1 are shown in Fig. D.2.

The spatial resolution model used to compute the BIDA assumes no differential non-linearity effects. If DNL effects were accounted for, the BIDA value would vary as a function of the bin offset with respect to the strip edges. Therefore, in order to mitigate the differential non-linearity effects and obtain bins of equal BIDA values, the bin width should be a multiple of the strip pitch which is 3.2 mm for the NSW sTGC strip-boards.

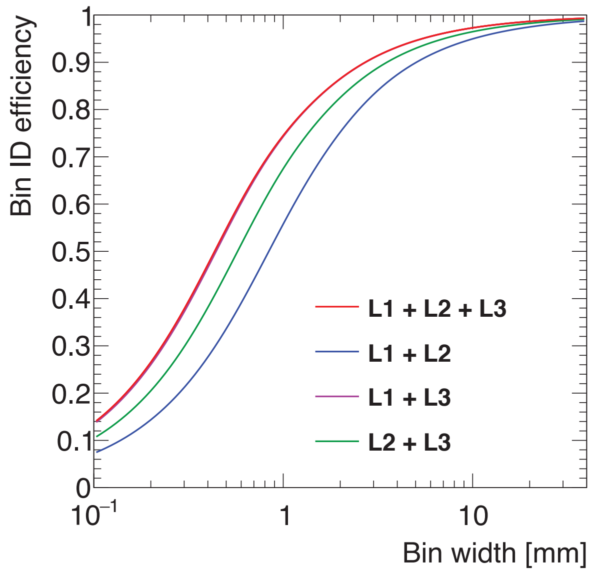

(a)

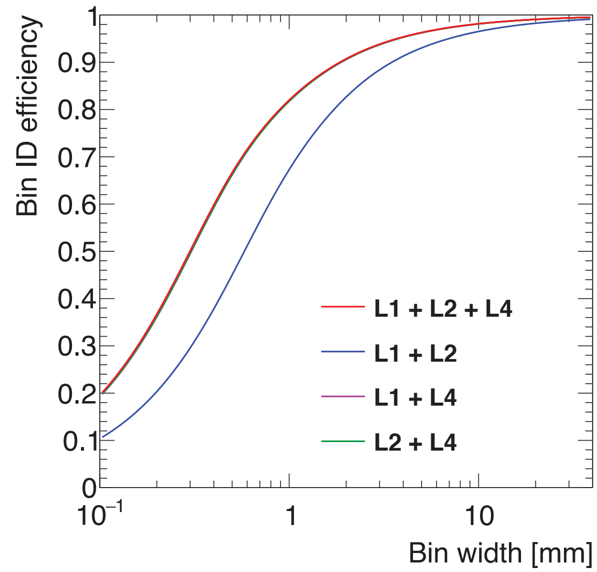

(b)

Figure D.2: Calculated BIDA values for (a) an outer tested layer (layer 4) and (b) an inner tested layer (layer 3) based on the parameters of the double Gaussian function fitted to the exclusively reconstructed track y-residual distributions shown in Fig. D.1. The layers used for the exclusive track reconstruction are indicated in the legend. The purple and red line coincide for the outer layer case (a). The red, purple and green curves coincidence for the inner layer case (b).

D.2 Study of the bin x-dimension

The x-z reference track position on the tested layer is discrete rather than continuous like for reference tracks reconstructed with strip hits in the y-z plane. The wire hits that provide the reference track are positioned at the center of the wire group having the largest signal peak value on each detector plane. Therefore, the x-z reference tracks are incident on a finite number of x position on the tested layer. A sketch of the possible x-z reference tracks is shown in Fig. D.3 for the interpolation and extrapolation cases. The displayed tracks fall into the McGill cosmic-ray hodoscope angular acceptance. The sketch assumes that the wire groups are staggered by half a wire group width between each layer, or half staggering, which corresponds to the approximate design of the 40x60 cm^2

sTGC prototype.

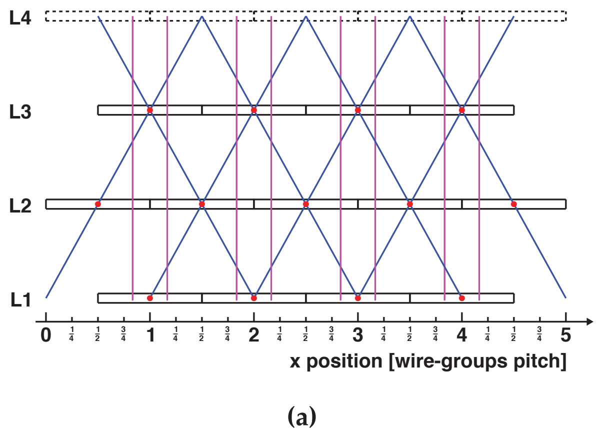

Figure D.3: Sketch of the possible x positions of a reference track reconstructed with wire hits in the x-z plane on the tested layer of a sTGC built with half staggering of the wire groups and equal distance between detector planes. The special cases for an (a) outer tested layer (layer 4) and (b) inner tested layer (layer 3) are shown. The wire groups are identified by rectangles. The wire groups of the tested layer have dotted lines. The position of the reconstructed wire space points is marked by a red dot in the middle of the wire groups. The tracks are displayed using lines of different colours. Each colour is associated with a different value of the x-z track polar angle $|\theta_{xz}|$.

The discretization of the x-z reference tracks implies that the BIDA is not guaranteed to be independent of the measurement bin offset with respect to the wire groups. Furthermore, the calculated position of the possible reference tracks on the tested layers implies that bins narrower than half the wire group width could be positioned such that they are not identified by any reference track.

The BIDA value as a function of the bin width and offset is obtained using a Monte Carlo simulation. The simulation assumes that the polar angle θ of the true muon tracks follows a $\cos^2\theta$ distribution, similar to the observed distribution for cosmic rays [5]. The simulated detector has 18 mm wide wire groups, a constant distance of 10.8 mm between the detector planes and a half wire group staggering. The space points of the reconstructed track are given by the middle of the wire groups traversed by the true track excluding the tested layer. The bin offset is defined as the distance between the low-x

side of the bin and the low-x side of the closest wire group on the tested layer. Simulation results are shown in Fig. D.4 for the extrapolation and interpolation cases. The simulation shows a clear dependence of the BIDA value on the bin offset. Furthermore, the simulation confirms that the BIDA value is zero if the bin is sufficiently narrow and positioned is a region that is not covered by the reference tracks.

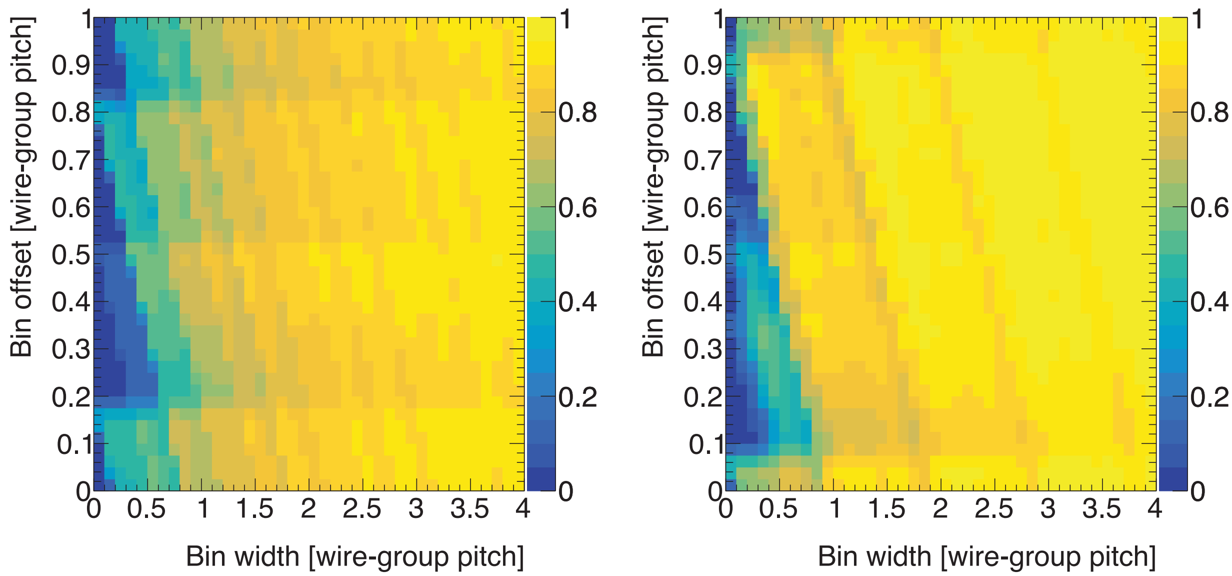

(a) (b)

Figure D.4: Simulated bin identification accuracy as a function of the bin width and the bin offset when the tested layer is (a) an outer layer and (b) an inner layer.

The strong dependence of the BIDA with the bin offset implies that the bin width should be a multiple of the wire group pitch to ensure that the BIDA of all measurement bins is equal. Given this constraint, a bin offset equal to half the wire group pitch provides the largest BIDA based on simulation results.

Taking a fixed offset equal to half the wire group pitch[1], the BIDA values for reference tracks with 2 or 3 space points as a function of the bin width are obtained using

1. Noting that the offset of multiple adjacent measurement bins is equal only if the bin width is equal to a multiple of the wire group width.

the Monte Carlo simulation. The results are shown in Fig. D.5 for the extrapolation and interpolation cases. The simulation shows that, for some specific bin widths, a reference track having 2 space points rather 3 provide a better or similar BIDA. This special case does not, however, occurs for a bin width that is a multiple of the wire group width.

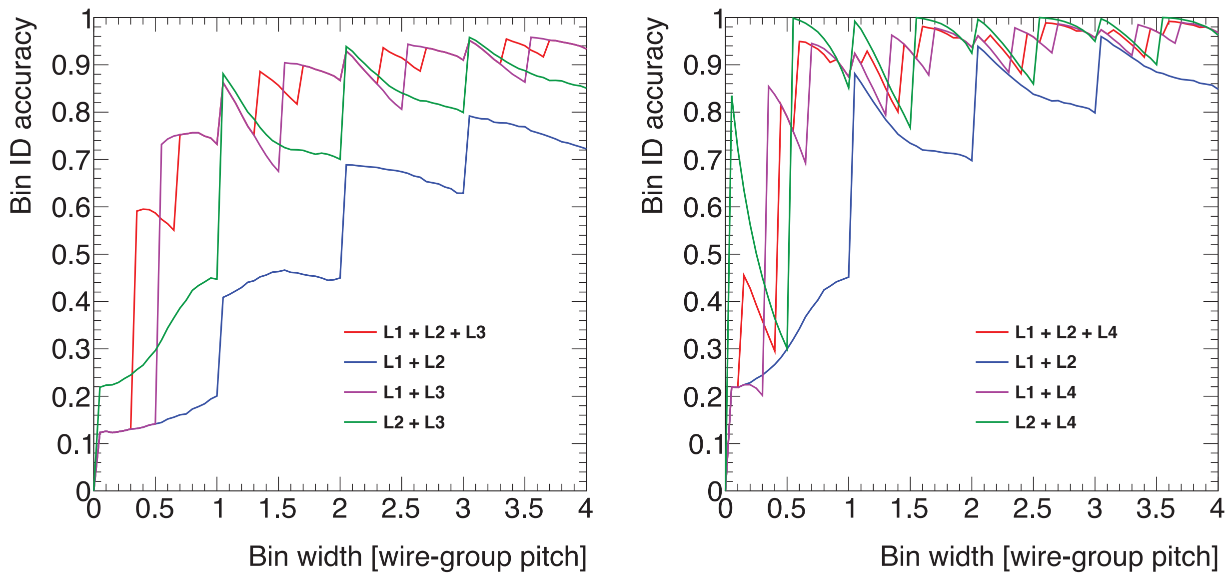

(a) **(b)**

Figure D.5: Simulated BIDA as a function of the bin width for a fixed bin offset equal to half the wire group width when the tested layer is (a) an outer layer and (b) an inner layer. The detector planes used for the reference track reconstruction are indicated in the legend.

Bibliography

[1] C. Burgess and G. Moore, *The Standard Model: A primer*. Cambridge University Press, 2006.

[2] L. Evans and P. Bryant, *LHC machine*, Journal of Instrumentation **3** (2008) S08001.

[3] ATLAS Collaboration, *The ATLAS Experiment at the CERN Large Hadron Collider*, Journal of Instrumentation **3** (2008) S08003.

[4] Wikipedia, *Standard Model of Elementary Particles*, 2006, URL: https://en.wikipedia.org/wiki/Standard_Model. Accessed: 2018-04-06.

[5] Particle Data Group, *Review of Particle Physics*, Chinese Physics **C38** (2014) 090001.

[6] SNO Collaboration, *Measurement of the rate of $\nu_e + d \rightarrow p + p + e^-$ interactions produced by ^8B solar neutrinos at the Sudbury Neutrino Observatory*, Physical Review Letters **87** (2001) 071301.

[7] T2K Collaboration, *Measurements of neutrino oscillation in appearance and disappearance channels by the T2K experiment with 6.6×10^{20} protons on target*, Physical Review D **91** (2015) 072010.

[8] M. Hirsch, R. Srivastava and J. W. Valle, *Can one ever prove that neutrinos are dirac particles?*, Physics Letters B **781** (2018) 302 .

[9] R. Henning, *Current status of neutrinoless double-beta decay searches*, Reviews in Physics **1** (2016) 29.

[10] P. W. Higgs, *Broken symmetries and the masses of gauge bosons*, Physical Review Letters **13** (1964) 508.

[11] LHCb Collaboration, *Observation of $J/\psi\phi$ Structures Consistent with Exotic States from Amplitude Analysis of $B^+ \rightarrow J/\psi\phi K^+$ Decays*, Physical Review Letters **118** (2017) 022003.

[12] LHCb Collaboration, *Observation of $J/\psi p$ resonances consistent with pentaquark states in $\Lambda_b^0 \rightarrow J/\psi K^- p$ decays*, Physical Review Letters **115** (2015) 072001.

[13] G. Charpak, R. Bouclier, T. Bressani, J. Favier and Č. Zupančič, *The use of multiwire proportional counters to select and localize charged particles*, Nuclear Instruments and Methods **62** (1968) 262.

[14] F. Sauli, *Principles of operation of multiwire proportional and drift chambers*, CERN-77-09, CERN, Geneva, 1977, URL: http://cds.cern.ch/record/117989.

[15] J. S. Townsend and S. John, *XIII. Electrical properties of newly prepared gases*, The London, Edinburgh, and Dublin Philosophical Magazine and Journal of Science **45** (1898) 125.

[16] J. S. Townsend and H. E. Hurst, *LXXV. The genesis of ions by the motion of positive ions, and a theory of the sparking potential*, The London, Edinburgh, and Dublin Philosophical Magazine and Journal of Science **8** (1904) 738.

[17] S. Majewski, G. Charpak, A. Breskin and G. Mikenberg, *A thin multiwire chamber operating in the high multiplication mode*, Nuclear Instruments and Methods in Physics Research **217** (1983) 265.

[18] OPAL Collaboration, *The OPAL detector: technical proposal*, CERN-LEPC-83-4, CERN, Geneva, 1983, URL: http://cds.cern.ch/record/300669.

[19] C. Beard, R. Hammarström, D. Hatzifotiadou, C. Kleinwort, L. Köpke, N. Wermes et al., *Thin, high gain wire chambers for electromagnetic presampling in OPAL*, Nuclear Instruments and Methods in Physics Research Section A **286** (1990) 117.

[20] G. Bella, J. Cohen, H. Czyrkowski, P. Fink, N. Horwitz, J. Kalo et al., *Development of calorimeters using thin chambers operating in a high gain mode*, Nuclear Instruments and Methods in Physics Research Section A **252** (1986) 503.

[21] S. Dado, J. Goldberg, N. Lupu, A. Mincer, G. Alexander, G. Bella et al., *A new high gain thin gap detector for the OPAL hadron calorimeter*, Nuclear Instruments and Methods in Physics Research Section A **252** (1986) 511.

[22] G. Mikenberg, *Thin-gap gas chambers for hadronic calorimetry*, Nuclear Instruments and Methods in Physics Research Section A **265** (1988) 223.

[23] LEP Injector Study Group, *LEP design report*, CERN-LEP-TH-83-29, CERN, Geneva, 1983, URL: https://cds.cern.ch/record/98881.

[24] K. Nagai, *Thin gap chambers in ATLAS*, Nuclear Instruments and Methods in Physics Research Section A **384** (1996) 219.

[25] H. Bethe, *Zur theorie des durchgangs schneller korpuskularstrahlen durch materie*, Annalen der Physik **397** (1930) 325.

[26] M. Berger, J. Coursey, M. Zucker and J. Chang, *ESTAR, PSTAR, and ASTAR: Computer programs for calculating stopping-power and range tables for electrons, protons, and helium ions*, 2017, URL: https://www.nist.gov.

[27] L. D. Landau, *On the energy loss of fast particles by ionization*, Journal of Physics **8** (1944) 201.

[28] S. R. Finch, *Mathematical Constants (Encyclopedia of Mathematics and its Applications)*. Cambridge University Press, 2003.

[29] P. V. Vavilov, *Ionization losses of high-energy heavy particles*, Journal of Experimental and Theoretical Physics **5** (1957) 749.

[30] S. Striganov, *Ionization straggling of high energy muons in thick absorbers*, Nuclear Instruments and Methods in Physics Research Section A **322** (1992) 225.

[31] H. Bichsel, *Straggling in thin silicon detectors*, Reviews of Modern Physics **60** (1988) 663.

[32] C. Grupen and B. Shwartz, *Particle Detectors*. Cambridge University Press, Cambridge, United Kingdom, 1st ed., 2008.

[33] ATLAS Collaboration, *Simulation Studies of Characteristics and Performance of small-strip Thin Gap Chamber for the ATLAS New Small Wheel Upgrade*, ATL-MUON-PUB-2014-001, CERN, Geneva, 2014, URL: https://cds.cern.ch/record/1645880.

[34] F. Penning and C. Addink, *The starting potential of the glow discharge in neon-argon mixtures between large parallel plates: I. Results*, Physica **1** (1934) 1007.

[35] F. M. Penning, *Über den einfluß sehr geringer beimischungen auf die zündspannung der edelgase*, Zeitschrift für Physik **46** (1928) 335.

[36] G. Alkhazov, A. Komar and A. Vorobév, *Ionization fluctuations and resolution of ionization chambers and semiconductor detectors*, Nuclear Instruments and Methods **48** (1967) 1.

[37] S. Usačev and M. Seman, *Threshold oscillations in bromine-quenched g-m counters*, Nuclear Instruments and Methods **73** (1969) 41.

[38] F. W. Sears and G. L. Salinger, *Thermodynamics, Kinetic Theory, and Statistical Thermodynamics*. Addison-Wesley, Reading MA, 3^{rd} ed., 1975.

[39] P. Langevin, *L'ionization des gaz*, Annales de chimie et de physique **28** (1903) 443.

[40] J. S. Townsend and H. T. Tizard, *The motion of electrons in gases*, Proceedings of the Royal Society of London. Series A **88** (1913) 336.

[41] C. Ramsauer, *Über den wirkungsquerschnitt der gasmoleküle gegenüber langsamen elektronen*, Annalen der Physik **369** (1921) 513.

[42] J. Townsend, *Electricity in Gases, Clarendon*. Oxford, 1915.

[43] O. Sahin, T. Z. Kowalski and R. Veenhof, *High-precision gas gain and energy transfer measurements in Ar–CO_2 mixtures*, Nuclear Instruments and Methods in Physics Research Section A **768** (2014) 104.

[44] H. Raether, *Electron avalanches and breakdown in gases*, Butterworths advanced physics series. Butterworths, London, 1964.

[45] P. Campion, *Spurious pulses in proportional counters: A review*, Nuclear Instruments and Methods **112** (1973) 75.

[46] G. F. Knoll, *Radiation detection and measurement*. John Wiley & Sons, Hoboken, 3^{rd} ed., 2000.

[47] H. Geiger and W. Müller, *Elektronenzählrohr zur messung schwächster aktivitäten*, Naturwissenschaften **16** (1928) 617.

[48] S. A. Korff et al., *Electron and nuclear counters*. D. Van Nostrand Company, 1946.

[49] H. H. Staub, *Experimental nuclear physics. 1*. Wiley, 1953.

[50] H. Hofer, P. L. Coultre, H. Li, X. Li, Y. Lu, X. Tang et al., *Some properties of thin gap gas chambers*, Nuclear Instruments and Methods in Physics Research Section A **309** (1991) 422.

[51] A. Mincer, S. Dado, J. Goldberg, Y. Gernitzky, D. Lazic, N. Lupu et al., *Charge production in thin gap multi-wire chambers*, Nuclear Instruments and Methods in Physics Research Section A **439** (2000) 147.

[52] H. Spieler, *Semiconductor detector systems*, Semiconductor Science and Technology. Oxford University Press, Oxford, 2005.

[53] G. De Geronimo and S. Li, *Shaper design in CMOS for high dynamic range*, IEEE Transactions on Nuclear Science **58** (2011) 2382.

[54] G. Charpak, G. Petersen, A. Policarpo and F. Sauli, *Progress in high-accuracy proportional chambers*, Nuclear Instruments and Methods **148** (1978) 471.

[55] A. Walenta, *Left-right assignment in drift chambers and MWPC's using induced signals*, Nuclear Instruments and Methods **151** (1978) 461.

[56] J. Fischer, H. Okuno and A. Walenta, *Spatial distribution of the avalanche in proportional counters*, Nuclear Instruments and Methods **151** (1978) 451.

[57] E. Gatti, A. Longoni, H. Okuno and P. Semenza, *Optimum geometry for strip cathodes or grids in MWPC for avalanche localization along the anode wires*, Nuclear Instruments and Methods **163** (1979) 83.

[58] E. Mathieson and J. Gordon, *Cathode charge distributions in multiwire chambers: II. approximate and empirical formulae*, Nuclear Instruments and Methods in Physics Research Section A **227** (1984) 277.

[59] G. Battistoni, E. Iarocci, G. Nicoletti and L. Trasatti, *Detection of induced pulses in proportional wire devices with resistive cathodes*, Nuclear Instruments and Methods **152** (1978) 423.

[60] G. Battistoni, P. Campana, V. Chiarella, U. Denni, E. Iarocci and G. Nicoletti, *Resistive cathode transparency*, Nuclear Instruments and Methods in Physics Research **202** (1982) 459.

[61] ATLAS Collaboration, *ATLAS muon spectrometer: Technical Design Report*, CERN-LHCC-97-022, CERN, Geneva, 1997, URL: http://cds.cern.ch/record/331068.

[62] H. Fukui, M. Yoshida, Y. Miyazaki, Y. Fukatsu, Y. Hasegawa, T. Hosoda et al., *Studies on ageing effects and rate dependence of thin gap chambers*, Nuclear Instruments and Methods in Physics Research Section A **419** (1998) 497.

[63] I. Endo, T. Kawamoto, Y. Mizuno, T. Ohsugi, T. Taniguchi and T. Takeshita, *Systematic shifts of evaluated charge centroid for the cathode read-out multiwire proportional chamber*, Nuclear Instruments and Methods in Physics Research **188** (1981) 51.

[64] E. Mathieson and G. C. Smith, *Reduction in non-linearity in position-sensitive MWPCs*, IEEE Transactions on Nuclear Science **36** (1989) 305.

[65] V. Radeka and R. A. Boie, *Centroid finding method for position-sensitive detectors*, Nuclear Instruments and Methods **178** (1980) 543.

[66] K. Lau and J. Pyrlik, *Optimization of centroid-finding algorithms for cathode strip chambers*, Nuclear Instruments and Methods in Physics Research Section A **366** (1995) 298.

[67] A. Abusleme, C. Bélanger-Champagne, A. Bellerive, Y. Benhammou, J. Botte, H. Cohen et al., *Performance of a full-size small-strip thin gap chamber prototype for the ATLAS new small wheel muon upgrade*, Nuclear Instruments and Methods in Physics Research Section A **817** (2016) 85.

[68] N. Amram, G. Bella, Y. Benhammou, M. A. Diaz, E. Duchovni, E. Etzion et al., *Position resolution and efficiency measurements with large scale Thin Gap Chambers for the super LHC*, Nuclear Instruments and Methods in Physics Research Section A **628** (2011) 177.

[69] ALICE Collaboration, *The ALICE experiment at the CERN LHC*, Journal of Instrumentation **3** (2008) S08002.

[70] CMS Collaboration, *The CMS experiment at the CERN LHC*, Journal of Instrumentation **3** (2008) S08004.

[71] LHCb Collaboration, *The LHCb Detector at the LHC*, Journal of Instrumentation **3** (2008) S08005.

[72] Wikipedia, *LHC experiments and the preaccelerators*, 2006, URL: https://en.wikipedia.org/wiki/Large_Hadron_Collider. Accessed: 2018-04-06.

[73] G. Apollinari, I. Béjar Alonso, O. Brüning, P. Fessia, M. Lamont, L. Rossi et al., *High-Luminosity Large Hadron Collider (HL-LHC): Technical Design Report V. 0.1*, CERN-2017-007-M, CERN, Geneva, 2017, URL: https://cds.cern.ch/record/2284929.

[74] ATLAS Collaboration, *Luminosity Public Results Run 2*, 2018, URL: https://twiki.cern.ch/twiki/bin/view/AtlasPublic/LuminosityPublicResultsRun2. Accessed: 2018-08-06.

[75] ATLAS Collaboration, *ATLAS magnet system: Technical Design Report, 1*, CERN-LHCC-97-018, CERN, Geneva, 1997, URL: http://cds.cern.ch/record/338080.

[76] ATLAS Collaboration, *ATLAS barrel toroid: Technical Design Report*, CERN-LHCC-97-019, CERN, Geneva, 1997, URL: http://cds.cern.ch/record/331065.

[77] ATLAS Collaboration, *ATLAS end-cap toroids: Technical Design Report*, CERN-LHCC-97-020, CERN, Geneva, 1997, URL: http://cds.cern.ch/record/331066.

[78] ATLAS Collaboration, *ATLAS central solenoid: Technical Design Report*, CERN-LHCC-97-021, Geneva, 1997, URL: http://cds.cern.ch/record/331067.

[79] ATLAS Collaboration, *ATLAS inner detector: Technical Design Report, 1*, CERN-LHCC-97-016, CERN, Geneva, 1997, URL: http://cds.cern.ch/record/331063.

[80] ATLAS Collaboration, *ATLAS inner detector: Technical Design Report, 2*, CERN-LHCC-97-017, CERN, Geneva, 1997, URL: http://cds.cern.ch/record/331064.

[81] ATLAS Collaboration, *ATLAS pixel detector: Technical Design Report*, CERN-LHCC-98-013, CERN, Geneva, 1998, URL: http://cds.cern.ch/record/381263.

[82] ATLAS Collaboration, *ATLAS liquid-argon calorimeter: Technical Design Report*, CERN-LHCC-96-041, CERN, Geneva, 1996, URL: http://cds.cern.ch/record/331061.

[83] ATLAS Collaboration, *ATLAS tile calorimeter: Technical Design Report*, CERN-LHCC-96-042, CERN, Geneva, 1996, URL: http://cds.cern.ch/record/331062.

[84] ATLAS TDAQ Collaboration, *The ATLAS Data Acquisition and High Level Trigger system*, Journal of Instrumentation **11** (2016) P06008.

[85] ATLAS Collaboration, *Performance of the ATLAS trigger system in 2015*, The European Physical Journal C **77** (2017) 317.

[86] N. Hessey on behalf of the ATLAS Muon Collaboration, *The precision drift chambers for the ATLAS Muon Spectrometer*, Nuclear Instruments and Methods in Physics Research Section A **419** (1998) 326.

[87] M. Livan for the ATLAS Muon Group, *Monitored drift tubes in ATLAS*, Nuclear Instruments and Methods in Physics Research Section A **384** (1996) 214.

[88] T. Argyropoulos, K. A. Assamagan, B. H. Benedict, V. Chernyatin, E. Cheu, J. Deng et al., *Cathode strip chambers in ATLAS : Installation, commissioning and in situ performance*, IEEE Nuclear Science Symposium Conference Record (2008) 2819.

[89] R. Santonico and R. Cardarelli, *Development of resistive plate counters*, Nuclear Instruments and Methods in Physics Research **187** (1981) 377.

[90] R. Cardarelli, R. Santonico, A. D. Biagio and A. Lucci, *Progress in resistive plate counters*, Nuclear Instruments and Methods in Physics Research Section A **263** (1988) 20.

[91] M. Deile, S. Kircher, G. Herten, N. P. Hessey, U. Landgraf, W. Mohr et al., *Influence of aqueous vapour on the drift properties of MDT gases*, ATL-MUON-97-214, CERN, Geneva, 1997, URL: http://cds.cern.ch/record/685594.

[92] M. Deile, H. Dietl, J. Dubbert, S. Horvat, O. Kortner, H. Kroha et al., *Performance of the ATLAS precision muon chambers under LHC operating conditions*, Nuclear Instruments and Methods in Physics Research Section A **518** (2004) 65.

[93] ATLAS Collaboration, *New Small Wheel Technical Design Report*, CERN-LHCC-2013-006, CERN, Geneva, 2013, URL: https://cds.cern.ch/record/1552862.

[94] ATLAS Collaboration, *Performance of the ATLAS muon trigger in pp collisions at $\sqrt{s} = 8$ TeV*, The European Physical Journal C **75** (2015) 120.

[95] I. Ravinovich, *The New Small Wheel background rates predictions based on CSC and TGC Run-2 measurements.*, ATL-COM-MUON-2016-006, CERN, Geneva, 2016, URL: https://cds.cern.ch/record/2131686.

[96] T. Argyropoulos, K. A. Assamagan, B. H. Benedict, V. Chernyatin, E. Cheu, J. Deng et al., *Cathode Strip Chambers in ATLAS: Installation, Commissioning and in Situ Performance*, IEEE Transactions on Nuclear Science **56** (2009) 1568.

[97] L. Guan on behalf of the ATLAS Muon Collaboration, *Trigger algorithms and electronics for the ATLAS muon new small wheel upgrade*, Journal of Instrumentation **11** (2016) C01083.

[98] Y. Giomataris, P. Rebourgeard, J. Robert and G. Charpak, *Micromegas: a high-granularity position-sensitive gaseous detector for high particle-flux environments*, Nuclear Instruments and Methods in Physics Research Section A **376** (1996) 29.

[99] CERN Engineering & Equipment Data Management Service (EDMS), "New Small Wheel sTGC Detector Drawings." URL: https://edms.cern.ch/nav/P:ATL-0000010588:V0/P:ATL-0000010235:V0. Accessed: 2018-05-03.

[100] P. Povinec, *A study of proportional counter optimization for long-term counting*, Nuclear Instruments and Methods **163** (1979) 363.

[101] S. Tsuno, T. Kobayashi and B. Ye, *Gamma-ray sensitivity of a thin gap chamber*, Nuclear Instruments and Methods in Physics Research Section A **482** (2002) 667.

[102] H. Ohshita, H. Iwasaki, J. Kaneko, H. Kiyamura, M. Nakao, A. Ochi et al., *Neutron irradiation test of an ATLAS thin gap chamber*, Nuclear Instruments and Methods in Physics Research Section A **587** (2008) 259.

[103] S. R. Majewski and G. Charpak, *A thin multiwire chamber operating in saturated and limited streamer modes: preliminary results*, CERN-EP-INT-82-02, CERN, Geneva, 1982, URL: https://cds.cern.ch/record/138523.

[104] J. Lacy and R. Lindsey, *High-resolution readout of multiwire proportional counters using the cathode-coupled delay-line technique*, Nuclear Instruments and Methods **119** (1974) 483.

[105] R. Baumgart, C. Grupen and U. Schäfer, *Properties of streamers in streamer tubes*, Nuclear Instruments and Methods in Physics Research **222** (1984) 448.

[106] NIST, *NIST Chemistry WebBook*, 2017, URL: https://webbook.nist.gov.

[107] V. Smakhtin, G. Mikenberg, A. Klier, Y. Rozen, E. Duchovni, E. Kajamovitz et al., *Thin Gap Chamber upgrade for SLHC: Position resolution in a test beam*, Nuclear Instruments and Methods in Physics Research Section A **598** (2009) 196.

[108] R. Dixon, N. Kwok, I. Koveshnikov, B. Yuen, S. Issinski, R. Langstaff et al., *Standard Operating Procedures: Production Manual, rev. 2.01*. TRIUMF, Vancouver, Canada, 2017.

[109] G. D. Geronimo, J. Fried, S. Li, J. Metcalfe, N. Nambiar, E. Vernon et al., *VMM1 - An ASIC for micropattern detectors*, IEEE Nuclear Science Symposium and Medical Imaging Conference Record (NSS/MIC) (2012) 633.

[110] I. Antcheva, M. Ballintijn, B. Bellenot, M. Biskup, R. Brun, N. Buncic et al., *ROOT — A C++ framework for petabyte data storage, statistical analysis and visualization*, Computer Physics Communications **182** (2011) 1384.

[111] B. Lefebvre, C. Belanger-Champagne, A. Robichaud-Veronneau and B. Vachon, *Study of pedestal measurement methods for VMM1 ASICs*, ATL-COM-UPGRADE-2016-003, CERN, Geneva, 2016, URL: https://cds.cern.ch/record/2134485.

[112] E. Pastuchová and M. Zákopčan, *Comparison of algorithms for fitting a gaussian function used in testing smart sensors*, Journal of Electrical Engineering **66** (2015) 178.

[113] R. Carnegie, M. Dixit, J. Dubeau, D. Karlen, J.-P. Martin, H. Mes et al., *Resolution studies of cosmic-ray tracks in a TPC with GEM readout*, Nuclear Instruments and Methods in Physics Research Section A **538** (2005) 372.

[114] T. Alexopoulos, G. Iakovidis, S. Leontsinis, K. Ntekas and V. Polychronakos, *Examining the geometric mean method for the extraction of spatial resolution*, Journal of Instrumentation **9** (2014) P01003.

[115] P. Rehak and E. Gatti, *Semiconductor detectors in nuclear and particle physics*, American Institute of Physics Conference Proceedings **338** (1995) 319.

[116] I. Rubinskiy, *An EUDET/AIDA pixel beam telescope for detector development*, Physics Procedia **37** (2012) 923.

[117] C. Hu-Guo, J. Baudot, G. Bertolone, A. Besson, A. Brogna, C. Colledani et al., *First reticule size MAPS with digital output and integrated zero suppression for the EUDET-JRA1 beam telescope*, Nuclear Instruments and Methods in Physics Research Section A **623** (2010) 480.

[118] H. Jansen, S. Spannagel, J. Behr, A. Bulgheroni, G. Claus, E. Corrin et al., *Performance of the EUDET-type beam telescopes*, EPJ Techniques and Instrumentation **3** (2016) 7.

[119] Arduino, "UNO." URL: https://store.arduino.cc/arduino-uno-rev3.

[120] G. Iakovidis on behalf of the ATLAS Muon Collaboration, *VMM3, an ASIC for micropattern detectors*, European Physical Journal Web of Conferences **174** (2018) 07001.

[121] Xilinx, *Xilinx Kintex-7 FPGA KC705 Evaluation Kit*, 2018, URL: https://www.xilinx.com/products/boards-and-kits/ek-k7-kc705-g.html. EK-K7-KC705-G.

[122] Molex, *MMCX Microminiature Connectors*, 2015, URL: http://www.literature.molex.com/SQLImages/kelmscott/Molex/PDF_Images/987650-3243.PDF.

[123] Canada sTGC collaboration, *sTGC Assembly Manual*, 2018, URL: https://edms.cern.ch/document/1399978/2.

[124] B. Lefebvre on behalf of the ATLAS Muon Collaboration, *Muon Spectrometer Phase-I Upgrade for the ATLAS Experiment: the New Small Wheel project*, 13th Conference on the Intersections of Particle and Nuclear Physics (CIPANP) (2018) CIPANP2018-Lefebvre, arXiv: 1810.01394[physics.ins-det].

[125] R. Keyes, K. Johnson, L. Pepin, F. Léger, C. Qin, S. Webster et al., *Development and characterisation of a gas system and its associated slow-control system for an ATLAS small-strip thin gap chamber testing facility*, Journal of Instrumentation **12** (2017) P04027.

[126] L. D. Brown, T. T. Cai and A. DasGupta, *Interval estimation for a binomial proportion*, Statistical Science **16** (2001) 101.

[127] M. Benedikt, *Future Circular Collider Study*, CERN-ACC-SLIDES-2016-0017, CERN, Geneva, 2014, URL: http://cds.cern.ch/record/2206380.

[128] F. Sauli, *Micro-pattern gas detectors*, Nuclear Instruments and Methods in Physics Research Section A **477** (2002) 1.

[129] S. D. Pinto on behalf of the RD51 Collaboration, *Micropattern gas detector technologies and applications the work of the RD51 collaboration*, IEEE Nuclear Science Symposium Medical Imaging Conference (2010) 802.